

## INFORMATION TO USERS

This manuscript has been reproduced from the microfilm master. UMI films the text directly from the original or copy submitted. Thus, some thesis and dissertation copies are in typewriter face, while others may be from any type of computer printer.

**The quality of this reproduction is dependent upon the quality of the copy submitted.** Broken or indistinct print, colored or poor quality illustrations and photographs, print bleedthrough, substandard margins, and improper alignment can adversely affect reproduction.

In the unlikely event that the author did not send UMI a complete manuscript and there are missing pages, these will be noted. Also, if unauthorized copyright material had to be removed, a note will indicate the deletion.

Oversize materials (e.g., maps, drawings, charts) are reproduced by sectioning the original, beginning at the upper left-hand corner and continuing from left to right in equal sections with small overlaps. Each original is also photographed in one exposure and is included in reduced form at the back of the book.

Photographs included in the original manuscript have been reproduced xerographically in this copy. Higher quality 6" x 9" black and white photographic prints are available for any photographs or illustrations appearing in this copy for an additional charge. Contact UMI directly to order.

**UMI<sup>®</sup>**

Bell & Howell Information and Learning  
300 North Zeeb Road, Ann Arbor, MI 48106-1346 USA  
800-521-0600



**Analysis of defibrillation efficacy and investigation of  
impedance cardiography with finite element models  
incorporating anisotropic myocardium**

Yanqun Wang

A dissertation submitted in partial fulfillment of the  
requirements for the degree of

Doctor of Philosophy

University of Washington

1999

Program Authorized to Offer Degree: Department of Bioengineering

UMI Number: 9936895

---

UMI Microform 9936895  
Copyright 1999, by UMI Company. All rights reserved.

This microform edition is protected against unauthorized  
copying under Title 17, United States Code.

---

**UMI**  
300 North Zeeb Road  
Ann Arbor, MI 48103

**University of Washington**

**Graduate School**

This is to certify that I have examined this copy of a doctoral dissertation by

Yanqun Wang

and have found that it is complete and satisfactory in all respects,  
and that any and all revisions required by the final  
examining committee have been made

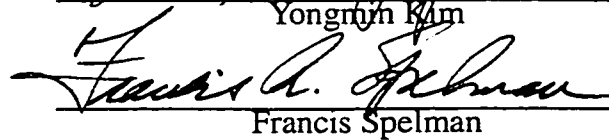
Chair of Supervisory Committee:

  
\_\_\_\_\_  
Yongmin Kim

Reading Committee:

  
\_\_\_\_\_  
David Haynor

  
\_\_\_\_\_  
Yongmin Kim

  
\_\_\_\_\_  
Francis Spelman

In presenting this thesis in partial fulfillment of the requirements for the Doctoral degree at the University of Washington, I agree that the Library shall make its copies freely available for inspection. I further agree that extensive copying of the dissertation is allowable only for scholarly purposes, consistent with "fair use" as prescribed in the U.S. Copyright Law. Requests for copying or reproduction of this dissertation may be referred to University Microfilms, 300 North Zeeb Road, Ann Arbor, MI 48106-1346, to whom the author has granted "the right to reproduce and sell (a) copies of the manuscript in microform and/or (b) printed copies of the manuscript made from microform."

Signature

Yam Wang

Date

6/11/99

# University of Washington

## Abstract

Analysis of defibrillation efficacy and investigation of impedance cardiography with finite element models incorporating anisotropic myocardium

Yanqun Wang

Chairperson of the Supervisory Committee:

Professor Yongmin Kim  
Department of Bioengineering

Increasing defibrillation efficacy by estimating and lowering the defibrillation threshold (DFT) is important in positioning implantable defibrillating electrodes. We analyzed the relation between the experimentally-measured DFTs and the myocardial voltage gradients (VGs) simulated by the 3D subject-specific isotropic finite element models. Our data show a statistically significant correlation between the DFT and the left ventricular VG, with its septal region being most significant ( $cc = 0.74$ ). The DFT correlation with the RV and atrial VG, however, is not significant. We then estimated the errors in this correlation due to the isotropic simplification in modeling myocardium by elastically mapping published myocardial fiber data into our animal models, and found that the error in the estimated myocardial VG should have only a small effect on the above estimated correla-

tion. Because the correlation is also affected by the accuracy of the measured resistivities of anisotropic tissues, e.g., myocardium and skeletal muscle, we studied the geometric effects of a four-electrode probe on the measurement of anisotropic resistivities. Our simulation shows that the measured tissue anisotropy ratio is decreased by increasing the electrode size relative to the interelectrode spacing, which is supported by our experimental measurements. We have thus provided an equation for estimating such errors from the electrode geometry.

We also studied how the band- and spot-electrode location affects the measured impedance change in impedance cardiography using realistic diastolic and systolic human thorax models. The results show that ventricular contraction, the only factor that increases systolic impedance, has a larger effect than the resulting expansion of major vessels and decrease in lung and aortic blood resistivities. When spot electrodes are placed on the anterior chest wall near the heart, ventricular contraction dominates and the measured impedance change at systole represents 82% of the contribution from ventricular contraction. When using band electrodes, the impedance change is a more balanced combination of the four effects. These results suggest that impedance cardiography can not directly measure stroke volume based on the whole thoracic impedance change, while spot electrodes may be more useful in detecting local physiological activities in the ventricles.

## Table of Contents

	Page
List of Figures .....	ii
List of Tables .....	iii
Introduction .....	1
Chapter 1: Analysis of Defibrillation Efficacy with Myocardial Voltage Gradient ..	3
I. Introduction .....	3
II. Methods .....	4
III. Results .....	11
IV. Discussions .....	13
V. Conclusion .....	18
Chapter 2: Estimating Effects of Myocardial Anisotropy .....	32
I. Introduction .....	32
II. Methods .....	34
III. Results .....	42
IV. Discussions .....	45
V. Conclusion .....	50
Chapter 3: Geometric Effects on Four-electrode Resistivity Measurements .....	65
I. Introduction .....	65
II. Methods .....	67
III. Results .....	70
IV. Discussions .....	72
V. Conclusion .....	75
Chapter 4: Finite Element Study of Impedance Cardiography .....	83
I. Introduction .....	83
II. Methods .....	86
III. Results .....	90
IV. Discussions .....	93
V. Conclusion .....	99
Bibliography .....	109
Curriculum Vitae .....	118

## List of Figures

Number		Page
Figure 1.1	Correlation study flow chart .....	22
Figure 1.2	Electrode configuration diagram .....	23
Figure 1.3	DFT measurement protocol .....	24
Figure 1.4	65%-tilt biphasic waveform .....	25
Figure 1.5	Myocardial regions investigated .....	26
Figure 1.6	Backward-cumulative histogram .....	27
Figure 1.7	Measured DFT <sub>50s</sub> .....	28
Figure 1.8	Computed VG <sub>80s</sub> .....	29
Figure 1.9	cc values between DFT <sub>50</sub> and VG <sub>80</sub> .....	30
Figure 1.10	Minimal VG's in whole myocardium .....	31
Figure 2.1	Electrode configuration tested .....	52
Figure 2.2	Landmark points on myocardial surfaces .....	53
Figure 2.3	Screen capture of mapping procedure .....	54
Figure 2.4	Mapped myocardial surfaces .....	55
Figure 2.5	Mapped fiber directions on myocardial surfaces .....	56
Figure 2.6	Mapped cross-wall fiber directions .....	57
Figure 2.7	Spatial change rate of mapped fiber direction .....	58
Figure 2.8	Spatial change rate of VG from isotropy to anisotropy .....	59
Figure 2.9	LV free wall's VG histogram change from isotropy to anisotropy ..	60
Figure 2.10	Septal VG histogram change .....	61
Figure 2.11	LV's VG histogram change .....	62
Figure 2.12	RV's VG histogram change .....	63
Figure 2.13	LV & RV's VG histogram change .....	64
Figure 3.1	Four-electrode technique .....	78
Figure 3.2	Simulated measurements in isotropic tissues .....	79
Figure 3.3	Simulated measurements in low-anisotropic tissues .....	80
Figure 3.4	Simulated measurements in high-anisotropic tissues .....	81
Figure 3.5	<i>In-vitro</i> experimental measurements .....	82
Figure 4.1	ICG technique .....	102
Figure 4.2	Model creation procedure .....	103
Figure 4.3	MR scans and classified images .....	104
Figure 4.4	ICG electrode configurations investigated .....	105
Figure 4.5	Simulated impedance change due to structure change .....	106
Figure 4.6	Simulated impedance change due to resistivity change .....	107
Figure 4.7	Simulation of practical electrode configurations .....	108

## List of Tables

Number		Page
Table 1.1	Tissue resistivities in FE models .....	20
Table 1.2	Correlation coefficients between $DFT_{50}$ and $VG_{80}$ .....	20
Table 1.3	Myocardial volumes .....	21
Table 2.1	Tissue resistivities in FE models .....	51
Table 2.2	Anisotropic myocardial resistivities .....	51
Table 2.3	Change in $VG_{80}$ from isotropy to anisotropy .....	51
Table 3.1	Measured muscle anisotropic resistivities .....	76
Table 3.2	Muscle anisotropy ratios in the literature .....	76
Table 4.1	Tissue resistivities in FE models .....	100
Table 4.2	Blood volume change from diastole to systole .....	100
Table 4.3	Impedance change due to structural change .....	101
Table 4.4	Impedance change due to resistivity change .....	101

## Acknowledgments

It has been quite a journey, and it is impossible to mention all the people who have helped. But some of them have had such direct and profound impact both on my research and on myself as a person that they deserve a great deal of credits. In particular, I want to thank Drs. Yongmin Kim, David Haynor, and Paul Schimpf, whose wisdom, encouragement, patience, critique, and willingness for discussion have meant so much to me. I wish you had as much joy reading my manuscripts as I had reading your comments. It is through observing your work that I realize that capable people, although different in styles, all have merits in common that are key to success - dedication, independent and logical thinking, perseverance, and effective usage of time. I want to especially thank Dr. Haynor for his tremendous help in numerous occasions on image data acquisition. I am also grateful to Dr. Francis Spelman, who provided lot of helpful discussion on my research and offered me a very memorable teaching opportunity. Sandy, it was simply a joy working with you, and I admire your teaching style and sense of humor so much that I wish I could have just a bit of that talent. I also want to thank Dr. Gust Bardy wholeheartedly, who would always find time for me from his tremendously busy schedule to provide discussions on cardiac electrophysiology and great ideas and insights on animal experiments.

Many other people have also contributed to the research projects. I want to express my sincere thanks to Mr. George Johnson, an electrical engineer in the Department of Cardiology, who helped great deal in data acquisition and measurements in the FE study of defibrillation efficacy, helped make the four-electrode probes in the study of geometric effects on the tissue resistivity measurement, and offered many useful insights and understanding on instrumentation. I also want to thank Mr. Robert Thomas and Ms. Christine Rothnie, research technicians of the Animal Laboratory of the Cardiothoracic Surgery Department in the School of Medicine at the University of Washington, who helped ensure successful completion of the experiments for the study of defibrillation efficacy. I am par-

ticularly grateful to Drs. Hiroji Akimoto, Hidenori Gohra, Kazuhiro Suzuki, and Sadahiro Sai of the Cardiothoracic Surgery Division, who performed the surgical procedures and prepared tissue samples in various studies and whose skills, collaborative spirits and patience are beyond praise.

Last but not the least, my heartfelt thanks go to my wife Yong and son Eddie, who have been my spiritual support for so many years and put up with countless evenings and weekends while I had to be away in the lab. Yong, sorry for my stubbornness, but I was just trying to do a better work.

*To My Dear Parents,*

*Wang, Jigang*

*and*

*Zhou, Jiamei*

## Introduction

Two important bioelectric phenomena are frequently encountered in the clinical environment: (1) can defibrillation efficacy be estimated using non-invasive or minimally-invasive techniques? (2) since the physiological events underlying impedance cardiography are still unclear, how can impedance cardiography provide more physiologically meaningful measurements by selecting proper electrodes and measurement locations? While answering these questions requires an enormous research effort, this dissertation attempts to provide some insight through a series of preliminary studies that used both subject-specific computer simulation and animal experiments.

Increasing defibrillation efficacy by lowering the defibrillation threshold (DFT) is an important goal in positioning implantable cardioverter-defibrillator electrodes. Clinically, the DFT is difficult to estimate non-invasively. It has been suggested that the DFT relates to the myocardial voltage gradient distribution, but this relation has not been demonstrated quantitatively. Our group performed a series of pig experiments to measure the DFTs, and created three-dimensional subject-specific finite element models to assess the correlation between the computed myocardial voltage gradient and the DFTs. However, two factors obstructed a detailed analysis of this correlation: the myocardial fiber direction and the principal myocardial resistivities, both of which are needed in the finite element models but are not readily available on a subject-specific basis.

In order to assess the effects of anisotropic electric property of myocardium, myocardial fiber direction was needed. In this study, we proposed a multiquadric-spline based elastic mapping approach to incorporate a “generalized” myocardial fiber information into a specific individual to assess the effects of the correlation between the DFT and myocardial voltage gradient. Since principal anisotropic tissue resistivities are most commonly measured with the four-electrode technique, the geometry of four-electrode arrays can affect the measurement results significantly. We studied via computer simulation the

effects of electrode diameter, electrode length, interelectrode spacing and tissue size on the accuracy of measured tissue resistivities and anisotropy ratios obtained with the widely-used four-electrode technique. We also used experimental data obtained on *in vitro* tissues to verify the simulation results.

Traditional impedance cardiography technique uses band electrodes for delivering current to and measuring voltage of the thorax. The use of spot electrodes has added a new dimension to the impedance cardiography technique, increasing the ease of electrode placement and the comfort level for patients. Research has shown that changes in thoracic impedance can have multiple causes. In this study, we proposed to use finite element modeling to investigate the sources of impedance change for both band-electrode and spot-electrode impedance cardiography, and focused on how differences in electrode location affect the contribution of different sources to changes in impedance. Realistic end-diastolic and end-systolic models were obtained from MRI images of a healthy human subject. We examined the hypothesis that impedance cardiography can be used to directly measure stroke volume based on the change in the whole thoracic impedance, and investigated whether more physiologically meaningful measurements can be obtained by using different types of electrodes and applying them at different locations.

## **Chapter 1. Analysis of Defibrillation Efficacy from Myocardial Voltage Gradients with Isotropic Finite Element Models**

### **I. Introduction**

Ventricular fibrillation (VF) is characterized by uncoordinated ventricular contractions that result in a sudden substantial drop in cardiac output. Clinical studies have shown that VF is closely related to sudden cardiac death [7]. The success of the implantable cardioverter-defibrillator (ICD) in terminating VF has led to wide clinical acceptance [8][87], and the ICD is now believed to be the most efficacious device for the prevention of sudden cardiac deaths [79]. One of the major issues concerning ICD usage is placement of the defibrillating electrodes so that the current can be optimally channeled through the cardiac muscle, particularly the left ventricular myocardium. A good electrode configuration should achieve successful defibrillation with maximal efficiency while minimizing potential injury to the patient.

Finite element (FE) models have been extensively used in studies ranging from determining the voltage gradient distributions in tissue to the optimal design of defibrillation electrodes [35][36][41][42][48]. Recently, we applied subject-specific three-dimensional (3D) FE models to investigate quantitatively the correlation between the computed and measured voltage distributions in animals under defibrillation shock and obtained an average correlation coefficient of 0.927 [36]. Our 3D FE models were based on CT images of individual subjects, and thus were anatomically subject-specific. The results demonstrated the usefulness and capability of the subject-specific FE modeling approach in defibrillation study.

Defibrillation efficacy is measured by the defibrillation threshold (DFT), the minimum effective voltage for successful defibrillation [77]. Because defibrillation outcomes

are probabilistic in that a given applied voltage will result in successful defibrillation sometimes rather than always, the DFT is defined as the voltage corresponding to a certain success rate. For example, the 50% DFT (or  $DFT_{50}$ ) is the voltage that succeeds in defibrillation in 50% of trials. In experiments performed directly on the exposed canine heart, it was observed that a voltage gradient (VG) distribution with a minimum of 3 V/cm in the whole myocardium needs to be established for successful defibrillation with biphasic waveform [32][101], suggesting that the DFT is closely related to the myocardial VG. In addition, some researchers have suggested that the influences of different myocardial regions on the DFT are different [78]. While measuring the myocardial VG *in vivo* is an invasive and very challenging task, FE modeling offers a potential practical approach to this problem.

Using animal experiments and 3D subject-specific FE models, we tested the hypothesis that the DFT is related to the VG distribution in the myocardium.

## II. Methods

Figure 1.1 shows a flowchart showing the steps in our study. Important steps are described in more detail in this section.

### A. *Animal experiments*

#### A.1 *Animal preparation*

A total of 11 Hampshire-Yorkshire Cross pigs were used in the experiments reported here. Animals were of random sex and 1 to 2 months of age, with weights ranging from 20 to 30 kg. All animal experiment protocols were in accordance with NIH standards and were approved by the University of Washington Animal Care Committee [28].

Animals were housed in the animal lab for up to 5 days before the experiments. At the beginning of the experiment, the animal was sedated with an intramuscular injection of ketamine (22 mg/kg), acepromazine (1.1 mg/kg), and atropine (0.05 mg/kg). The animal

was then given halothane by mask and following endotracheal intubation or tracheotomy, general anesthesia was maintained with halothane (1-2%) in 100% oxygen (O<sub>2</sub>) until instrumenting the animal was complete. Halothane was then slowly decreased, and pentobarbital sodium (30 mg/kg) was used as an anesthetic maintenance agent for the duration of the experiment. Throughout the experiment, the animal was ventilated with a Harvard respirator and was placed on 5 cm H<sub>2</sub>O positive end-expiratory pressure (PEEP). The arterial partial pressure of carbon dioxide (CO<sub>2</sub>) was maintained between 35-45 mmHg, and the animal was oxygenated with 100% O<sub>2</sub>. A warming blanket was also provided to maintain the animal's body temperature at 37°C. Intravenous antibiotics of cefazolin (50 mg/kg) and gentamicin (2.5 mg/kg) were administered every 4 hours.

Intravascular catheters were placed in the femoral artery and vein to continuously monitor central venous pressure and arterial pressure. The electrocardiogram was monitored for the animal's physiological condition, fibrillation induction and defibrillation conversion. Blood samples were taken approximately every 2 hours for measurements of electrolyte (K<sup>+</sup> and Mg<sup>+</sup>) concentration. Arterial blood gases, pH and hematocrit were recorded every 10-45 minutes. Body temperature and respiration rate were also monitored.

The first three of the following implantable electrode configurations were tested on each pig, except for pig #11 in which all four configurations were tested. The cathode was always a catheter electrode (Medtronic, Minneapolis, MN, model 6884) in the apex of the right ventricle (RV) placed via the right jugular vein. The anode was placed subcutaneously and was one of the following: (1) an anterior patch (Medtronic model 6895) electrode placed over the cardiac apex of the left ventricle (LV), (2) an anterior 40-cc can electrode (Medtronic model 10438-40) placed below the left clavicle, (3) a posterior 40-cc can electrode placed below the left scapula, (4) an anterior patch electrode placed in the upper right abdomen (Figure 1.2). At the beginning of the experiment, anode pockets were made, and the catheter was fluoroscopically placed in the RV with the tip screwed into the apical myocardium. The position of the RV catheter was verified afterwards by pacing and was checked intermittently by fluoroscopy throughout the experiment.

## A.2 DFT measurement

After animal preparation and placement of the defibrillation electrodes, the DFT was measured for each electrode configuration. Figure 1.3 is a flowchart of the DFT measurement protocol.

The DFT measurement began with an initial guess of the  $DFT_{50}$  as 800 V (Step 2). Then, a series of fibrillation-defibrillation episodes ensue through which the DFT was estimated iteratively (Steps 3-8). For each episode, VF was induced at the end of expiration by applying a 60-Hz current to the heart (Step 3), and a test defibrillation shock from the implanted electrodes was delivered (Step 4). If defibrillation was unsuccessful, a rescue shock was applied using an external transthoracic defibrillator (Step 5). The DFT and its 95% confidence interval (CI) were then calculated (Steps 6 & 7) and the next defibrillation voltage to be used was suggested (Step 8) through a mathematical procedure (below). These testing episodes for a particular electrode configuration were stopped when either the 95% CI of the DFT was less than 150 V or the total number of defibrillation shocks (including rescue shocks) exceeded 30, whichever occurred first. For most configurations, the 95% CI of the DFT at the completion of the procedure was reduced to 150 V, and it was always less than 170 V. A 3-minute interval was allowed before the next defibrillation voltage was tested.

There are two main types of methods to measure the DFT, reflecting two different views of the DFT concept. The first method is the voltage stepping test based on the concept that the DFT is a transition voltage between defibrillation success and failure [14][63]. This concept has now evolved to a statistical concept of the DFT as the threshold intensity that can successfully defibrillate on half of the trials. Rather than describing the transition voltage by a single value, the second method views the DFT as having a distribution that peaks at a certain voltage [20][47]. Therefore, the probability of defibrillation success is a monotonically increasing (usually sigmoidal) function of applied voltage. The first method is deemed qualitative and cannot define a DFT success rate other than 50%. We consider the concept of probabilistic DFT more appropriate. Therefore, we adopted a

logistic regression approach in which a sigmoidal curve was fit to a series of binary (success/failure) points on a graph of success rate vs. defibrillation voltage [31]. The sigmoidal relation was parameterized as follows:

$$p(V) = \frac{e^{(V - \text{DFT}_{50})/b}}{1 + e^{(V - \text{DFT}_{50})/b}} \quad (1.1)$$

where  $p(V)$  is the probability of defibrillation success for an applied voltage  $V$ , and  $b$  reflects the transition width of the sigmoidal curve. A computer program was developed to run on-line during the fibrillation-defibrillation episodes, giving continuously-updated estimates for  $\text{DFT}_{50}$  and  $b$  along with their 95% CIs (Steps 6 & 7). The program also calculates the test voltage for the next defibrillation episode, which will maximally reduce the 95% CI of  $\text{DFT}_{50}$  based on the results of the previous trials (Step 8), thus minimizing the number of defibrillation shocks on the animal. When the CI of  $\text{DFT}_{50}$  is sufficiently small or the total number of defibrillation shocks is over 30, the iterative process is terminated, and the  $\text{DFT}_{50}$  value is obtained. Our definition of the  $\text{DFT}_{50}$  and the DFT defined by a single transition voltage are essentially equivalent ([87], pp. 236-256), which allows comparison of our results with those in the literature. Note that from Eq. (1.1), a DFT for any success rate can be obtained, such as the  $\text{DFT}_{80}$  that is found by solving  $p(\text{DFT}_{80}) = 0.8$ .

A specially-designed high voltage pulse generator was used to provide a 65%-tilt biphasic waveform (Figure 1.4) for defibrillation with selectable voltage and pulse width. The actual delivered defibrillation voltage and current were measured using a PC-based data acquisition system controlled by a Windows program.

### A.3 CT scan

To build a subject-specific FE model, each animal was imaged via a CT scanner. At the completion of an experiment, the anesthetized animal was administered a blood vessel contrast agent (Renografin-76, 6 mg/kg) that makes the heart chambers and blood vessels show up with higher intensity in the CT images, facilitating later image segmenta-

tion. The animal was then immediately euthanized and transported to a nearby CT scanner (General Electric 9800 HTD, Milwaukee, WI) for a post-mortem scan. The post-mortem (end-diastolic) heart resembles the heart in VF, where ventricular emptying is ineffectual. The endotracheal tube was clamped at end-expiration to prevent inflation of the lungs, which resembles the lungs in VF. Before scanning, all stimulating electrodes (metal) except the RV catheter were replaced with plastic phantoms to avoid artifacts in the reconstructed CT images. These phantom markers were easily identifiable in the CT images.

The scanning was done in two stages. The pig's heart was first scanned to locate the RV catheter electrode. The catheter electrode was then removed to avoid artifacts on the CT images so that the heart chambers could be easily segmented. After this, 3-mm scanning from neck to lower abdomen (approximately 130 slices) was performed.

### ***B. Subject-specific FE models***

The CT images have 512 x 512 pixels (FOV = 300 mm) with 12 bits/pixel. Using a semi-automatic tissue classification program [76], these images were classified into different tissue types, and the location of the anode was determined from the imaged plastic phantom while the cathode was located from the scan of the RV catheter. Based on the classified images for each animal, multiple 3D FE models were constructed, one for each electrode configuration. Each tissue class was assigned a resistivity adopted from values published in the literature [25][72] (Table 1.1). Skeletal and cardiac muscles were modeled using isotropic resistivities.

By modeling biological tissues including myocardium as passive conducting media, voltage in the tissues as a result of an external electrical stimulation follows Laplace's equation

$$\nabla \cdot \sigma(\nabla V) = 0 \quad (1.2)$$

where  $\sigma$  is the assigned conductivity value of the tissues and  $V$  is the voltage to be solved for. The FE method, a numerical modeling technique suitable for solving partial differen-

tial equations in an irregular geometric domain, has been successfully used to solve Eq. (1.2) in computing the electric field in the thorax as a result of external stimulation [40][48]. In order to apply the FE method, tissue domain was discretized into 3D elements, with  $\sigma$  constant in each element and  $V$  interpolated using nodal voltages [102].

Over the past several years, our group has developed both the fixed-mesh-size and adaptive-meshing FE solvers [11][70]. Both solvers automatically generate FE meshes directly from segmented tomographic images, which is useful for the rapid generation of patient-specific models because tissue boundaries in the human thorax are too complicated to generate with solid geometry models. Contrast to the fixed-mesh-size FE algorithm, our adaptive FE algorithm adaptively refines the meshes according to the local current-density error. Adaptive mesh refinement results in models with varying mesh densities, e.g., higher density in the heart and near the electrodes, and lower density in the lungs and away from the electrodes. Mesh adaptation uses local estimates of the current density error to identify regions for which the mesh should be refined, and continues iteratively until the global current density error falls below a pre-defined threshold, thus allowing a much more efficient computation than the fixed-mesh-size FE approaches [70]. For additional details, we refer the readers to a comprehensive description of the algorithm in [70].

Our FE models use uniform hexahedral (cubic) elements [102], with each node being the vertex of a voxel in the classified images. The element size in the FE models was 2.3 mm x 2.3 mm x 3.0 mm obtained by averaging the resistivities of 4x4 pixels in each classified image. The number of elements in the models ranged from 600,000 to 900,000.

Dirichlet (constant voltage) boundary conditions were applied at the anode and cathode electrodes. A Neumann (zero normal flux) boundary condition was applied at all the external surfaces of the model. The resulting system of linear equations was solved using the Jacobi conjugate gradient (JCG) method on an IBM RS6000 workstation with 128 Mbytes of memory. Model construction and solution for each configuration took approximately 2.5 hours.

### C. DFT correlation with the voltage gradient distribution

From the model solutions for each electrode configuration, tissue voltages were obtained and their partial derivatives were evaluated along the three orthogonal coordinate axes, from which we extracted the VG magnitude in the myocardium and its subregions (Figure 1.5). Then, we calculated the backward-cumulative histograms  $H(vg)$  via

$$H(vg) = \int_{vg}^{\infty} h(x)dx, \text{ where } x \text{ is the VG magnitude and } h(x) \text{ is the normalized VG histogram.}$$

A typical backward-cumulative histogram in the myocardial region from one animal model is shown in Figure 1.6. By definition,  $H(vg)$  is the proportion of the myocardial region of interest that has a voltage gradient of at least  $vg$ . For a given percentage  $p$ , we define  $VG_{100*p}$  by solving  $H(VG_{100*p}) = p$ ; in other words,  $VG_{100*p}$  is the minimal voltage gradient present in  $100*p\%$  of the myocardium. For example, when  $p = 80\%$ ,  $VG_{80}$ , the minimal voltage gradient over 80% of the entire myocardium, can be found by solving  $H(VG_{80}) = 80\%$ , where  $H(vg)$  is the backward-cumulative voltage gradient histogram for the entire myocardium.

We are interested in the relation between the VG and the DFT. For example, if two electrode configurations have different backward-cumulative voltage gradient histograms and different  $VG_{80}$ s obtained from an FE animal model (Figure 1.6) for the same applied defibrillation voltage, which one of them will have the lower measured DFT in experiment? Studies have suggested that a reliable defibrillation requires a certain VG (about 5 to 6 V/cm for monophasic, and 3 V/cm for biphasic defibrillation waveforms) to be established in a critical mass of the myocardium [32][51][94][100][103]. Although the size of this critical mass has not been accurately determined, it has been hypothesized to range from 75% ([87], pp. 29-36) to 90% [100] of the ventricular mass. In this study, we chose to examine the relationship of the  $VG_{80}$  to the DFT. The calculation of  $VG_{80}$  from the FE models is more accurate than that of  $VG_{90}$  because at 80% level more elements are available for calculation and the discretization error in the FE models is smaller. A certain VG

being required in a critical mass of the myocardium implies that the electrode configuration with the higher VG in Figure 1.6 (configuration #1) can establish a voltage gradient of at least 3 V/cm with a lower applied voltage than the other configuration (configuration #2), and that configuration #1 should have the lower DFT. Thus, the specific hypothesis we set out to test is that for an electrode configuration, the higher the  $VG_{80}$  for a fixed applied defibrillation voltage, the lower the measured  $DFT_{50}$  will be. Spearman's rank correlation method was used to calculate the rank correlation coefficient ( $cc$ ) and to test its significance [97]. Because we are also interested in the subregions of the myocardium (Figure 1.5), we tested the above hypothesis for these subregions as well. Since the governing Laplace's equation for FE models is linear, the model solutions are proportional to the applied boundary conditions. Thus, the choice of the applied defibrillation voltage (the boundary condition) is arbitrary, and we chose to apply 400 V.

### III. Results

#### A. *DFT measurements*

From 34 electrode configurations in 11 pigs, a total of 34  $DFT_{50}$ s were measured as shown in Figure 1.7.

#### B. *DFT correlation with the voltage gradient distribution*

After the FE model for each configuration in each animal was created and solved, the VG magnitude values of all the elements in the whole myocardium and its subregions (Figure 1.5) were extracted. The backward-cumulative histograms of the VG magnitude for the myocardial regions were calculated. From 34 electrode configurations in 11 pigs, we obtained 34  $VG_{80}$ s for the entire myocardium, atria, ventricles, RV, LV, LV free wall, and septum, respectively (Figure 1.8(a) - (g)).

The purpose of Spearman's method is to assess the correlation of the ranks of observations for the two variables. To test the hypothesized relation that the higher the  $VG_{80}$ , the lower the  $DFT_{50}$ , all  $DFT_{50}$  measurements were ranked from high to low (i.e.,

rank 1 is the highest) while all the simulated  $VG_{80}$  values were ranked from low to high (i.e., rank 1 is the lowest). Then,  $cc$  was calculated using Spearman's formula [97]:

$$cc = 1 - \frac{6 \sum_{i=1}^{N_c} (R_{D,i} - R_{V,i})^2}{N_c^3 - N_c} \quad (1.3)$$

where  $N_c = 34$  (number of configurations), and  $R_{D,i}$  and  $R_{V,i}$  are the  $DFT_{50}$  and  $VG_{80}$  rank for the  $i$ th configuration, respectively. Spearman's test was then applied to the null hypothesis  $H_0: cc = 0$ . The calculated correlation coefficients, termed cross-animal  $cc$ , are listed in Table 1.2 with their  $p$  values (first row). The whole myocardium, ventricles, LV, LV free wall, and septum have the highest  $cc$  values, and  $H_0$  is rejected for these regions at the 5% significance level. Neither the atria nor the RV shows any statistically significant correlation between  $VG_{80}$  and  $DFT_{50}$ .

In addition to assessing the correlation collectively over 11 pigs, we also assessed the correlation for each pig since each pig had 3 - 4 different electrode configurations, enough to allow Eq. (1.3) to be evaluated ( $N_c = 3$  or 4). These correlation coefficients are termed as within-animal  $cc$ . Figure 1.9(a) - (g) show the within-animal  $cc$  values for each pig for the entire myocardium, atria, ventricles, RV, LV, LV free wall, and septum, respectively. Table 1.2 also lists the average of these  $cc$  values from 11 pigs (second row). Compared to the cross-animal  $cc$ , the averaged within-animal  $cc$  is much higher for the septum (0.74), but is not significantly different for the other myocardial regions. Again, the whole myocardium, ventricles, LV, and LV free wall as well as septum demonstrate significant correlation.

The above studies used the mean  $DFT_{50}$  values for estimating the correlations. Due to our  $DFT_{50}$  measurement protocol in Figure 1.3, each estimated  $DFT_{50}$  has a distribution characterized by its mean and CI. In order to examine the variation in the correlation

results due to the uncertainty in  $DFT_{50}$  estimation, we resampled 10,000  $DFT_{50}$  values from the  $DFT_{50}$  distribution for each electrode configuration and repeated the above correlation studies. More than 50% of the resampled  $DFT_{50}$ s resulted in the same correlation coefficients as those estimated using the mean  $DFT_{50}$ s, which justifies the above correlation study using only the mean  $DFT_{50}$  values.

#### IV. Discussion

Estimating the DFT for a specific patient is very desirable in clinical environments. Current practice often requires the use of multiple fibrillation-defibrillation testing trials during the ICD implantation procedure, which presents a risk to the patient. Research on correlating the DFT with various clinical attributes has produced disappointing results. Raitt *et al.* [62] examined the clinical predictors of the DFT using an electrode configuration with an 80-cc left anterior can and an RV catheter electrode. The clinical predictors examined were sex, age, weight, body surface area, resting heart rate, QRS interval, LV mass, posterior wall thickness, septal wall thickness, and ejection fraction. Except for the LV mass ( $cc = 0.45$ ) and LV end-diastolic diameter ( $cc = 0.40$ ), no clinically relevant correlation was found between these variables and the DFT ( $cc = 0.03 - 0.36$ ). This reflects the fact that the complex physiological and cellular events are not adequately represented by general clinical information.

Studies have shown that at the cellular level, transmembrane potential is closely related to the extracellular voltage gradient [87]. As the transmembrane potential and the stage of polarization of thousands of myocardial cells determine the defibrillation outcome, it is reasonable to assume that the DFT is related to the VG distribution in the myocardium. Our study attempted to quantify this relation by way of animal experiments and FE modeling of each animal.

### ***A. Correlation of DFT with voltage gradient distribution in the atria, RV, and LV***

Although the size of the critical mass for successful defibrillation is not known precisely, it is suggested by experiments and simulations to be close to 80% of the ventricular mass [87][75]. Based on this, we assessed the correlation between the  $DFT_{50}$  and  $VG_{80}$  in the entire myocardium, atria, RV, LV, LV free wall, and septum. Here,  $VG_{80}$  is defined as the minimal voltage gradient established in 80% of each of the above myocardial regions.

In the first row of Table 1.2, cross-animal  $cc$  values for various myocardial regions were calculated between the 34 computed  $VG_{80}$  values in those regions and 34  $DFT_{50}$  measurements, all of which were obtained from 11 pigs. This ignores possible differences in resistivities among animals since our FE models account for only the individual anatomical variations while assuming generic tissue resistivities. In contrast, the within-animal  $cc$  values are much less affected by the inter-animal difference in resistivities. However, because each within-animal  $cc$  value is estimated from 3 to 4 pairs of the  $VG_{80}$  and  $DFT_{50}$  data, the estimation may contain a large standard deviation. By averaging the within-animal  $cc$  values over 11 pigs, the averaged  $cc$  contains less deviation than each within-animal  $cc$ . Because of this averaging, the  $p$  values for the averaged within-animal  $cc$ 's are not available. When the averaged within-animal  $cc$  and cross-animal  $cc$  values are significantly different, it may indicate that the inter-animal difference is significant. From Table 1.2, only the septum demonstrates a significant difference between the cross-animal  $cc$  and averaged within-animal  $cc$ , which will be discussed later.

In Table 1.2, the two types of  $cc$  values are similar for the whole myocardium, atria, ventricles, RV and LV. The whole myocardium, ventricles and LV have much higher and much more statistically significant correlations than the atria and RV. In view of the fact that on average the LV volume is about 76% of the entire myocardium and 82% of the ventricular volume (Table 1.3), the above results simply reflect that it is the LV's influence that makes the  $cc$  values for the whole myocardium and the ventricles significant. In com-

parison, the atria and RV appear insignificant in the relation between the  $DFT_{50}$  and VG distribution. The relative importance of the LV compared to the RV and atria in defibrillation success is well established [87]. Oeff *et al.* [56] showed that the fraction of the LV mass encompassed by patch electrodes, as measured from CT images, is more predictive of the DFT than any other myocardial region. As the LV mass accounts for most of the heart both anatomically and functionally, this result is not surprising.

It is worth noting from Table 1.3 that the myocardial size of the animals used in this study varies significantly. The maximal heart volume (pig #4, 5671 voxels) is more than twice the minimal heart volume (pig #11, 2226 voxels), and the maximal volumetric ratio of the septum to LV is 0.36 (pig #10) while the minimal ratio is 0.20 (pig #8). This fact supports the use of our subject-specific 3D FE models, which can account for individual anatomical variations and has been shown to play an important role in simulating bioelectric phenomena in an individual subject [35][36].

### ***B. Importance of the septum***

Although the cross-animal  $cc$  values do not show a significant difference between the septum and the LV free wall, the within-animal  $cc$  values averaged over 11 pigs show that the minimal voltage gradient in 80% of the septum correlates much better with the  $DFT_{50}$  than the LV free wall and the entire LV. The importance of the septum in defibrillation success has also been suggested by other researchers. Singer *et al.* [78] observed that transseptal defibrillation was superior to conventional transvenous defibrillation. They found that compared to the usual transvenous defibrillation configurations (cathode in the RV apex, and anodes placed subcutaneously and in the superior vena cava), a transseptal configuration (cathodes in the RV apex and the RV outflow tract, and subcutaneous anode) demonstrated a higher success probability at any voltage setting and lowered the required energy by 1/3, while the impedance was about the same. Guse *et al.* [29] showed that a configuration (LV catheter and four cutaneous patches) that has a larger coverage of the septum than the conventional transvenous configuration also produced a lower DFT. Similar results were also shown by Oeff *et al.* [56], who observed that the absolute and relative

amount of the septal mass encompassed by the patch electrodes is a more important determinant of the DFT than the patch-encompassed free wall mass. That the septum may be more important is reasonable because the septum contains the Purkinje fibers. These Purkinje fibers are important in the sequential excitation of myocardial cells, which may be a contributing factor in determining defibrillation outcome. The fact that the averaged within-animal  $cc$  value is significantly higher than the cross-animal  $cc$  value only for the septum may suggest the following: (1) the septum has different tissue properties from the LV free wall and (2) the septal properties vary more than the LV free wall among animals. This, however, requires further investigation.

We also investigated the effect of the size of the critical mass on the correlation between the  $DFT_{50s}$  and the myocardial voltage gradients. As we changed the critical mass proportion from 80% to 70% and 90%, the rank  $cc$  values between the  $DFT_{50s}$  and VGs of the LV, LV free wall and septum were reduced by up to 11% (data not shown), while the  $cc$  values for the atria and RV remained insignificant. When the critical mass proportion was reduced from 80% to 50%, the  $cc$  values generally decreased by up to 20%. Although the change is gradual, a critical mass proportion between 70% and 90% provided the maximal  $cc$  values for the LV and its subregions. This result indirectly points to the existence of a critical mass for successful defibrillation.

We also varied the DFT success rate from 50% to 80% (i.e., from  $DFT_{50}$  to  $DFT_{80}$ ) to observe the change in correlation between the DFT and the myocardial voltage gradient. The cross-animal  $cc$  values between the  $DFT_{50s}$  and the minimal voltage gradients in those myocardial regions studied above were 10-15% higher than those between the  $DFT_{80s}$  and the minimal voltage gradients. Although this difference is not significant, that the correlation is better for the  $DFT_{50s}$  than the  $DFT_{80s}$  may be due to the smaller variation in the estimated  $DFT_{50}$  than that in the estimated  $DFT_{80}$  as a result of the DFT estimation procedure.

Although our results show a statistically significant relationship between the DFT and the  $VG_{80}$  in some parts of the myocardium, this relationship is not strong enough to be deterministic. Many factors may contribute to this result, particularly the dependence of the defibrillation outcome on the myocardial fiber orientation relative to the defibrillation-induced voltage gradients. Tung *et al.* [88] and Bardou *et al.* [6] demonstrated through *in vitro* experiments on isolated myocardial cells that the cell stimulation thresholds depend on the cells' orientation with respect to the electric field and were lowest when the direction of the electric field intensity was aligned parallel to the long axis of the myocardial fibers. This result was supported by *in vivo* animal experiments [5][34]. Analysis using a simple myocardial-cell model has shown that the voltage drop across the cell membrane is critically dependent upon the size, geometry, and orientation of the cell when placed in an electric field ([87], pp. 225-232). Myocardial cells have a long shape with length-to-diameter ratio of about 5 to 1. The more in parallel a myocardial cell lies to the electric field, the longer the span of the cell in the direction of the field, and the larger the voltage drop across the membrane, the more likely the cell will be stimulated. In addition, myocardium has been shown to have significant anisotropy, with intracellular anisotropy ratio larger than extracellular anisotropy ratio [59][60]. An investigation of the separate effects of intracellular and extracellular anisotropies requires the usage of bidomain models. Simulating excitation by a unipolar extracellular cathode, Sepulveda *et al.* [74] have demonstrated a more complex polarization pattern for unequal intracellular and extracellular anisotropy ratios in bidomain models showing both depolarization and hyperpolarization in adjacent areas than in monodomain models showing only a depolarization pattern. Bidomain models may also allow inclusion of other physiological complexities, such as nonlinear electrical characteristics of the cell membrane [67]. Because we used monodomain, isotropic FE models and did not extract VG components relative to the fiber direction, we were unable to assess these effects.

### C. Minimal voltage gradient for reliable defibrillation

We also attempted to verify the reported finding that a certain voltage gradient is needed in the myocardium for reliable defibrillation [32][101]. Zhou *et al.* [101] found in experiments that a  $DFT_{80}$  voltage (biphasic) establishes a minimum voltage gradient of 3 V/cm in the myocardium. In view of the limitations that there are areas in the myocardium that are not easily accessible, the electrodes to measure the voltage gradient cannot cover the entire myocardium. We applied  $DFT_{80}$ s, computed from Eq. (1.1), to our animal models and calculated the resulting minimal voltage gradient magnitude in 80% of the entire myocardium. The minimal voltage gradient magnitudes from 34 electrode configurations in 11 pigs are shown in Figure 1.10. It can be seen that 97% of the configurations (33 out of 34) have a minimal  $VG > 3.1$  V/cm, and 79% of the configurations (27 out of 34) have a minimal  $VG > 5$  V/cm. This result is in agreement with the experimental finding about the minimal myocardial voltage gradient necessary for reliable defibrillation.

## V. Conclusions

Although experiments have suggested the existence of correlation between the myocardial voltage gradient and the defibrillation efficacy described by DFT [32], this relation has not been quantified. In this study, using 3D subject-specific FE modeling, we obtained evidence to support the hypothesis that for an electrode configuration, the higher the  $VG_{80}$  magnitude in the myocardium with a fixed defibrillation voltage applied, the lower the measured  $DFT_{50}$ . In particular, we found significant correlations between  $VG_{80}$  in the LV and its subregions and the measured  $DFT_{50}$ , as also suggested by some experimental findings reported in the literature. However, whether the minimal voltage gradient in the myocardium can be used to compare different electrode configurations and predict defibrillation efficacy for a given configuration still needs investigation.

The future work may include expanding the FE models from monodomain to bidomain, incorporating muscle anisotropy in both intracellular and extracellular spaces, and extracting the components of voltage gradient parallel and perpendicular to the myocardial

fiber direction will enable us to investigate our empirical findings in this study more deeply. Our next step is to investigate how the complex myocardial fiber orientation affects the voltage gradient distribution in the heart and the correlations between the  $VG_{80}$  in the myocardium and the  $DFT_{50}$ . Although actual fiber orientations cannot be seen on CT or MRI images, models defining the relationship between the orientation of the heart's long axis and that of the myocardial fibers based on experimental measurements are available [54]. The anisotropy ratios of various muscles are well studied and are available [21][27][59][60][69][81][99]. Skeletal muscle fibers need not to be modeled for the study of the relationship between the  $VG_{80}$  and  $DFT_{50}$  as research has shown that myocardial  $VG_{80}$  is much less sensitive to the skeletal muscle than to the myocardium [35]. The next Chapter describes our research on how the incorporation of the myocardial anisotropy affects estimation of myocardial  $VG_{80}$ , which will allow us to further examine the validity of the correlation results between the  $VG_{80}$  and the  $DFT_{50}$  obtained in this Chapter.

TABLE 1.1. Tissue resistivities used in FE models

Tissue type	Resistivity ( $\Omega$ -cm)
blood	154
bone	16000
fat	2180
liver	673
lung	1500
myocardium	420
skeletal muscle	700
skin	1500
stomach	800

TABLE 1.2. Correlation coefficients (cc) between the DFT<sub>50</sub>s and VG<sub>80</sub>s in the myocardial regions

Regions	Whole Heart	Atria	Ventricles	RV	LV	LV free wall	Septum
cross-animal cc	0.55 ( $p < 0.001$ )	-0.14 ( $0.2 < p < 0.5$ )	0.57 ( $p < 0.001$ )	0.15 ( $0.2 < p < 0.5$ )	0.56 ( $p < 0.001$ )	0.60 ( $p < 0.001$ )	0.54 ( $0.001 < p < 0.002$ )
averaged within-animal cc	0.60	-0.26	0.60	0.14	0.57	0.53	0.74

TABLE 1.3. Number of elements of the myocardial regions in FE models

Pig #	Heart	Atria	Ventricles	RV	LV	LV Free wall	Septum
1	3649	401	3248	759	2489	1778	711
2	4930	372	4558	1025	3533	2627	906
3	2855	248	2607	503	2104	1475	629
4	5671	501	5170	922	4248	3033	1215
5	3454	270	3184	658	2526	1802	724
6	3441	164	3277	657	2620	1874	746
7	3361	290	3071	356	2715	1960	755
8	2256	143	2113	391	1722	1370	352
9	3314	132	3182	517	2665	1943	722
10	3610	110	3500	484	3016	1934	1082
11	2226	157	2069	251	1818	1212	606
<b>Total</b>	<b>38767</b>	<b>2788</b>	<b>35979</b>	<b>6523</b>	<b>29456</b>	<b>21008</b>	<b>8448</b>

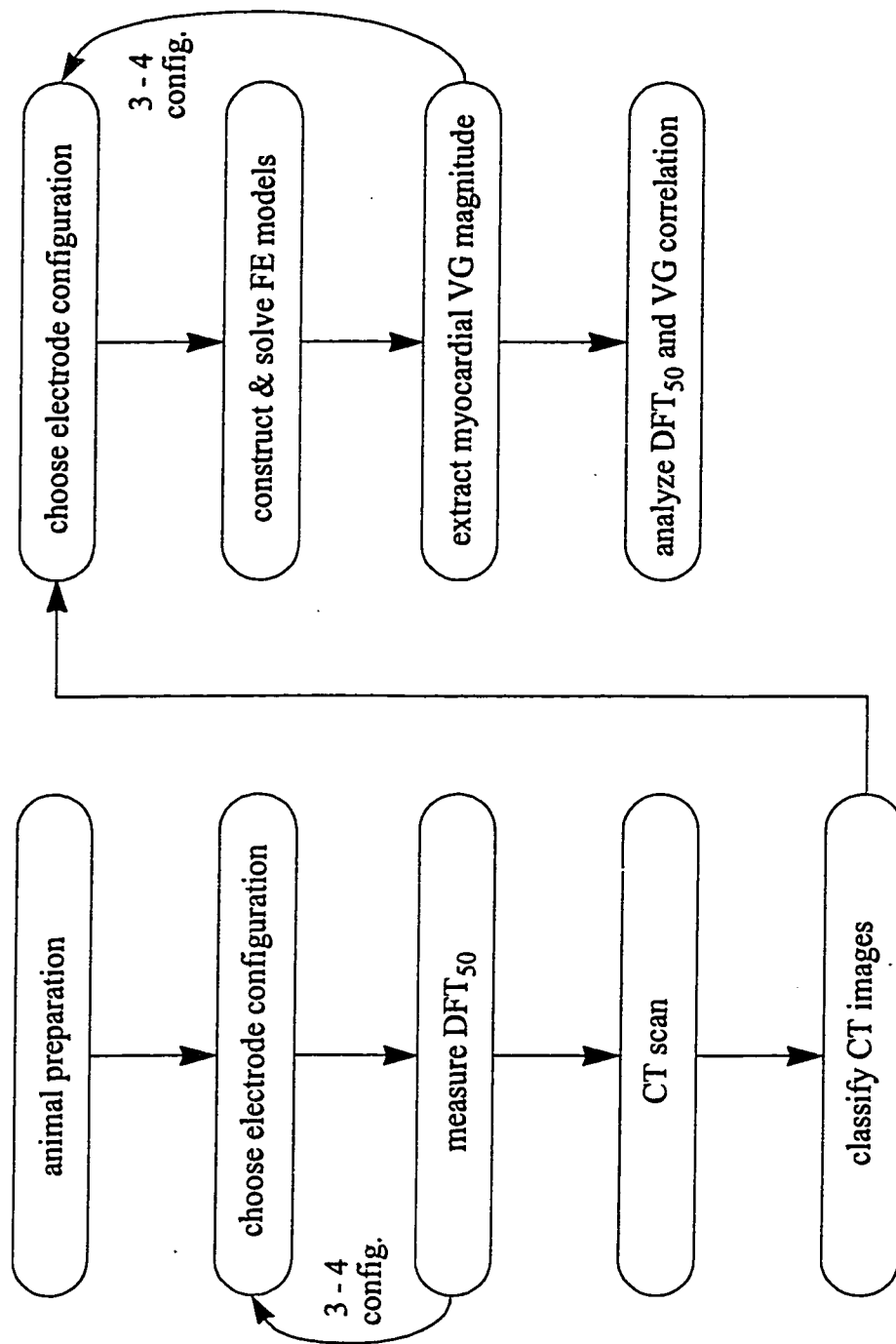


FIGURE 1.1. Flowchart of the study of correlating the measured DFT with the calculated VG magnitude.

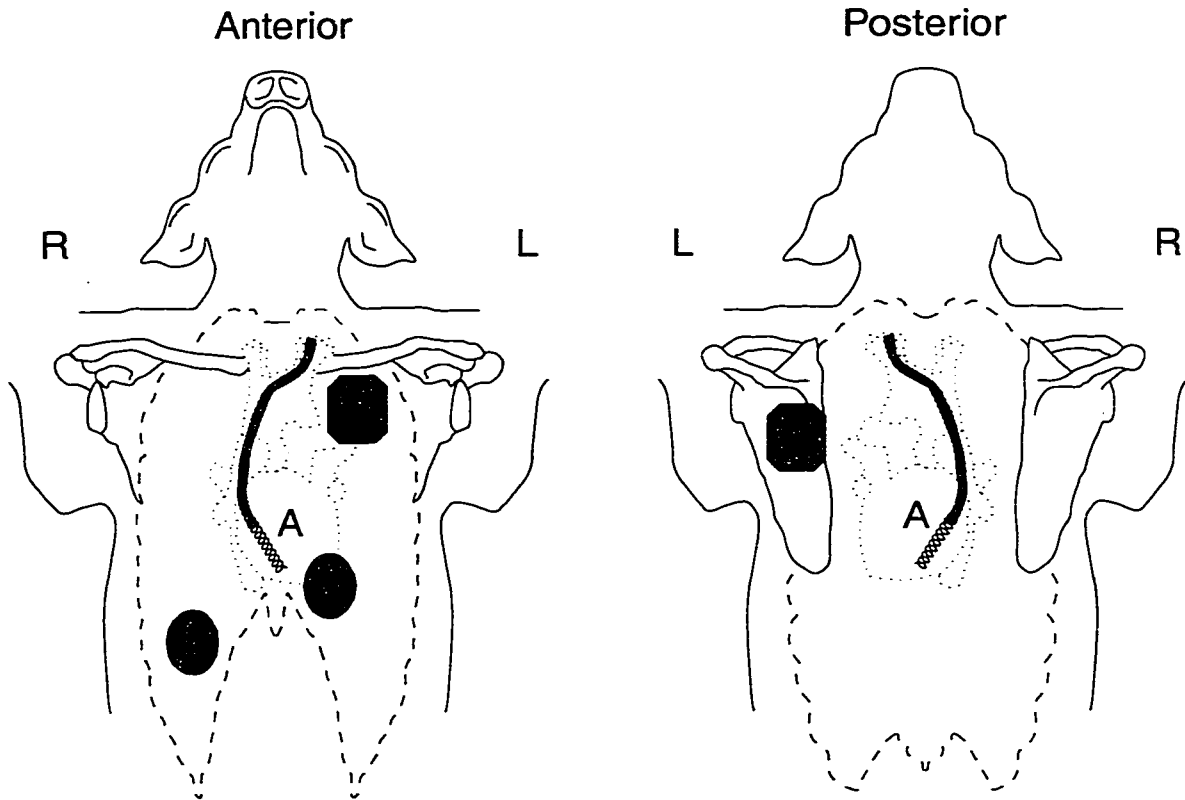
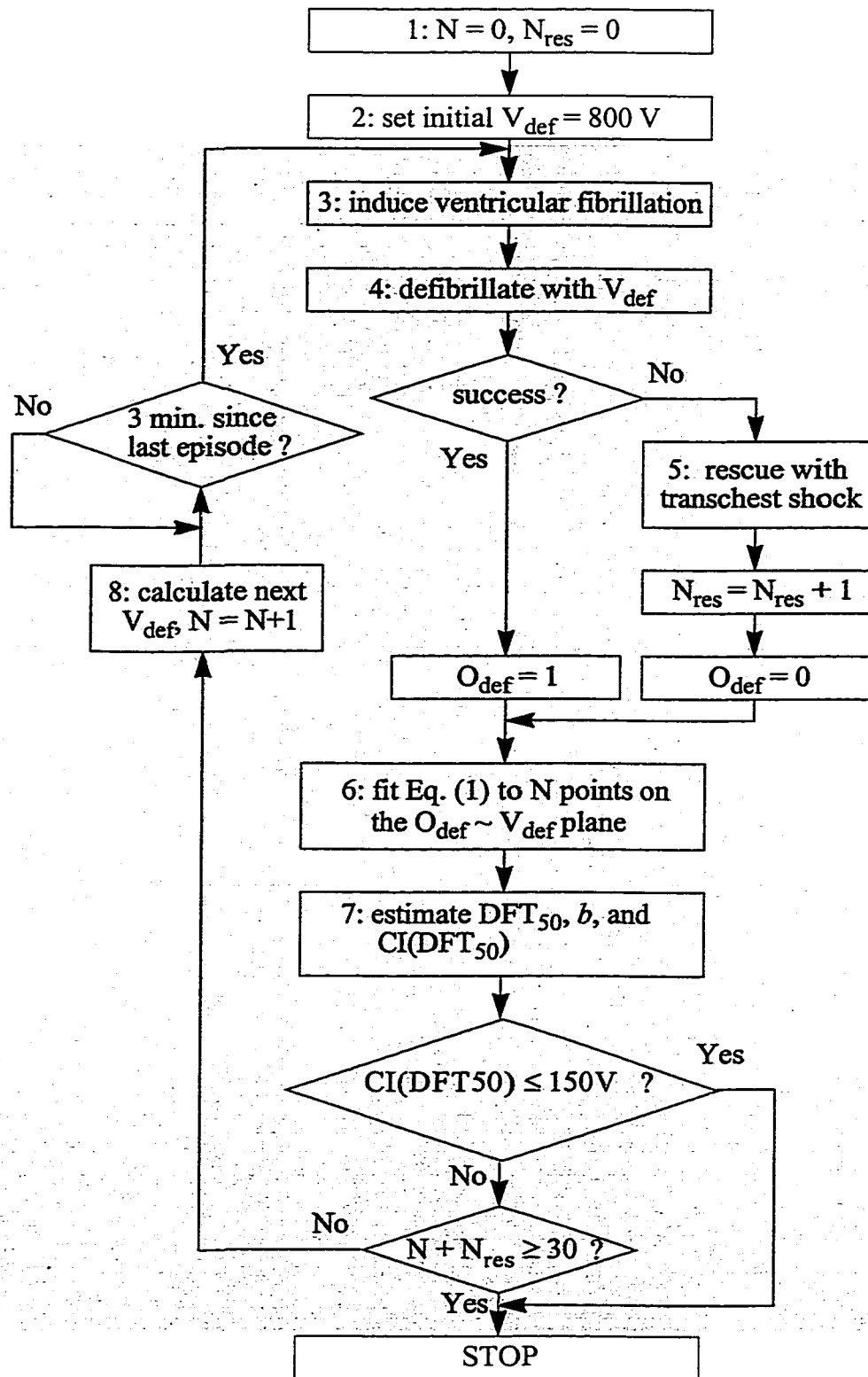


FIGURE 1.2. Schematic diagram of the electrode configurations used in the experiments: configuration 1: anterior chest patch electrode (1) / RV catheter electrode (A); configuration 2: anterior can (2) / RV catheter (A); configuration 3: posterior can (3) / RV catheter (A); configuration 4: upper right abdomen patch (4) / RV catheter (A). The dashed lines outline the rib cage, while the dotted lines show the heart.

FIGURE 1.2. Flowchart of the DFT measurement protocol. The shaded area is an iterative part consisting of a series of fibrillation-defibrillation episodes. N: number of defibrillation episodes;  $N_{\text{res}}$ : number of rescue shocks;  $V_{\text{def}}$ : defibrillation voltage;  $O_{\text{def}}$ : defibrillation outcome (1-success, 0-failure);  $\text{DFT}_{50, b}$ : see Eq. (1.1); CI: 95% confidence interval.



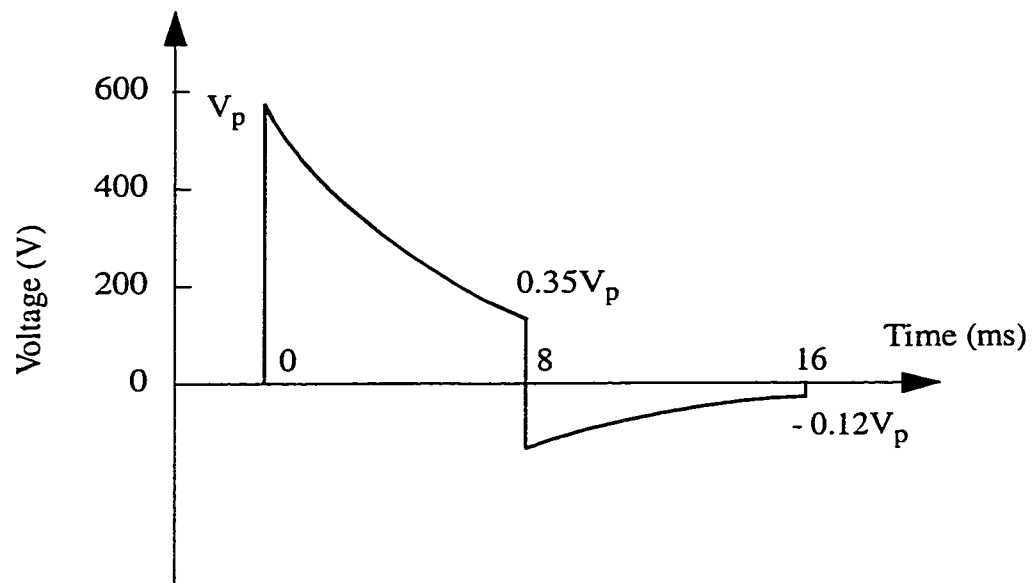


FIGURE 1.4. A typical 65%-tilt biphasic waveform used in high voltage defibrillation shocks. When the voltage drops to  $0.35V_p$ , the phase is flipped. The waveform terminates when the voltage is  $-0.12V_p$ .

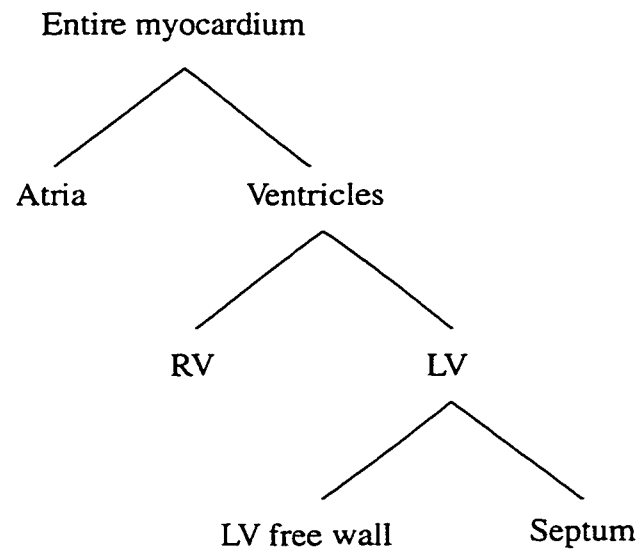


FIGURE 1.5. The myocardial regions investigated, in which the  $VG_{80}s$  were correlated to  $DFT_{50}s$ .

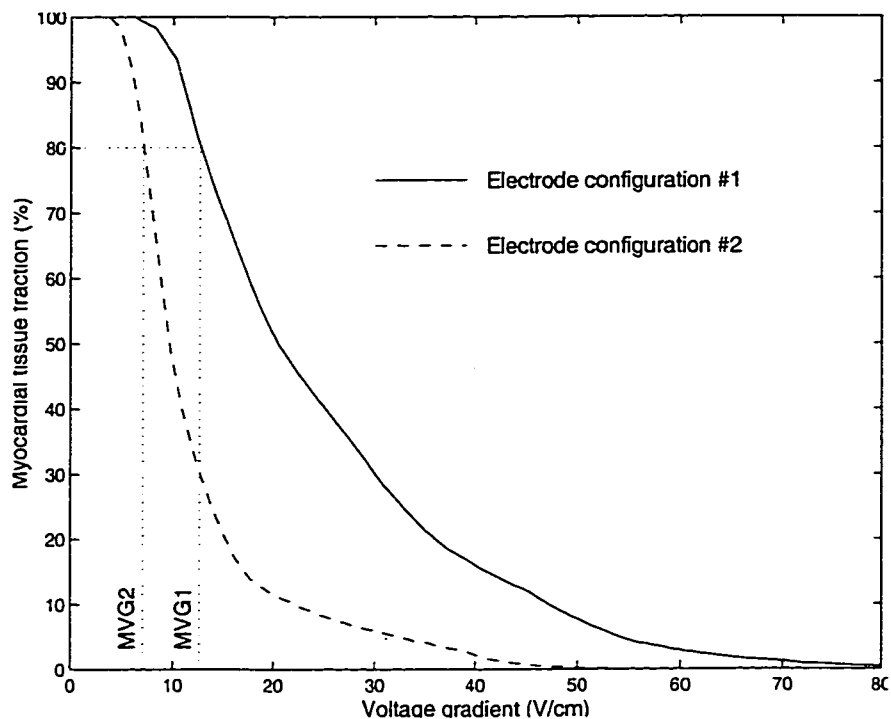


FIGURE 1.6. Backward-cumulative voltage gradient histograms for two electrode configurations in a myocardial region from one animal model with the applied voltage of 400 V.  $VG_{80}$  is found by  $H(VG_{80}) = 80\%$ . Because the histogram for configuration 1 is to the right of the histogram for configuration 2,  $VG_{80}$  for configuration 1  $>$   $VG_{80}$  for configuration 2. We thus predict that the DFT for configuration 1 is less than that for configuration 2.

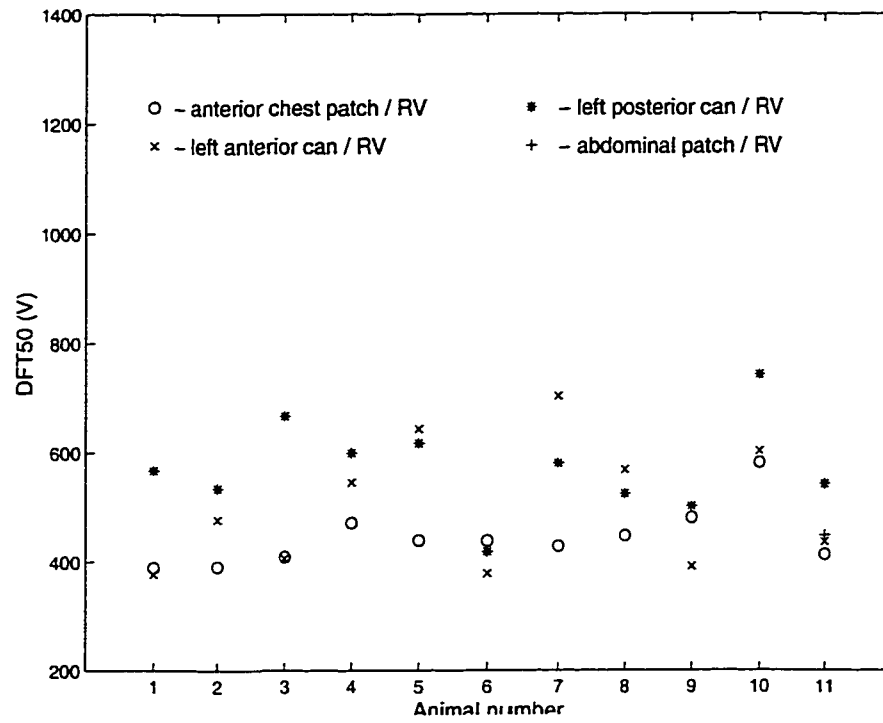


FIGURE 1.7. Experimental DFT<sub>50</sub> measurements.

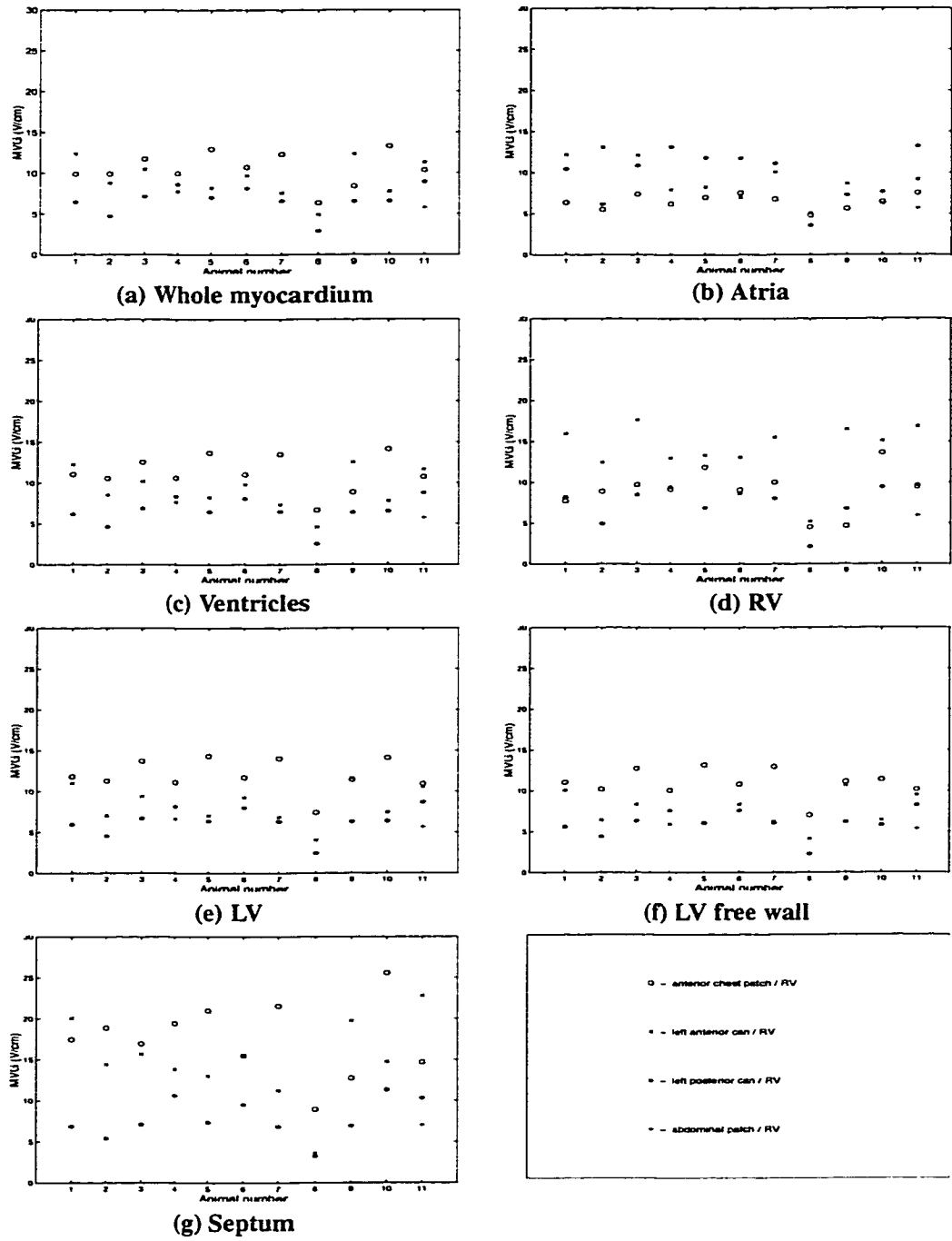


FIGURE 1.8.  $V_{G80s}$  for several different myocardial regions, with a fixed defibrillation voltage of 400 V.

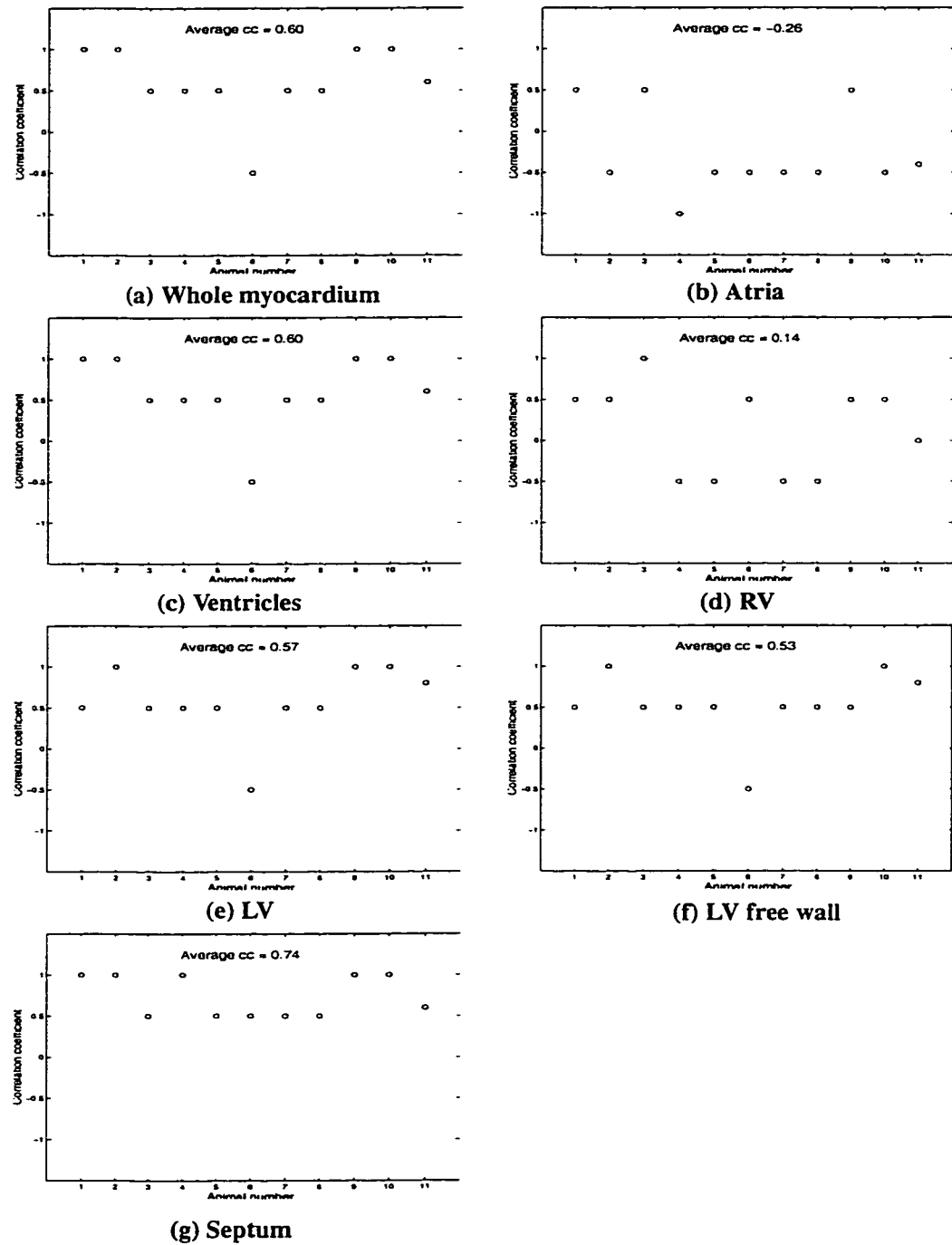


FIGURE 1.9. Within-animal correlation coefficients between  $DFT_{50}$  and  $VG_{80}$  in the myocardial regions.

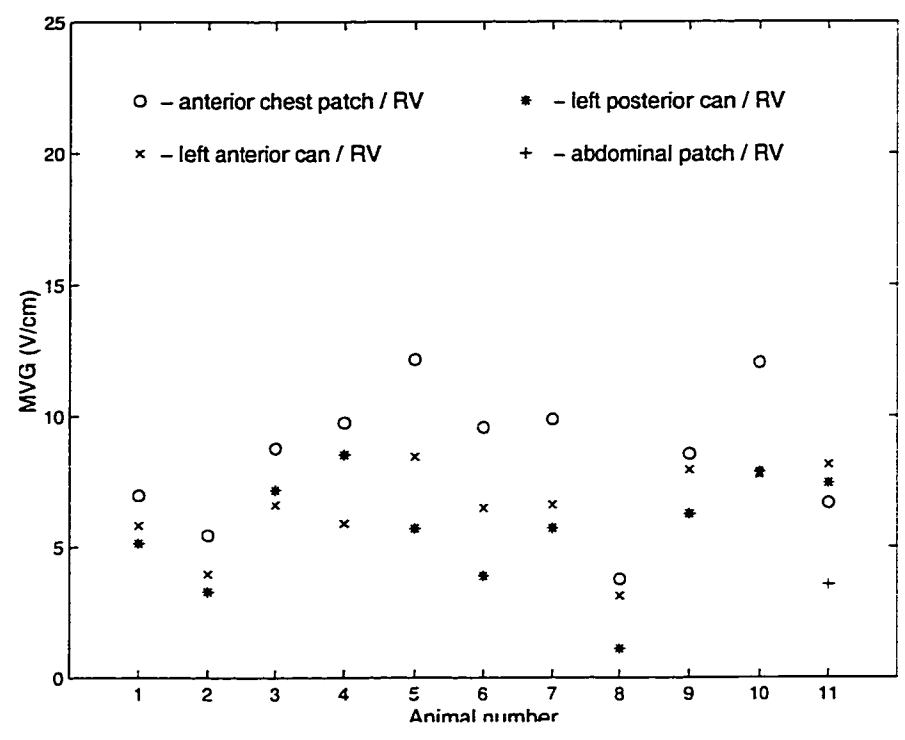


FIGURE 1.10. Minimal VGs in the entire myocardium when  $DFT_{80}$ s are applied to the corresponding FE models.

## **Chapter 2. An Investigation of the Effects of Myocardial Anisotropy on the Heart Models: Methodology and Application in the Analysis of Defibrillation Efficacy**

### **I. Introduction**

The correlation between the DFT and myocardial VG estimated in Chapter 1 was based on isotropic myocardial models, while in fact myocardium has been shown to have significant anisotropy [59]. Myocardial anisotropy information is also needed in the study of many other bioelectric problems, such as the effects of electrode size and location on ventricular defibrillation effectiveness [37], and the propagation of electrocardiographic and magnetocardiographic signals in the heart [48]. These applications need to deal with electric or magnetic potentials and potential gradients in the heart. The isotropic-model simplification is commonly due to the fact that most FE models are constructed from anatomical atlases, or more recently, tomographic (CT or MRI) images of the subjects of interest. None of these anatomies provide information on myocardial fiber structure.

Unlike skeletal muscle, whose fiber orientation usually follows the principal axes of its overall 3D shape, myocardial fiber orientation has been demonstrated to have a complex structure [54][84][85]. For example, the fiber in the LV free wall changes direction by more than  $90^\circ$  from endocardium to epicardium [85]. The fiber direction also changes significantly from the ventricular base to the apex. In an anisotropic material with 2 fixed principal axes such as a skeletal muscle, increasing the anisotropy ratio from 1 to 2 would increase the ratio of longitudinal to transverse voltages by 41% [68]. However, it is unknown, for the much more complex myocardial fiber structure, how much error is introduced in the computed voltage and VG by approximating the myocardium as an isotropic medium.

An example of the use of VG is in the study of ventricular defibrillation, in which estimation of the myocardial VG is needed to assess the efficacy of an electrode configuration [87]. While the ICD provides a better defibrillation efficacy with less damage to other tissues than the transthoracic defibrillators [79][87], the technique can be potentially improved if the relation between the DFT and myocardial VG can be better quantified [71]. Experiments have shown that a certain minimal VG is needed for successful defibrillation [32]. Animal experiments and subject-specific FE models in Chapter 1 have shown that the defibrillation efficacy, measured as the  $DFT_{50}$ , is statistically correlated with the  $VG_{80}$  in the LV and septum, suggesting the potential for estimating the defibrillation efficacy by computing the myocardial VG distribution using subject-specific FE models [92]. However, the FE models used in this study assume an isotropic myocardium, and therefore the error involved by making this assumption needs to be estimated to validate the correlation between the  $DFT_{50}$  and myocardial  $VG_{80}$ .

To obtain the information on myocardial anisotropy, both the fiber structure and anisotropy ratio are needed. Numerous studies have been conducted to quantify fiber orientation with regard to heart geometry [85]. None of those measurements provide a global mapping of the fiber structure that is usable for FE modeling. Recently, Nielsen *et al.* conducted a systematic measurement of the myocardial fiber structure and obtained both the heart geometry and myocardial fiber directions from several hearts [54]. The data were made publicly available, providing a useful resource for other research involving the complex myocardial fiber structure.

In this study, we used Nielsen's data to investigate the effects of myocardial anisotropy by mapping the fiber direction onto individual hearts, using a method based on elastic deformation. We estimated the difference in myocardial  $VG_{80}$  between isotropic and anisotropic myocardium, and studied its effects on the correlation between the  $DFT_{50}$  and myocardial  $VG_{80}$ .

## II. Methods

### A. Model construction

The animal model was chosen from one of the models described in Chapter 1. See Chapter 1, Sections II.A and II.B for details on the experiment protocol and model construction. The animal subject chosen for this study was a Hampshire-Yorkshire Cross pig, weighing 25 kg. A clinically useful nonsternotomy defibrillation electrode configuration was examined. The anode was a subcutaneous chest patch electrode (Medtronic, Minneapolis, MN, model 6895) placed over the cardiac apex of the LV. The cathode was a flexible catheter coil-electrode (Medtronic model 6884) fluoroscopically placed in the apex of the RV through the right jugular vein, with its tip anchored in the apical myocardium (Figure 2.1).

The thorax model was constructed from the segmented CT images of the animal. The segmented images, when stacked together, form a 3D thorax model of the pig, based on which the FE analyses were performed. The 3D thorax model can be visualized in the AVS visual programming environment (Advanced Visual Systems Inc, Waltham, MA) [2].

### B. FE method

For a description of our adaptive FE solver, see Chapter 1, Section II.B. Since the pixel size is 0.59 mm while the distance between images is 3 mm, each element in the FE models had an aspect ratio of 1:1:5.12, which might affect the convergence of the FE solutions. The images were thus downsampled from 512x512 to 256x256, making the new element size of 1.2x1.2x3.0 mm, for a final aspect ratio of 1:1:2.56. The algorithm was run on a Pentium-233 PC (233 MHz, Linux OS) containing 256 Mbytes of main memory.

Our adaptive FE algorithm was originally designed for isotropic models, i.e.,  $\sigma$  in Eq. (1.2) was a scalar [70]. To study the effects of myocardial anisotropy, the algorithm was modified to extend  $\sigma$  to a tissue conductivity tensor using the myocardial fiber direction obtained via elastic matching (see Sections C-E). Let the principal axes of the fiber be

$(L, T_1, T_2)$ , with  $L$  being the unit longitudinal and  $T_1$  and  $T_2$  being the two unit transverse vectors, and let the principal conductivities and resistivities be  $\sigma_L, \sigma_T$  and  $\rho_L, \rho_T$ , respectively ( $\sigma_L = \rho_L^{-1}, \sigma_T = \rho_T^{-1}, \sigma_L \geq \sigma_T$ ). Assuming an arbitrary orientation of  $(L, T_1, T_2)$  with regard to the  $(x, y, z)$  coordinate system, Eq. (1.2) can be expressed in matrix notation:

$$\begin{bmatrix} \frac{\partial}{\partial x} & \frac{\partial}{\partial y} & \frac{\partial}{\partial z} \end{bmatrix} \underline{J}^t \begin{bmatrix} \sigma_L & 0 & 0 \\ 0 & \sigma_T & 0 \\ 0 & 0 & \sigma_T \end{bmatrix} \underline{J} \begin{bmatrix} \frac{\partial}{\partial x} \\ \frac{\partial}{\partial y} \\ \frac{\partial}{\partial z} \end{bmatrix} V = 0 \quad (2.1)$$

where  $\underline{J}$  and  $\underline{J}^t$  are an orthonormal matrix and its transpose, respectively, for the rotation between the coordinate systems  $(L, T_1, T_2)$  and  $(x, y, z)$ .  $\underline{J}$  can be obtained by projecting the  $(L, T_1, T_2)$  axes onto the  $(x, y, z)$  coordinates:

$$\underline{J} = \begin{bmatrix} L_x & L_y & L_z \\ T_{1x} & T_{1y} & T_{1z} \\ T_{2x} & T_{2y} & T_{2z} \end{bmatrix} \quad (2.2)$$

Comparing Eqs. (1.2) and (2.1), it is easy to see that the conductivity tensor is:

$$\underline{\sigma} = \underline{J}^t \begin{bmatrix} \sigma_L & 0 & 0 \\ 0 & \sigma_T & 0 \\ 0 & 0 & \sigma_T \end{bmatrix} \underline{J} \quad (2.3)$$

which is a symmetric 3x3 matrix. Thus, the conductivity tensor can be easily calculated given the principal conductivities or principal resistivities of the myocardium and the fiber

direction. The evaluation of the stiffness matrices of the FE equations was adjusted accordingly.

When observing the effects of myocardial anisotropy, it is important to note that not only the anisotropy ratio but also the absolute resistivity values of the myocardium affect the myocardial VG. To compare the isotropic and anisotropic myocardial models, we focus only on the effect of non-unity anisotropy ratio and need to fix some quantity of the absolute resistivity values. The principal myocardial resistivities ( $\rho_L$  and  $\rho_T$ ) were chosen with a constant geometric mean, i.e.,  $\rho_L \cdot \rho_T = \text{constant}$ , but a varying anisotropy ratio  $\rho_T/\rho_L$ . As we will see from Eqs. (3.2) and (3.3) in Chapter 3, when current flow is perpendicular to the fibers in a homogeneous anisotropic tissue, the transverse voltage drop  $V_T \propto \sqrt{\rho_L \cdot \rho_T}$  and thus does not change. Although the thorax model is highly inhomogeneous, fixing  $\rho_L \cdot \rho_T$  still provides a base for observation of the effects of anisotropy ratio. The mean myocardial resistivity was the generic value adopted from publications (Table 2.1, [25]), while the anisotropy ratio was varied from 1 to 20 (Table 2.2, [59]). For the rest of the tissues, generic isotropic resistivities from [25][72] were used, as shown in Table 2.1.

### ***C. Myocardial fiber orientation***

The calculation of anisotropic conductivity tensors for myocardium requires knowing the local myocardial fiber direction (Eqs. (2.2) and (2.3)), information not available from the CT scans.

One way to obtain the myocardial fiber direction is through anatomical measurement. The invaluable work by Torrent-Guasp, Hort, and Streeter has pioneered the investigation of myocardial fiber structure [84][85]. Torrent-Guasp studied the spiral course of fibers from epicardium to endocardium by lifting up layers of myocardium and tracing the pathways of the fibers in a cow heart. Hort performed a microscopic analysis of frozen

sections from the hearts of guinea pigs, dogs, and pigs under systole and diastole, and studied the change of fiber direction across ventricular wall. Streeter *et al.* analyzed the fiber direction change across ventricular wall in cold-hardened sections of the hearts of pigs, dogs, monkeys [84], and human [85], and also attempted to explore the fiber structures mathematically [85]. Nielsen *et al.* [54] experimentally measured the ventricular fiber direction in excised canine hearts filled with silicone rubber and mounted on a measurement fixture. A special technique was developed to peel off the muscle in thin layers (0.5 mm) over the myocardial surface so that the entire ventricle could be evenly sampled. The results of these studies are in good agreement with each other. The contribution of the work by Nielsen *et al.* lies in the mapping of heart geometry in addition to the global mapping of fiber directions. Their data are available through the World Wide Web (<http://www.esc.auckland.ac.nz/Groups/Bioengineering/>).

The results about ventricular fiber structure can be summarized as follows [54][84][85]. (a) Most fibers are parallel to the epicardial surface, (b) epicardial myocardial fibers follow a left-handed helical pathway when viewed from the base, but endocardial fibers form a right-handed helix, (c) the fiber angle change across the myocardial wall is largest in the interventricular septum ( $60^\circ - 180^\circ$ ), modest in the LV free wall (more than  $90^\circ$ ), and least in the RV free wall (as low as  $20^\circ$ ). A typical section of the LV free wall has fibers in the mid-wall plane almost parallel to the ventricular base, while the bulk of fibers are oblique with regard to the base.

Fiber orientations measured experimentally in various mammalian species, including guinea pigs, cows, dogs, pigs, monkeys, and human, have demonstrated consistent and remarkable similarity within and across the species [85]. This similarity justifies our approach to map the fiber orientation data from a canine heart onto a pig heart in this study.

Two types of data available from Nielsen *et al.* [54] are related to our study: ventricular geometry and ventricular fiber directions in directional cosine. Our approach to mapping ventricular fiber angle data onto our pig's heart consists of two steps: (a) estab-

lish an elastic mapping function between the geometries of the two hearts, (b) use the one-to-one mapping to estimate fiber direction at each point in the pig’s heart. Because fiber directions in [54] were measured at discrete positions, interpolation was used.

#### ***D. Elastic mapping and fiber data interpolation***

Elastic mapping addresses the problem of differentiably deforming one object to another with certain energy constraints imposed on the deformed object [3][50]. Such energy constraints ensure that after mapping, an equilibrium state is reached between the external applied forces for deformation and the internal forces against deformation. Since elastic mapping deforms one object to another continuously, the two objects must have the same topological structure, while differing only in shape details. The external forces applied in the mapping are functions of a similarity measure often in the form of distance between the source and target objects, or more specifically in the form of an average displacement between some corresponding points in the two objects [50]. The internal forces, on the other hand, are based on the objects’ elasticity and the derivatives of some anatomical contours, which are essentially related to the stretching and bending energies. The equilibrium state can be solved by force-balancing or by minimizing total energy according to Lagrange’s principle.

An alternative in solving the equilibrium state is to use splines, which greatly eases computation. While the external force is represented by the correspondence of pre-specified control points, the internal force is implied in the splines. Unlike  $C^1$ -continuous Bzier splines, radial-basis splines are defined over the entire problem domain, suitable for modeling unstructured data sampled at arbitrary locations. The random nature of the anatomical landmarks in the mapping problem here makes radial-basis splines a better choice than B splines. Thin-plate splines [12] and multiquadric splines [52][53] are two useful radial-basis splines. Although thin-plate splines, which uniquely minimize the physical bending energy consistent with given constraints of point correspondence, have very similar performance as the multiquadric splines in 2D [23], the 3D thin-plate spline is

nondifferentiable at the control points [12], while the 3D multiquadric spline is differentiable everywhere. In this study, we used multiquadric splines.

The multiquadric spline has the following nonlinear form in 3D:

$$F(d_i) = \sqrt{d_i^2 + R^2} \quad (2.4)$$

where  $d_i = \|\mathbf{p} - \mathbf{p}_i\| = \sqrt{(x - x_i)^2 + (y - y_i)^2 + (z - z_i)^2}$ ,  $\mathbf{p} = (x, y, z)$  is an arbitrary point,  $\mathbf{p}_i = (x_i, y_i, z_i)$  is the  $i$ th control point, and  $R > 0$  is a parameter that determines the visual smoothness of the warping result. Assume that the coordinate systems in the source and target hearts are  $(x, y, z)$  and  $(X, Y, Z)$ , respectively. Splines were applied to the  $X$ ,  $Y$ , and  $Z$  coordinates separately, yielding the following trivariate transformations:

$$f(x, y, z) = \sum_{i=1}^N a_i \cdot F(d_i) + b_0 + b_1 \cdot x + b_2 \cdot y + b_3 \cdot z = X, Y, \text{ or } Z \quad (2.5)$$

where  $N$  is the number of control points of correspondence in the source and target hearts,  $a_i$ 's are the spline coefficients, and  $b_0 - b_3$  are the linear transformation coefficients. All the coefficients can be uniquely solved for, given  $N$  pairs of corresponding control points in the two hearts. Because there are four more coefficients than control points in Eq. (2.5), the following equations are added [22]:

$$\sum_{i=1}^N a_i = 0, \quad \sum_{i=1}^N a_i \cdot x = 0, \quad \sum_{i=1}^N a_i \cdot y = 0, \quad \sum_{i=1}^N a_i \cdot z = 0 \quad (2.6)$$

The coefficients describing each coordinate transform can be solved for independently of the other coordinates.

To provide a more uniform distribution of  $d_i$  in Eqs. (2.4) and (2.5), an affine transformation was applied before the multiquadric-spline based mapping. Suppose the control points in the source and target hearts are  $ps_i$  and  $pt_i$ , respectively, a 3x3 transformation matrix  $A$  and a 3x1 shifting matrix  $D$  can be found by satisfying the following equation:

$$\mathbf{Min} \left( \sum_i \|(A \cdot ps_i + D) - pt_i\|^2 \right) \quad (2.7)$$

The ultimate goal of elastic mapping is to map the myocardial fiber orientation. After the mapping functions were obtained from solving Eqs. (2.5) and (2.6), the Jacobian matrix between the two coordinate systems was calculated to produce the myocardial fiber directions at each point in the target heart:

$$\begin{bmatrix} dX \\ dY \\ dZ \end{bmatrix} = \begin{bmatrix} \frac{\partial X}{\partial x} & \frac{\partial X}{\partial y} & \frac{\partial X}{\partial z} \\ \frac{\partial Y}{\partial x} & \frac{\partial Y}{\partial y} & \frac{\partial Y}{\partial z} \\ \frac{\partial Z}{\partial x} & \frac{\partial Z}{\partial y} & \frac{\partial Z}{\partial z} \end{bmatrix} \begin{bmatrix} dx \\ dy \\ dz \end{bmatrix} \quad (2.8)$$

Because the dog's fiber directions were measured at discrete locations, Eqs. (2.5) and (2.6) were also used to fit the fiber direction data, except that  $f(x, y, z)$  is now one of the three directional cosines of the fibers and  $(x, y, z)$  is the coordinate for the dog heart [54]. A C++ program was written to implement the above mapping and interpolation procedures (Eqs. (2.5) - (2.8)).

### ***E. Anatomical landmarks***

The control points in the source and target hearts are best realized by anatomical landmarks. Landmark points are set of discrete geometric points that correspond biologi-

cally across subjects. In essence, they encode the information needed to describe a geometric shape from a morphometric standpoint [13]. A proper choice of landmark points is necessary to obtain good mapping functions between the pig heart in our study and the dog heart used by Nielsen *et al.* [54].

A total of 81 landmark points were chosen, evenly distributed on the surfaces of epicardium (26), LV endocardium (28), and RV endocardium (27). Figure 2.2 schematically shows the positions of the landmark points chosen in both hearts. For the epicardium (Figure 2.2 (a)), in addition to the apex and the center of the ventricular base, eight landmark points were chosen at the base and each of the two cross-sections equally spaced between the base and the apex, representing anterior, posterior, left, and right extremities, and anterior left and right, and posterior left and right, respectively. For the LV endocardium (Figure 2.2 (b)), four landmarks were chosen at each of the basal and apical cross sections of the LV endocardium, and 5 cross sections equally spaced in between. In adjacent cross sections, the four landmarks were alternated between anterior, posterior, left, right and anterior left, anterior right, posterior left, posterior right. For the RV endocardium (Figure 2.2 (c) and (d)), equally-spaced landmarks were chosen at the basal, apical, and three middle cross sections, with the number of points at each section from base to apex being four, three, four, two, three for the RV endocardial free wall, and three, two, three, two, one for the RV endocardial septum.

The anatomical landmarks were determined visually on the 3D myocardial surfaces displayed in AVS. The pig's LV, RV, and septum were assigned different tissue indices during image classification, thus allowing the epicardium and LV, RV, and septal endocardium to be easily extracted and displayed with the *IsoSurface* module which is based on the marching-cubes principle [2]. For the dog heart, the myocardial geometry is depicted by the coordinates of unstructured sample points on the surfaces of the epicardium, LV endocardium, and RV endocardium [54]. An AVS module was written to triangulate the myocardial surfaces using the sample points, taking advantage of the fact that all the samples were taken in equal-spaced parallel planes, which allowed the tiling trian-

gles to fill the myocardial surfaces continuously and seamlessly. We did not use the triangulation module in AVS as it is based on the Delaunay triangulation principle and performs best on surfaces for convex volumes.

The pig and dog's 3D myocardial surfaces were displayed side-by-side in AVS. In addition to the interactive capability that allows 3D shift, rotation, and scaling easily controllable by keyboard and mouse, AVS also provides utilities to allow the mouse cursor to be placed on a 3D surface by pointing and clicking, returning the 3D coordinate of the marked point on the surface. As a result, the anatomical landmarks were easily selected on both the pig and dog hearts. These landmarks were then used to derive the geometric mapping functions between the two hearts.

### III. Results

#### A. *Myocardial fiber orientation*

Figure 2.3 shows a screen-capture of the mapping procedure performed between the dog and the pig's hearts. The lower part of the screen shows the AVS network of modules used for visualization and manipulation of the 3D heart models. The upper part of the screen shows two windows, with the pig's heart on the left and the dog's heart on the right. The outmost white surface represents the reconstructed epicardium, the yellow surface is the LV endocardium, the green surface is the RV septum, and the blue surface is the RV free wall. The white spheres on the RV free wall are some of the landmarks identified in the mapping procedure. The transparency of each surface can be set individually (in Figure 2.3, the epicardium is semi-transparent while the other surfaces are opaque), allowing the relations between the surfaces to be seen clearly. The 3D heart models can be scaled, shifted, and rotated interactively, while a probe can be point-and-clicked to any landmark on a surface with the coordinates shown in the top of the windows. This interface greatly facilitates the identification of corresponding landmarks on the two models.

The optimal choice of the parameter  $R$  in Eq. (2.4) has been shown to be problem dependent [22]. Although Carlson and Foley have proposed a method to estimate the optimal  $R$  for a given data set, exact computation of this optimal value remains an unsolved problem [18]. An alternative approach is to observe the visual effects of  $R$  on the results [22], which was used in this study. By varying  $R$  between 0 and 10, our visual observation of the mapped 3D surface and fiber directions gave a best choice of  $R = 1\text{mm}$  for geometric mapping and  $R = 0.1\text{mm}$  for fiber interpolation.

Figure 2.4 shows the epicardial and endocardial surfaces of the dog heart together with the pig heart mapped into the dog's coordinate space at 5 levels from the ventricular base to the apex.

Figure 2.5 (a) and (b) show the anterior view of the mapped fiber direction on the epicardium and LV endocardium, respectively. A widely-employed method to represent the myocardial fiber direction quantitatively is to use the helix angle, the angle between a fiber and the ventricular base [85]. Figure 2.6 (a) and (b) show the fiber helix angle change vs. a uniform wall thickness across the middle septum and the lateral LV free wall, respectively, in the pig model.

To better depict the myocardial fiber direction change in the pig's ventricles, we defined an index to characterize the rate of fiber direction change at any given position  $(x, y, z)$  as follows:

$$\alpha_{x,y,z} = \mathbf{Max} \frac{\angle(\phi_{x+i,y+j,z+k}, \phi_{x,y,z})}{\sqrt{i^2 + j^2 + k^2}} (\text{o/mm}),$$

$$\forall i, j, k = 0, 1, i^2 + j^2 + k^2 \neq 0 \quad (2.9)$$

where  $\phi_{x,y,z}$  is the fiber direction vector at voxel  $(x, y, z)$ , and  $(i, j, k)$  are the local coordinates in the  $2 \times 2 \times 2$  neighborhood with the origin at  $(x, y, z)$ . Figure 2.7 demonstrates the complex pattern in the ventricular fiber direction change, with the septum and the apex

having the highest fiber direction change rate and the LV free wall having the most uniform fiber direction change. In general, the closer to the apex, the more drastically the fiber direction changes.

### ***B. Myocardial voltage gradients***

Although cardiac anisotropy has been measured in numerous studies, the measured anisotropy ratios vary according to whether monodomain or bidomain modeling of cardiac tissue is used. The ratios range from 1.5 [81] to 3.2 [65] under the monodomain assumption, and 9.0 (intracellular) and 2.6 (extracellular) [19] under the bidomain assumption. Our study used a monodomain FE model, but we examined a wide range of anisotropy ratio from 1 to 20 (Table 2.3).

To analyze the effects of myocardial anisotropy, we calculated the ratio of change in VG magnitude from the isotropic case to a highly anisotropic case (anisotropy ratio = 20) (Figure 2.8). The maximum change (more than 2.5 fold) occurs in the LV free wall, while change in the septum and most of the RV is much more moderate. Comparing Figure 2.8 with Figure 2.7, the VG magnitude change does not appear to correlate with the change of myocardial fiber direction: the maximum VG magnitude change coincides with neither the maximum nor minimum fiber direction change.

For the study of ventricular defibrillation, the inverse cumulative VG histograms provide important information on the estimation of defibrillation efficacy [92]. Chapter 1 has shown that  $VG_{80}$ , the 80th percentile of VG in the ventricular mass, has a statistically significant correlation with the  $DFT_{50}$ . Figure 2.9 - Figure 2.13 show the inverse cumulative VG histograms for the LV free wall, septum, whole LV, RV free wall, and whole ventricular mass, respectively. The changes in  $VG_{80}$  due to tissue property change from isotropy to anisotropy are also listed in Table 2.3. The change in  $VG_{80}$  from isotropy to an anisotropy ratio of 2 is high in the LV free wall (8.6%) and RV free wall (9.6%) but small in the septum (0.1%). Because the LV mass consists of the LV free wall and septum, the change in LV's  $VG_{80}$  is intermediate (8.2%). Since LV accounts for most of the ventricular

mass, change in the ventricular  $VG_{80}$  is also 8.2%. In general,  $VG_{80}$  increases from its isotropic value as the anisotropy ratio increases.

## IV. Discussion

### A. Mapped heart geometry and fiber direction

Although eighty-one landmarks were used in mapping, in principle any sufficient number of landmarks can be chosen as long as they have an approximately uniform spatial density so that different parts of the heart have the same weight of influence on the mapping results. As discussed later, our results suggest that 81 landmarks provide adequate accuracy for the mapping procedure. While all the landmarks were chosen on the myocardial surfaces of epicardium and endocardium because these surfaces are most easily identifiable, landmarks within the myocardial wall could in principle be used to further increase the mapping accuracy. The choice of landmarks is limited by the confidence in visual determination of the heart anatomy [13] as viewed in AVS. In case of the dog model provided by Nielsen *et al.* [54], the papillary and trabecular muscles, for example, make the LV endocardium a very irregular surface, and the landmarks difficult to locate. Incomplete sampling in the dog's RV endocardium near apex also makes landmark correspondence difficult between the pig and dog. The authors did find a certain variability in identifying the landmarks due to the uncertainty in visual observation of the reconstructed 3D myocardial surfaces, but the variation turned out to be small enough that the resulting variations in the mapped pig's myocardial fiber directions were small.

Figure 2.4 demonstrates the quality of the geometric mapping between the pig and dog's myocardial surfaces. We calculated the average distance between the two surfaces, defined as an average of the distance between any point on the dog's myocardial surface to the closest point on the mapped pig's myocardial surface. The average distance is 2.3, 2.2, and 2.2 mm for epicardial, LV endocardial, and RV endocardial surfaces, respectively, comparable to the RMS errors of 0.9, 2.6, and 2.1 mm in the dog data due to their fitting of

the heart model to the experimentally measured geometry [54]. This small error indicates that the multiquadric-spline based mapping procedure achieves a good mapping accuracy.

A breakdown of the above average distance shows that the major error in mapping the epicardium occurs on the RV side (Figure 2.4 (a) - (d)). The pig's RV-side epicardium lies for the most part within the dog's epicardium. The pig's RV endocardium, on the other hand, often maps outside the dog's RV endocardium. This discrepancy reflects the fact that the pig's RV was fully stretched at the time of sacrifice due to the venous blood returning to the RV chamber, and thus the RV free wall was very thin. In contrast, the dog heart used in Nielsen's study [54] was cleared of blood before measurement, and the corresponding tissue distortion was not present. Because the elasticity ( $R$  in Eq. (2.4)) in mapping was uniform over the entire myocardium, better mapping of the RV free wall was difficult to obtain without a sacrifice in the mapping quality at other locations.

The warped pig's LV endocardium in general agrees well with the dog's endocardium in its location and area. The main difference is in smoothness, i.e., the pig's LV endocardium appears much smoother than the dog's LV endocardium. This is because the papillary and trabecular muscles are not easily seen on the pig's CT images and were thus ignored during classification. If these details were present, many more landmark points would be required.

An important parameter affecting the mapping outcome is  $R$ . We chose  $R = 1$  mm in Figure 2.4 to balance mapping accuracy in different parts of the myocardium. When  $R$  increases, the LV-side epicardium of the pig becomes smooth and is closer to that of the dog, but the RV-side smoothness is worsened. The opposite is true when  $R$  decreases. The choice of  $R = 1$  mm is therefore a compromise between the LV and RV portions of the myocardium.

The mapping of the myocardial fiber direction vectors, i.e., mapping of the derivatives of the coordinate transformation, can be examined by comparing the myocardial fiber patterns with published data at locations where characteristic fiber patterns are known to

exist. For example, an important characteristic of myocardial fiber orientation is its left-handed helical arrangement on the epicardium when the thumb is pointing from the apex to the base. The pig model's epicardial fiber direction in Figure 2.5 (a) changes smoothly in the correct orientation. On the LV endocardium, the fiber orientation is reversed to a right-handed helical pathway, and the LV fibers, excluding those at the apex, are at almost right angles to the corresponding epicardial fibers (Figure 2.5 (b)). The LV endocardial fiber orientation does not have as smooth a pattern as does the epicardial orientation, as demonstrated by Streeter [85]. Another distinctive feature is the transition of fiber direction across the middle septal wall and across the lateral LV free wall, shown as helix angle in Figure 2.6 (a) and (b) that changes monotonically across the wall. The helix angle change in the septum is greater than that in the LV free wall. The decrease in helix angle from the peak when the position gets very close to the LV endocardium in Figure 2.6 (a) is because as the fiber passes the vertical position relative to the ventricular base, the helix angle reaches its maximum of  $90^\circ$  and is then reduced. These results are all comparable to other reported fiber direction change in the septum and LV free wall [30][66][82][83][85].

It should be pointed out that we used a different value of  $R$  for the fitting of fiber fields from that used in the mapping of geometry. Because more than 2800 data points were used for the fiber field fitting, the results are not sensitive to the value of  $R$ . The choice of  $R = 0.1\text{mm}$  provided a satisfactory fiber field.

Although the elastic mapping procedure from a "generic" data set to a specific subject precludes the study of individual variation in myocardial fiber directions, mapping allows a quick estimation of the magnitude of the effects of myocardial anisotropy on FE models, in which an individual animal's fiber direction information is difficult to come by. Other potential application area of the technique may include quantitative comparison of the myocardial fiber pattern of different individuals and species with regard to their geometry.

## ***B. Myocardial voltage gradient***

Figure 2.8 shows the spatial distribution of the change in VG when the electric resistance of myocardium changes from isotropy to anisotropy of 20. Similar results are also seen for anisotropy of less than 20, with the change in VG magnitude correspondingly smaller. Overall, the VG magnitude tends to increase with the increase of anisotropy ratio over most of the ventricles. The change is most obvious in the LV free wall, where the VG magnitude can increase by up to three times for an anisotropy of 20.

Since the complex pattern of fiber orientation contributes to the VG change in the myocardium, it is logical to ask whether the VG magnitude change correlates with the fiber direction change in the ventricles. Comparison of Figure 2.7 and Figure 2.8 shows that in contrast to the VG change that is greatest in the LV free wall, the fiber direction of the myocardium, or the principal axes of the myocardial anisotropy, change with comparable rapidity throughout the entire ventricles. Significant correlation is not observed between the fiber direction change rate in Figure 2.7 and the VG magnitude change in Figure 2.8. That VG changes the most in the LV free wall is likely due to the large volume of the LV free wall in which there is more current than in any other myocardial portions.

Chapter 1 has shown that the  $VG_{80}$  in the LV free wall and septum is significantly correlated with the measured  $DFT_{50}$ , while the  $VG_{80}$  in the RV and atria does not show significant correlation. Since that study used an isotropic heart model and ignored the fiber orientation, the correlation between the  $VG_{80}$  and the  $DFT_{50}$  was reevaluated.

Figure 2.9 - Figure 2.13 show that the VG in most of the myocardium increases with an increase in tissue anisotropy except in the septum, where the VG tends to decrease at lower values. The  $VG_{80}$  changes by less than 10% for an anisotropy of 2, but by as high as 40% for an anisotropy of 20 (Table 2.3). A recent careful study performed by Steendijk *et al.* experimentally measured the myocardial anisotropy in dogs using the four-electrode technique and found an anisotropy ratio of less than 2 for a frequency range from 5k to 60 kHz [81]. Therefore it is likely that the increase in  $VG_{80}$  from an isotropic heart model to

a more realistic anisotropic model would be less than 10% (Table 2.3). In Chapter 1, the computed  $VG_{80}$ s between different electrode configurations have a more than 10% difference in 9 out of 11 pig models (82%) in the septum, in 8 out of 11 (73%) in the LV free wall, and in 7 out of 11 (64%) in the RV free wall. Considering that the myocardial VG changes in the same direction for any electrode configuration when tissues change from isotropic to anisotropic, the relative ranking of  $VG_{80}$  between different electrode configurations in Chapter 1 is likely to be affected even less. This suggests that the rank correlation results between the myocardial  $VG_{80}$  and  $DFT_{50}$  obtained in Chapter 1 will be affected little.

With the fiber information, the VG components along and perpendicular to myocardial fibers can also be extracted. Tung *et al.* [88] and Bardou *et al.* [6] have demonstrated that the cell stimulation thresholds depend on the cells' orientation with respect to the electric field and were lowest when the direction of the electric field intensity was aligned parallel to the long axis of the myocardial fibers, which is supported by *in vivo* animal experiments [5][34]. However, further experimental research is required to know how longitudinal and transverse VG components might be correlated with the DFT, which may help to further understand the relation between the myocardial VG and defibrillation efficacy.

Our approach has some limitations. First, the parameter  $R$  in Eq. (2.4) is uniform throughout the myocardium in the present elastic geometric mapping procedure, which is responsible for the irregularity of the RV endocardial surface seen in Figure 2.4. A possible remedy is to let  $R$  be locally adjustable based on  $d_i$  in Eq. (2.4) so that the pig's thin RV free wall could be stretched to the scale of the dog's RV free wall without much effect on the mapping accuracy of the LV free wall. We used the fiber orientation data provided by Nielsen *et al.* [54] during our mapping, so its accuracy is important to the validity of our procedure. Their experimental procedure was based on the assumption that the myocardial fibers are parallel to the epicardial surface so that their procedure of peeling off layers of myocardium in the measurement was justified. In fact, myocardial fibers imbricate

cate slowly from epicardium to endocardium by  $3 - 5^\circ$  [54][85], which may have contributed to the error in their data. Diffusion tensor MR imaging has shown promise in non-invasively measuring fiber orientations [64] and might provide more accurate depiction of the myocardial fiber field. The complexity of the myocardial fiber architecture also involves myocardial sheets that are ignored in this study but may also provide an invaluable information on the effects of myocardial anisotropy [46]. However, further investigations are needed to reveal how the sheet information can be utilized in an FE model. Finally, the unique fiber architecture of myocardium that differs from the skeletal muscle fiber structure makes a bidomain FE model more suitable for modeling its electric properties [59], which could potentially provide more accurate information on the relation between myocardial VG and DFT than the monodomain model.

## V. Conclusions

We have presented a methodology to incorporate a generic myocardial fiber orientation data into a model of an individual subject through elastic mapping based on the multiquadric spline. This elastic mapping procedure provides a viable approach to quickly assess the magnitude of the effects of the complex myocardial fiber structure and myocardial anisotropy. The underlying assumption of mapping is justified by the similarity of fiber orientation pattern among mammalian species. Although other methods can also be used for mapping, they often require sufficiently large number of landmarks to enforce correspondence between two models. With our approach, the number of landmarks can be drastically reduced by properly choosing the parameter  $R$  in the mapping procedure.

With the help of this mapping procedure, we have found that modeling the myocardium as an isotropic tissue as done previously would lead to an underestimation of the  $VG_{80}$  in the myocardium by less than 10% assuming that true myocardial anisotropy ratio is 2. The significance of this error will depend on the problem. In the study of the rank correlation between the myocardial VG and DFT for different electrode configurations, such an error is unlikely to greatly affect the correlation results.

TABLE 2.1. Tissue resistivities used in the FE models [25][72]

Tissues	Resistivity ( $\Omega\text{-cm}$ )
air	1000000
bone	16000
skin	1500
lung	1500
blood	154
muscle	700
fat	2180
myocardium <sup>1</sup>	420
liver	673
stomach	800
esophagus	700
spleen	420

Note: 1. Only isotropic resistivity of myocardium is listed. For anisotropic resistivities, see Table 2.2.

TABLE 2.2. Anisotropic myocardial resistivities

Anisotropy ratio	Longitudinal resistivity ( $\Omega\text{-cm}$ )	Transverse resistivity ( $\Omega\text{-cm}$ )
1	420	420
2	297	594
5	188	939
10	133	1328
20	94	1878

TABLE 2.3.  $V_{G80}$  from isotropy to anisotropy (absolute change (V/cm), (% change))

Tissue section	isotropy	anisotropy = 2	anisotropy = 5	anisotropy = 10	anisotropy = 20
LV free wall	3.22	3.50 (8.6%)	3.86 (19.8%)	4.10 (27.3%)	4.33 (34.5%)
septum	5.23	5.24 (0.1%)	4.96 (-5.2%)	4.70 (-10.2%)	4.59 (-12.2%)
LV	3.50	3.78 (8.2%)	4.11 (17.5%)	4.28 (22.3%)	4.41 (26.0%)
RV free wall	3.60	3.94 (9.6%)	4.47 (24.1%)	4.84 (34.6%)	5.02 (39.6%)
LV & RV	3.53	3.82 (8.2%)	4.18 (18.4%)	4.37 (23.9%)	4.56 (29.3%)

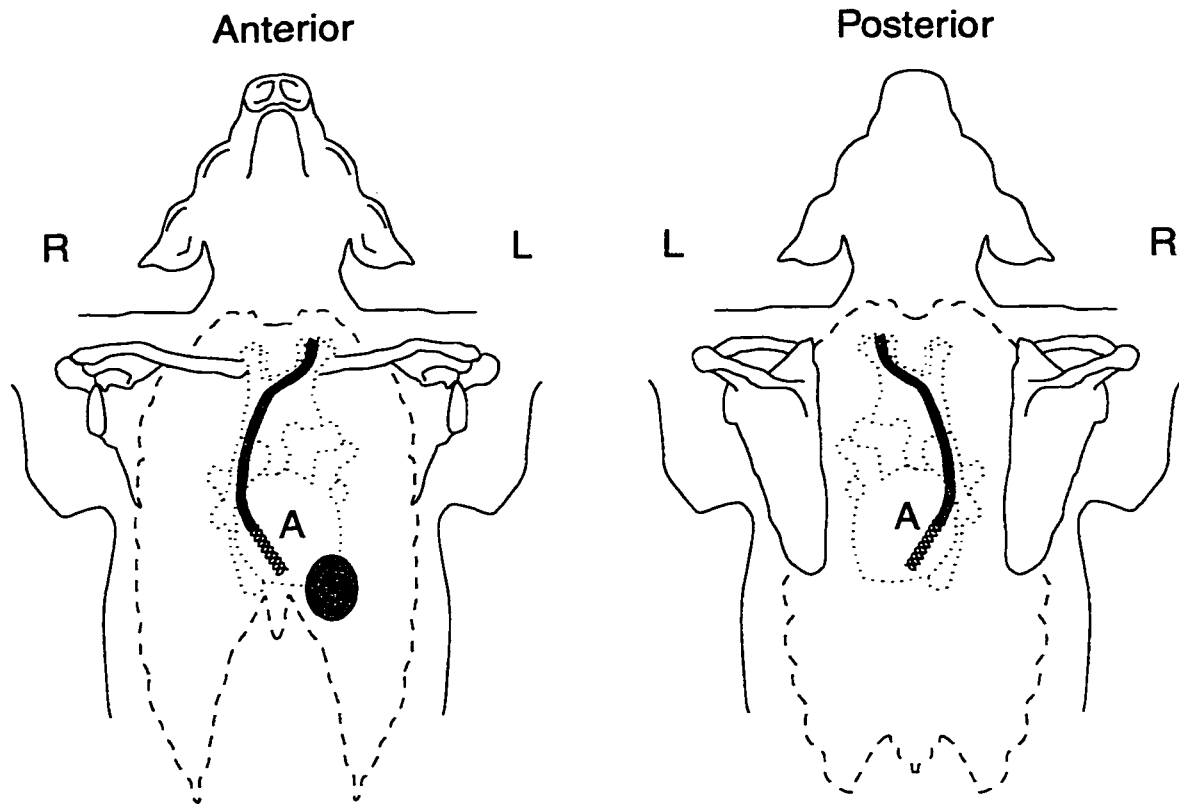


FIGURE 2.1. Defibrillation electrode configuration of left anterior chest patch / RV catheter electrode.

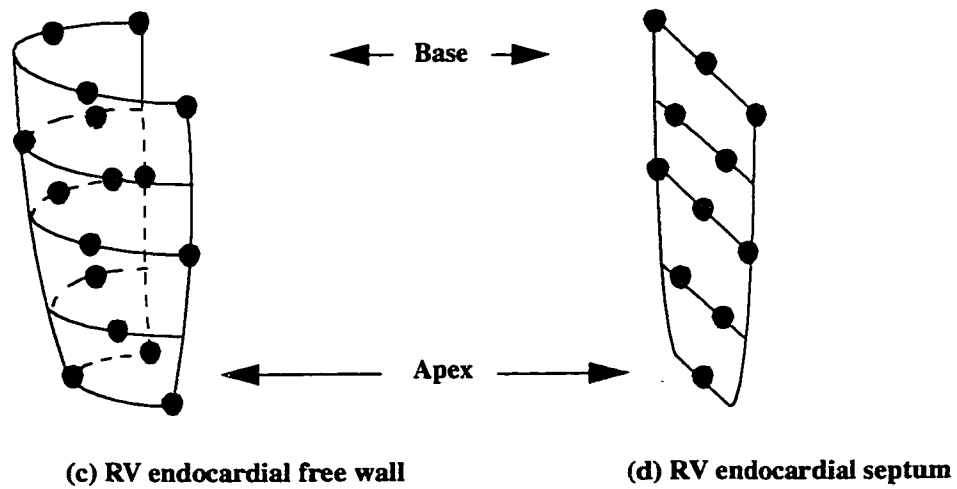
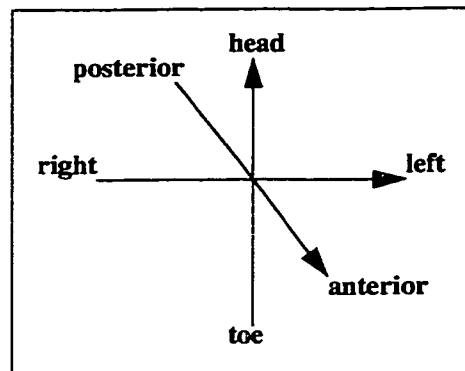
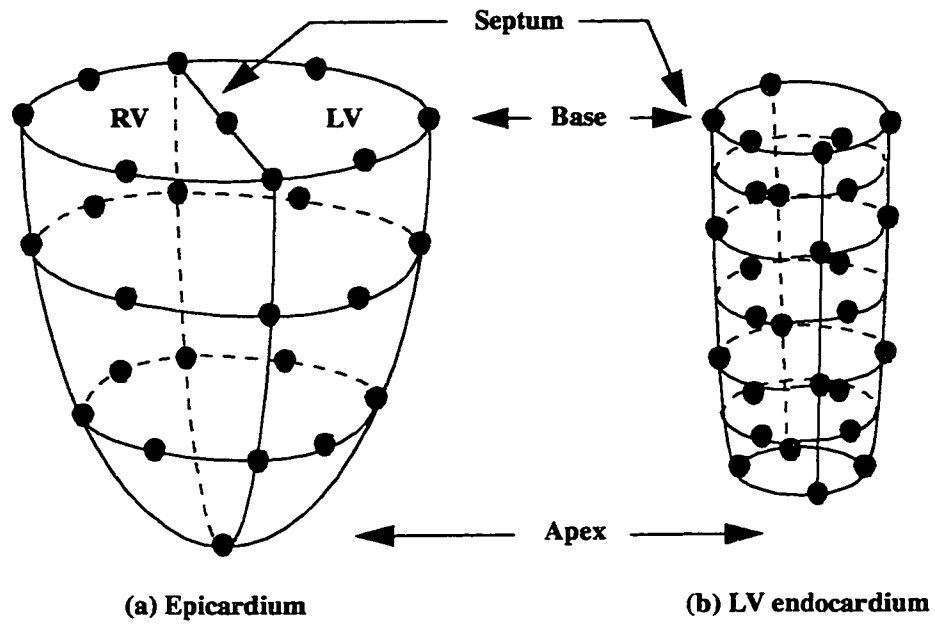


FIGURE 2.2. Landmark points chosen on the myocardial surfaces.

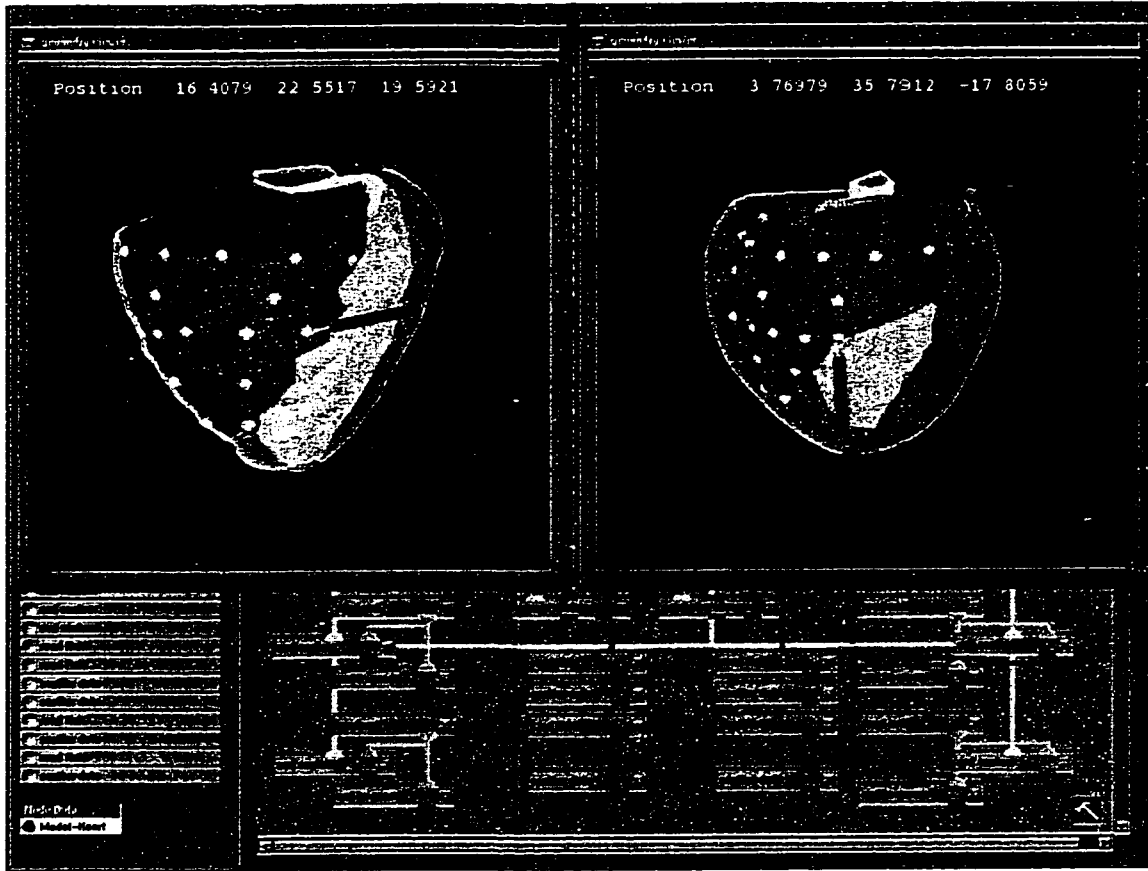


FIGURE 2.3. A screen capture of the myocardial fiber mapping procedure. The pig's heart is on the left, while the dog's heart is on the right.

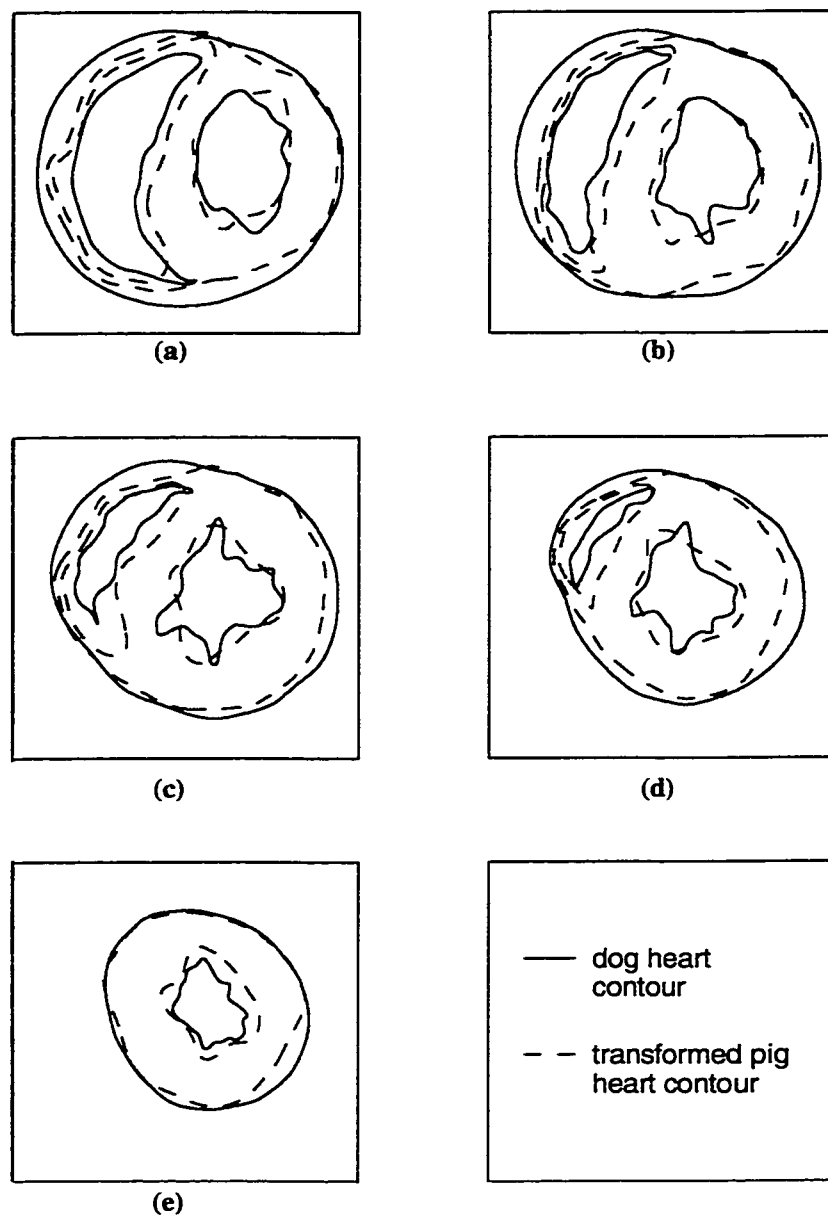


FIGURE 2.4. The dog's myocardial surfaces and the pig's myocardial surfaces mapped to the dog's coordinate space at cross-sections from base toward apex at  $X = -9.1, 0.9, 10.9, 20.9,$  and  $30.9$  mm, for (a) - (e), respectively, in the coordinate space of the dog [54].

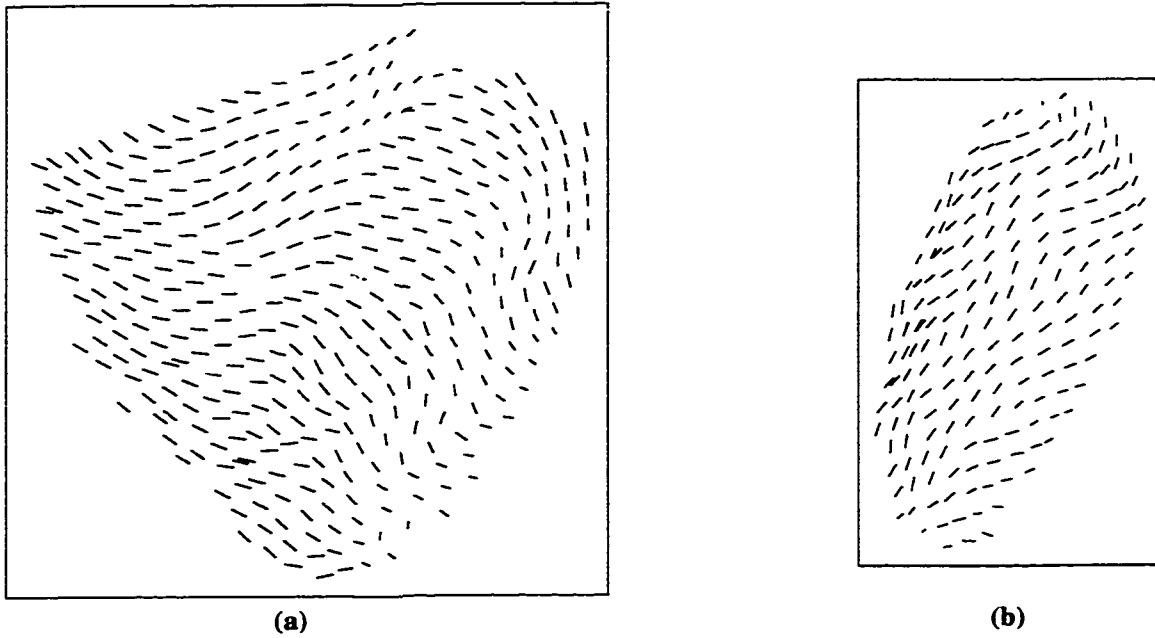


FIGURE 2.5. The mapped myocardial fiber direction in the fig. (a) an anterior view of the epicardial fiber directions, (b) an anterior view of the LV endocardial fiber directions.

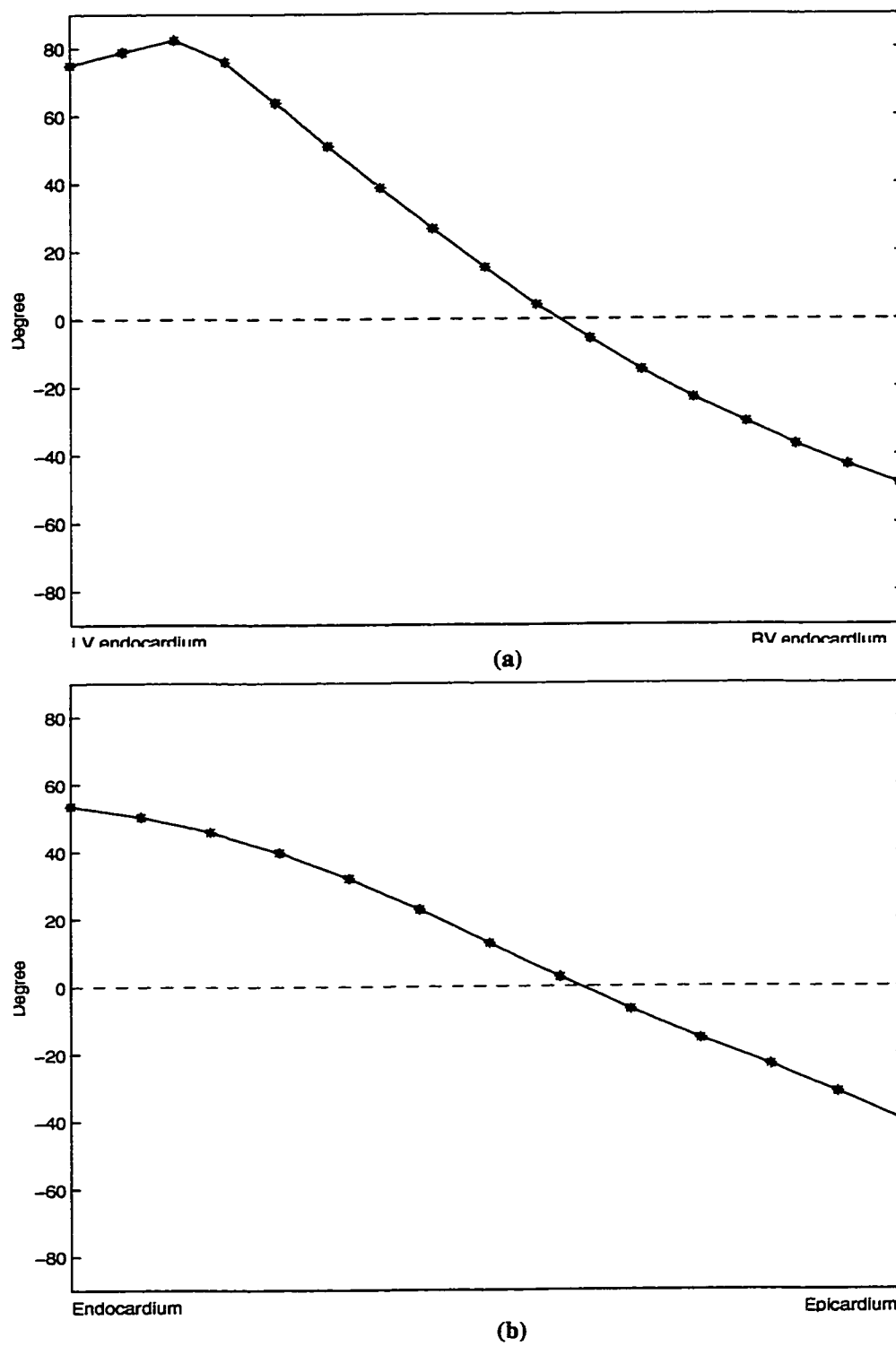


FIGURE 2.6. Cross-wall fiber directions in the pig's myocardium. (a) Across septum, (b) across lateral LV free wall.

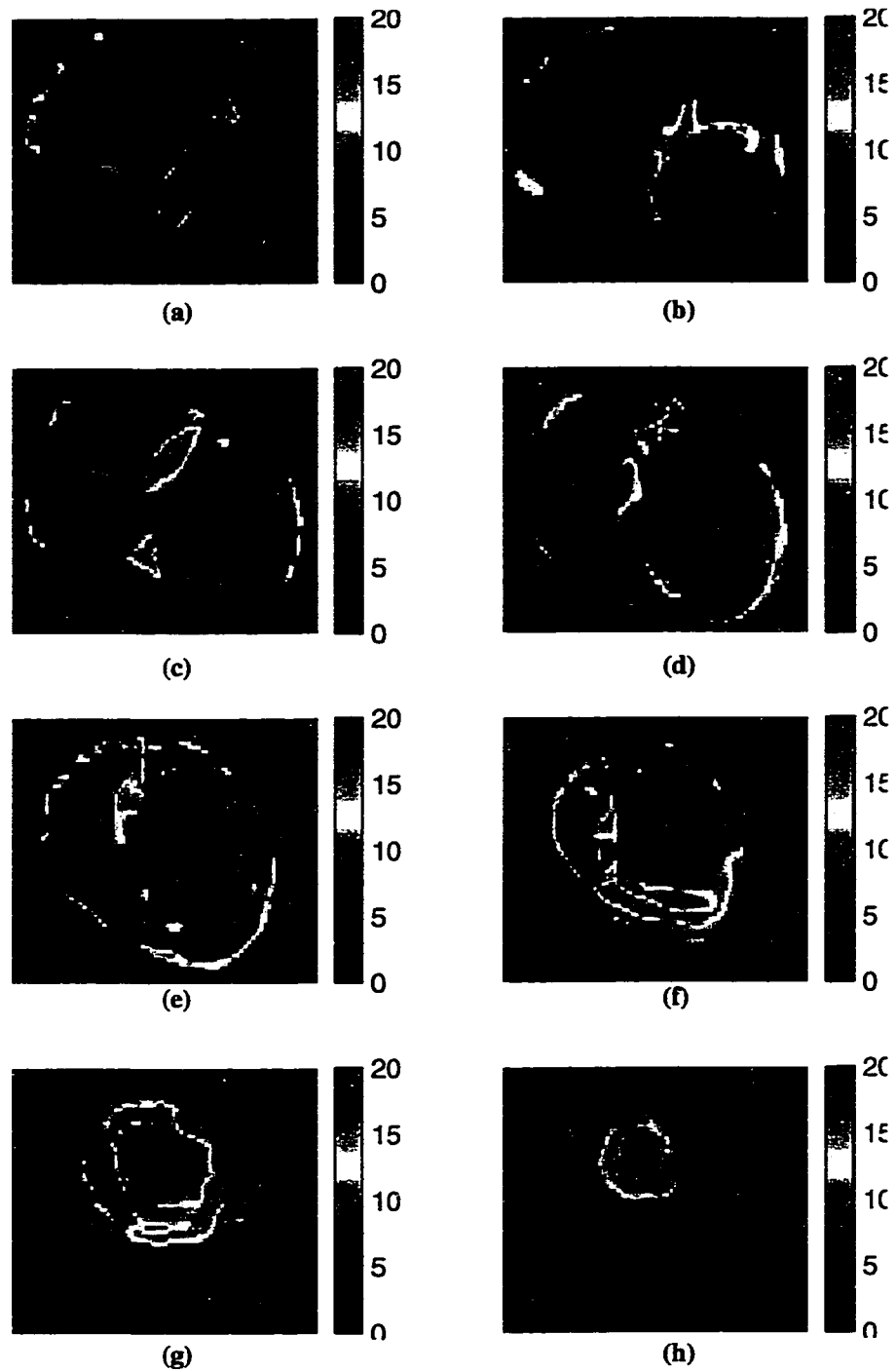


FIGURE 2.7. Rate of mapped fiber direction change in the pig's ventricles (unit:  $^{\circ}/\text{mm}$ ). (a) - (h) are slices 48, 39, 30, 21, 12, and 3mm, respectively, from the apex.

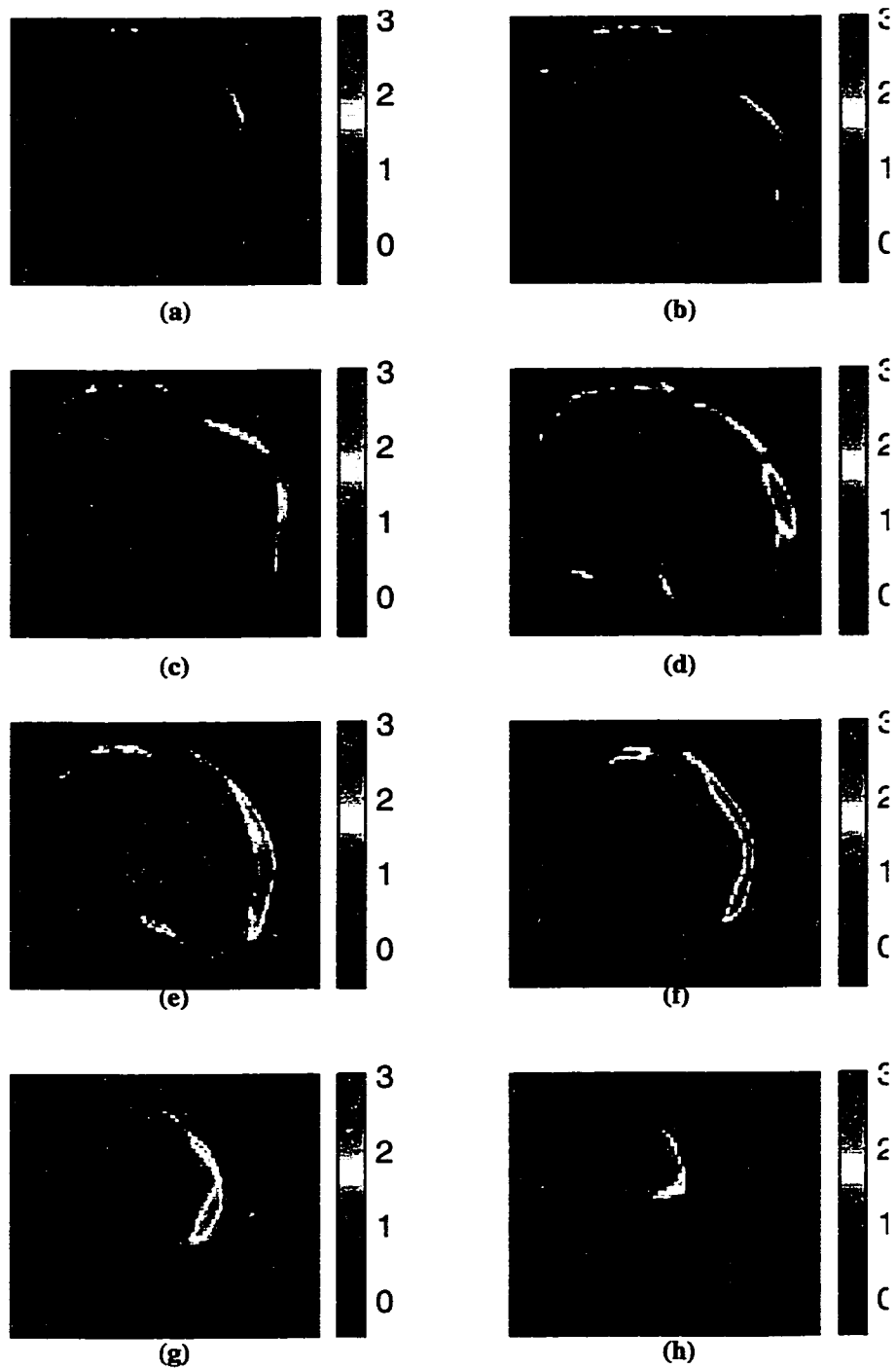


FIGURE 2.8. Ratio of VG with anisotropy ratio = 20 to VG with isotropy in the pig's ventricles. (a) - (h) are slices 48, 39, 30, 21, 12, and 3mm, respectively, from the apex.

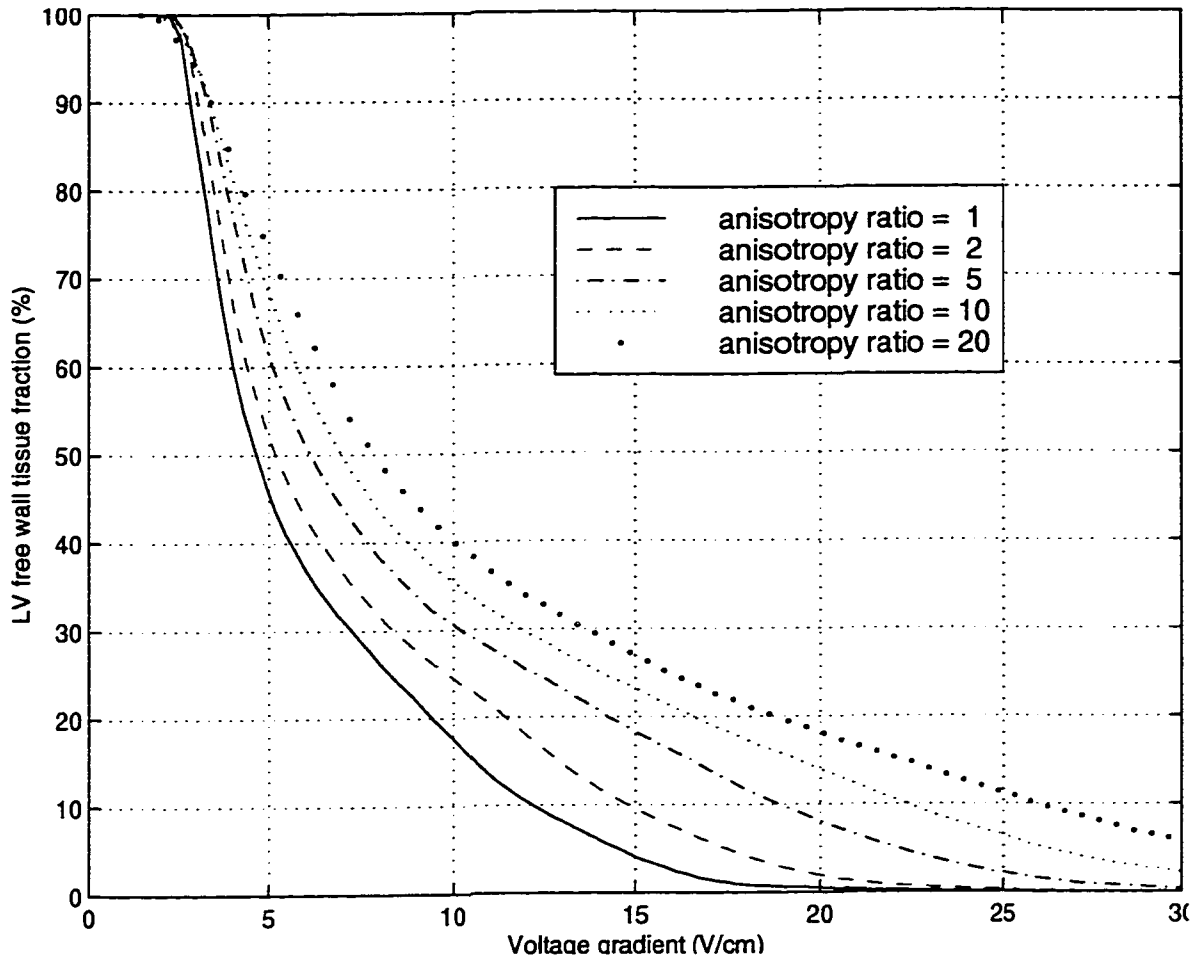


FIGURE 2.9. Inverse cumulative VG histograms in the pig's LV free wall.  $VG_{80}$  is found at the tissue fraction of 80%.

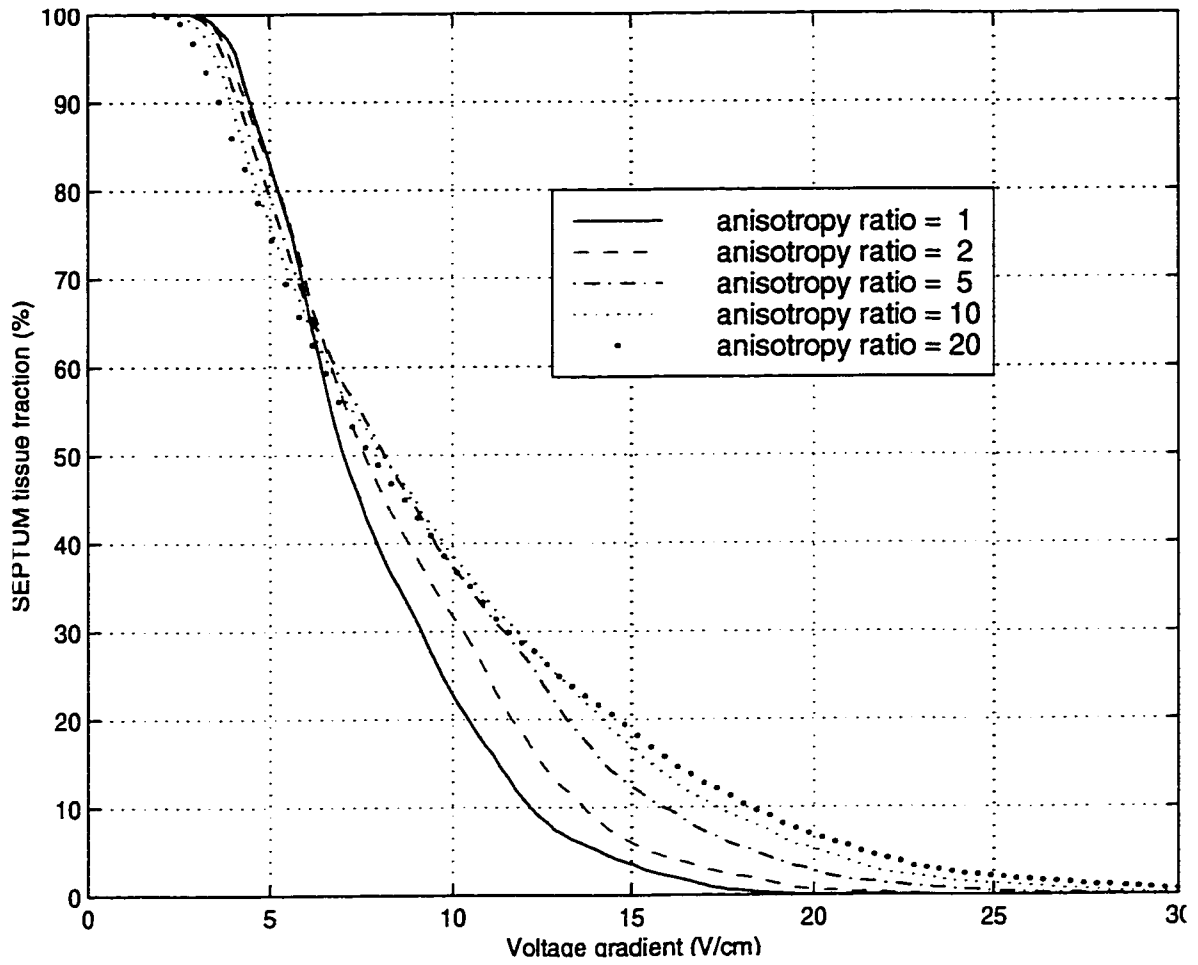


FIGURE 2.10. Inverse cumulative VG histograms in the pig's septum.  $VG_{80}$  is found at the tissue fraction of 80%.

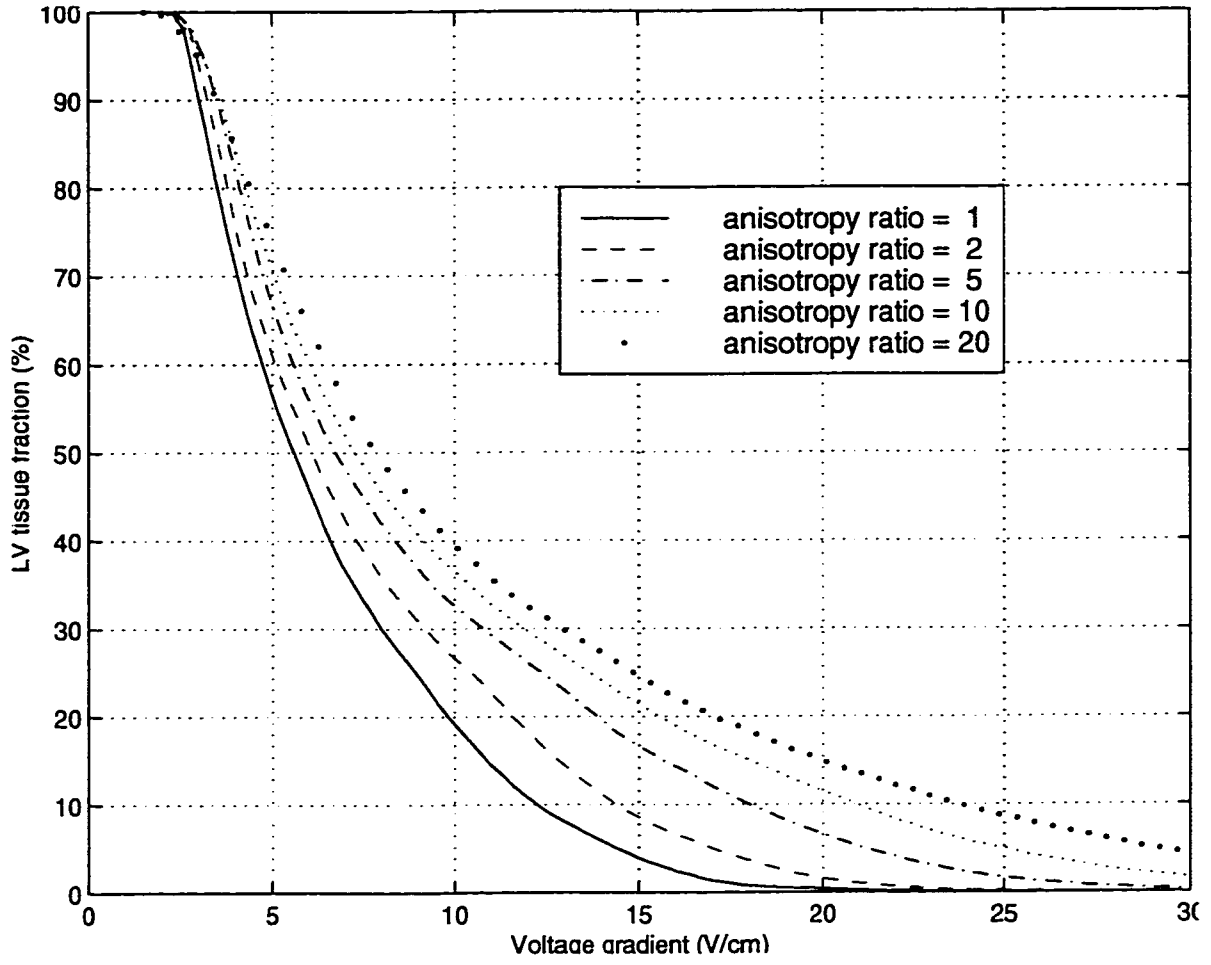


FIGURE 2.11. Inverse cumulative VG histograms in the pig's LV.  $VG_{80}$  is found at the tissue fraction of 80%.

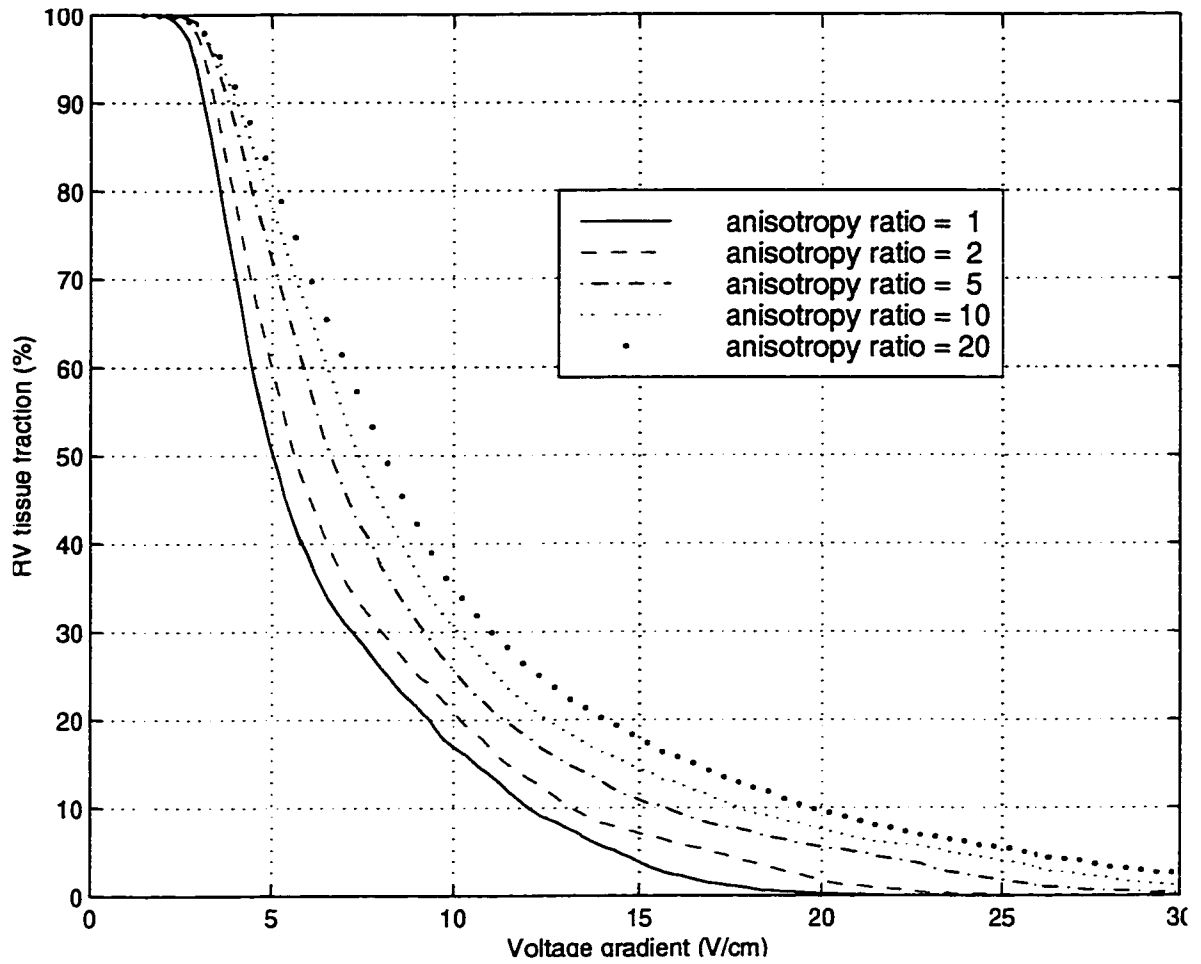


FIGURE 2.12. Inverse cumulative VG histograms in the pig's RV free wall.  $VG_{80}$  is found at the tissue fraction of 80%.

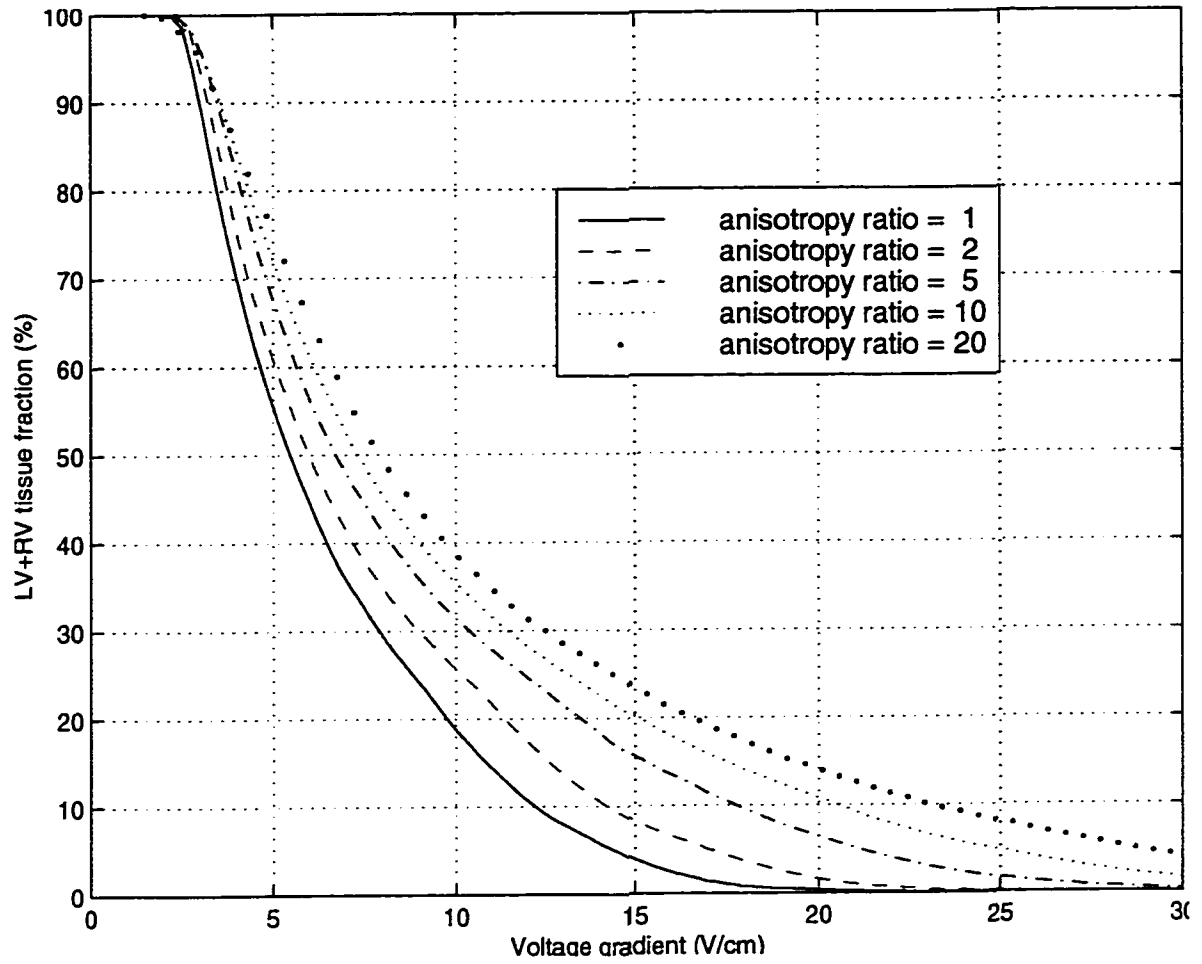


FIGURE 2.13. Inverse cumulative VG histograms in the pig's ventricles.  $VG_{80}$  is found at the tissue fraction of 80%.

## Chapter 3. The Geometric Effects on Resistivity Measurements with Four-electrode Probes in Isotropic and Anisotropic Tissues

### I. Introduction

Another factor that can significantly affect the estimated correlation between the DFT and myocardial VG is the principal myocardial resistivities, which are currently adopted from literature [25][72]. Myocardial VG has been shown to be affected most significantly by myocardial resistivities [35], thus inaccurate myocardial resistivities can alter the estimated correlation severely. In addition, resistivities are directly related to the computer modeling of many other bioelectric problems where volume conduction problems must be solved [48] and the measurement of many electrophysiological events [93]. Since literature has demonstrated a significant variation among the measured muscle resistivity values, it is vital to know what values can be used and why they can be used.

The probes used for measuring resistivities often consist of four equally-spaced electrodes placed on the surface of a tissue. The two outer electrodes are commonly used for current delivery and the two inner electrodes for voltage sensing. The sensing electrodes are connected to an amplifier with a very high input impedance to prevent input current flow, virtually eliminating polarization effects on the measurement.

The equations used to calculate the resistivities for the four-electrode measurement have been derived [68]. For an isotropic medium, the apparent tissue resistivity is calculated by

$$\rho_e = 2\pi \cdot IES \cdot \frac{V}{I} \quad (3.1)$$

where subscript  $e$  denotes the experimentally-measured or empirical value,  $IES$  is the interelectrode spacing,  $V$  is the measured voltage between the inner two electrodes, and  $I$

is the total current between the outer two electrodes. For an anisotropic medium, the empirical principal resistivities are ( $\rho_{Te} > \rho_{Le}$ )

$$\rho_{Te} = 2\pi \cdot IES \cdot \frac{V_L}{I} \quad (3.2)$$

$$\rho_{Le} = 2\pi \cdot IES \cdot \frac{V_T^2/V_L}{I} \quad (3.3)$$

where subscripts  $T$  (transverse) and  $L$  (longitudinal) denote the directions perpendicular and parallel to the low-resistivity direction, which, in the case of skeletal muscle, is the fiber direction. The empirical anisotropy ratio is

$$\alpha_e = \rho_{Te}/\rho_{Le} = \frac{V_L^2}{V_T^2} \quad (3.4)$$

Only in the ideal situation where all the electrodes are infinitesimally small (point electrodes) and the medium is semi-infinite [68], do  $\rho_e$ ,  $\rho_{Te}$ ,  $\rho_{Le}$ , and  $\alpha_e$  equal the true values  $\rho$ ,  $\rho_T$ ,  $\rho_L$ , and  $\alpha$ , respectively.

In contrast to the ideal situation, real tissue has a finite volume and real electrodes are typically cylinder-shaped with a finite electrode diameter (ED) and electrode length (EL), which causes the measurement results to deviate from the true values. Here ED and EL refer to the part of the electrodes inside the tissue, as shown in Figure 3.1. Schwan [73] suggested that the electrodes should be small enough to prevent them from disturbing the electric field. In previously-reported measurements [16][17][27][69][81], however, the geometry of the four-electrode probes and the volume of tissue samples were not fully described or justified. It is thus unclear to what degree the accuracy of these measurements were affected.

There exists a large variation among the published anisotropy ratios of skeletal muscle, ranging from 2.0 to 14.4 [16][17][21][27][69][99]. The four-electrode probe geometry generally varies among experiments, and its effects have not been studied thoroughly. The *in vivo* measurements on skeletal muscle by Gielen *et al.* [27] showed that electrode geometry can have a significant effect on the measured anisotropy ratio, which was 2.0 for an IES of 0.5 mm, but increased to 6.0 for an IES of 3 mm. The probe measuring the ratio of 2.0 had IES = 0.5 mm, ED = 0.1 mm, and possibly EL = 0.5 mm (unclear in [27]). Because IES is only 5 times ED and is possibly equal to EL, it is not clear whether such electrodes can be approximated as point electrodes meeting the ideal conditions for Eqs. (3.1) - (3.4). In this research, we systematically studied the effects of electrode geometry and tissue volume on four-electrode measurements, particularly with regard to anisotropic tissues.

Throughout the paper, we use the term *probe* for the four-electrode array and *electrode* for an individual electrode within the array. We use the term *non-point-electrode effect* to refer to the difference between measurements made with point electrodes and those made with non-point electrodes, and *finite-tissue-size effect* to refer to the difference between measurements in a semi-infinite tissue and those in a finite-size tissue.

## II. Methods

Our study consists of two parts: (1) computer simulations studying the effects of electrode and tissue geometries on the apparent resistivities and anisotropy ratio and (2) experimental measurements from real tissues for verification.

### A. Finite element simulations

Although a solution can be analytically obtained for the ideal situation where four infinitesimally small electrodes are placed on the surface of a semi-infinite tissue [68], no analytic solution exists for the case where electrodes and tissue volume are both of finite size. We therefore chose to perform simulations using the FE approach. The 3D FE solver that we have developed allows us to solve large anisotropic volume

conduction problems [11][35][36]. For a detailed description of the FE solver, see Section II. *B.* of Chapter 1. The linear equations in the models are solved iteratively, stopping when the RMS difference between the left- and right-hand sides normalized to the RMS of the right-hand side is less than 0.03% [11].

The 3D model used in simulation is shown schematically in Figure 3.1. Four equally-spaced electrodes are placed in the center of the top square surface of a conducting volume, aligned parallel to one side of the medium. The electrodes penetrate the top surface into the medium, and their length and diameter within the medium are  $EL$  and  $ED$ , respectively. The voltages ( $V$ ,  $V_L$ , or  $V_T$ ) predicted from the models and the delivered current ( $I$ ) were used in Eqs. (3.1) - (3.4) to derive the apparent resistivities and anisotropy ratio. For an anisotropic medium, the principal axes of  $\rho_L$  and  $\rho_T$  were aligned to the two sides of the volume. Our uniform meshing scheme creates cubical elements for the FE model.

In view of the linearity of the governing Laplace equation, all geometric dimensions were unitless and relative to the size of the finite elements. The tissue volume was chosen as  $128 \times 128 \times 100$ , where the tissue size (TS) is 128 and tissue depth (TD) is 100. The  $ED$  of non-point-electrodes was taken to be 1, which is identical to the element size. The resistivities were also taken as unitless. For isotropic tissues, the true resistivity ( $\rho$ ) was set to unity. For tissues with low anisotropy, the true resistivities were  $\rho_L = 1$  and  $\rho_T = 2$ , with  $\alpha = 2$ . For highly anisotropic tissues, the true resistivities were chosen as  $\rho_L = 1$  and  $\rho_T = 10$ , with  $\alpha = 10$ , which is typical for the literature results for muscle tissue [16][17][21][27][69][99].

We began by simulating the electrodes as point electrodes ( $EL = ED = 0$ ) and comparing the apparent resistivities and anisotropy ratios with the true values. This allows an assessment of the finite-tissue-size effect. Next, we simulated non-point electrodes ( $ED = 1$ ,  $EL > 0$ ). The effects of non-zero  $ED$  and  $EL$  were assessed by comparing point-electrode and non-point-electrode simulation results.

### ***B. In vitro resistivity measurements***

To verify the prediction of the FE simulation, we performed an *in vitro* experiment in which we measured resistivities of the skeletal muscle of a pig. We used four different probes with dimensions listed in Table 3.1. The current-delivering electrodes were made of platinum, and the voltage-sensing electrodes were made of silver/silver chloride. The electrodes were fixed in a flat insulating plastic material that acted as a mechanical support for the probes.

Resistivity measurements were taken at sixteen different locations on the tissue sample for each probe. Measurements at each location consisted of longitudinal and transverse voltages. The probe alignment with regard to the muscle fiber direction was determined by visual inspection.

A 45-msec current pulse ( $500\ \mu\text{A}$  -  $1\ \text{mA}$ ) was delivered using a voltage-controlled current source and measurements were taken at the end of the pulse, so only the low-frequency tissue impedance was measured, which reflects its real part, i.e., resistivity. Measured voltages were conditioned by an instrumentation op-amp that has a low noise level of  $0.3\ \mu\text{V}_{\text{p-p}}$ , an input impedance of  $10^9\ \Omega$ , a CMRR of 95 dB at  $1\text{k}\Omega$  source imbalance, and a bandwidth of 2.5 MHz at gain of 10 (AD524B Precision Instrumentation Amplifier, Analog Devices, Norwood, MA).

A farm pig weighing 30 kg was used in the experiment. Immediately after the pig was euthanized, skeletal muscle samples were excised from the gluteus maximus muscle, with a square cross section of approximately 10 cm x 10 cm and thickness of 7 cm. All the measurements were completed within one hour of euthanasia, which has been shown not to change the measured resistivities significantly [99]. During the measurements, the lower half of the sample was immersed in saline, and the top surface was rinsed intermittently with saline to prevent tissue drying but cleared of fluid during measurement to prevent shunting between the electrodes.

### III. Results

#### A. Simulation results

##### A.1 Resistivities

Figure 3.2(a) shows simulated  $\rho_e$  in an isotropic tissue. For the point-electrode probe, when IES is small, the derived resistivity ( $\rho_e$ ) from Eq. (3.1) is close to 1, the true resistivity,  $\rho$ . As IES increases relative to the tissue size,  $\rho_e$  increases as well. For the point-electrode probe, this increasing deviation from the actual resistivity value due to increasing IES reflects the finite-tissue-size effect.

The non-point-electrode effect, which is due to finite ED and EL, is seen in the percentage difference between point-electrode and non-point-electrode measurements. In order to isolate the non-point-electrode effect from the finite-tissue-size effect, we normalized  $\rho_e$  measured with the non-point-electrode probes by  $\rho_e$  measured with the point-electrode probe (Figure 3.2(a)), and we plotted the result in Figure 3.2(b). The use of non-point electrodes reduces  $\rho_e$  for small IES, but has little effect when IES is large. For example, when IES = 7, as the electrode increases from the point electrode to ED = 1 and EL = 1, 5 and 9,  $\rho_e$  decreases by 2%, 23% and 40%, respectively. When IES = 39, it decreases only by 1%, 2%, and 3%.

Figure 3.3(a) and Figure 3.3(b) show  $\rho_{Le}$  (apparent longitudinal resistivity) and  $\rho_{Te}$  (apparent transverse resistivity) in an anisotropic tissue with  $\rho_L = 1$  and  $\rho_T = 2$ , i.e.,  $\alpha = 2$ . Due to the finite-tissue-size effect,  $\rho_{Le}$  and  $\rho_{Te}$  measured by the point-electrode probe increase as IES increases. To assess the non-point-electrode effect, we normalized  $\rho_{Le}$  and  $\rho_{Te}$  measured with the non-point-electrode probes by those measured with the point-electrode probe and multiplied them by the true values ( $\rho_L = 1$ ,  $\rho_T = 2$ ), with the results shown in Figure 3.3(c). The non-point-electrode effect reduces both  $\rho_{Le}$  and  $\rho_{Te}$ , but the effect is more significant in the transverse direction. When IES = 7, probes with ED = 1 and EL =

1, 5 and 9 reduce  $\rho_{Le}$  by 3%, 13% and 28%, respectively, but reduce  $\rho_{Te}$  by 8%, 36% and 54%. As in the isotropic situation, the non-point-electrode effect is more pronounced when IES is small than when IES is large.

Figure 3.4(a) and Figure 3.4(b) show  $\rho_{Le}$  and  $\rho_{Te}$  in an anisotropic tissue with  $\rho_L = 1$  and  $\rho_T = 10$ , i.e.,  $\alpha = 10$ . Due to the finite-tissue-size effect, the measured  $\rho_{Le}$  and  $\rho_{Te}$  increase as IES increases. Similar to Figure 3.3(c),  $\rho_{Le}$  and  $\rho_{Te}$  measured with the non-point-electrode probes were normalized using the values measured with the point-electrode probe and multiplied by the true values ( $\rho_L = 1$ ,  $\rho_T = 10$ ), and the results are shown in Figure 3.4(c). The non-point-electrode effect affects  $\rho_{Le}$  and  $\rho_{Te}$  differently: when IES = 7, probes with ED = 1 and EL = 1, 5 and 9 raise  $\rho_{Le}$  by 31%, 67% and 58%, respectively, but reduce  $\rho_{Te}$  by 22%, 62% and 75%.

## A.2 Anisotropy ratios

The apparent anisotropy ratios ( $\alpha_e$ ) are calculated from Figure 3.3(c) and Figure 3.4(c), and plotted in Figure 3.3(d) and Figure 3.4(d), respectively. Due to the finite-tissue-size effect,  $\alpha_e$  measured with the point-electrode probe is close to  $\alpha$  for small IES, but  $\alpha_e$  decreases as IES increases. To isolate the non-point-electrode effect, we normalized  $\alpha_e$ 's from the non-point-electrode probes by those from the corresponding point-electrode probes and multiplied them by the true anisotropy ratios of 2 and 10 (Figure 3.3(e) and Figure 3.4(e)). In both (low and high anisotropy) cases, the non-point-electrode effect reduces  $\alpha_e$ , but the effect is more pronounced for small IES than for large IES. For example, when IES = 7 (Figure 3.4(e)), non-point-electrode probes with EL = 1, 5 and 9 underestimate  $\alpha$  by 41%, 77% and 84%, respectively. When IES = 39, non-point-electrode probes with EL = 1, 5 and 9 underestimate  $\alpha$  by 6%, 20% and 37%.

Figure 3.3(d) and Figure 3.4(d) also show that  $\alpha_e$  deviates more from  $\alpha$  as  $\alpha$  increases. For example, when EL = ED = 1 and IES = 11,  $\alpha_e/\alpha$  is 94% for  $\alpha = 2$ , but 61% for  $\alpha = 10$ .

## ***B. Experimental results***

Experimental results using an *in vitro* muscle sample of 10 cm x 10 cm x 7 cm are shown in Figure 3.5 and Table 3.1. The four probes with different IES and EL exhibited significant differences. The  $\alpha_e$  values measured by the probes with smaller IES/EL are smaller than those measured by the probes with larger IES/EL. As we discuss below, these results agree qualitatively with the computer simulation results.

## **IV. Discussion**

### ***A. Finite-tissue-size effect***

The finite-tissue-size effect on the resistivity measurement has been investigated both in isotropic and anisotropic tissues. Suesserman and Spelman [86] conducted computer simulations of a hollow spherical insulator filled with saline and a linear four-point-electrode array located in its center. Their result demonstrated that the measured voltage, and therefore the measured resistivity according to Eq. (3.1), increases with increasing IES. Steendijk *et al.* [81] solved analytically the case where a four-point-electrode probe is placed on one side of an infinitely-extended layer of tissue with finite thickness. Their solution showed that the larger the IES relative to the tissue thickness, the larger the deviation of  $\rho_e$  (or  $\rho_{Te}$  and  $\rho_{Le}$ ) from the actual value. It also showed that the measured anisotropy ratio  $\alpha_e$  decreases as the IES is increased, and the deviation is larger when the true ratio  $\alpha$  is larger. These results agree with our simulation findings for the finite-tissue-size effect.

That the finite-tissue-size effect increases the measured resistivities is to be expected, since the current delivered by the probe only flows through a limited tissue volume as opposed to the ideal situation where the current flows through an infinite tissue volume, and thus the apparent resistance seen by the probe is increased. This results in an increase in the measured voltage for a constant current, and thus an increase in the apparent resistivities.

Because all sizes in our simulation are dimensionless, it is only the ratios of electrode and tissue dimensions (IES to TS and IES to TD) that matter in the finite-tissue-size effect.

## ***B. Non-point-electrode effect***

### *B.1 Analysis*

The non-point-electrode effect has not been studied as extensively as the finite-tissue-size effect. Our simulation shows that the non-point-electrode effect increases  $\rho_{Le}$  and lowers  $\rho_{Te}$  for medium with high anisotropy ( $\alpha = 10$ ), but lowers  $\rho_{Le}$  and  $\rho_{Te}$  for medium with low anisotropy ( $\alpha = 2$ ). The change in  $\rho_{Te}$  can be understood. When EL or ED increases, the total medium resistance between the current-delivering electrodes decreases. Thus, the voltage drop between the constant-current-delivering electrodes decreases, and so does  $V_L$  and  $V_T$  measured by the voltage-sensing electrodes. Therefore,  $\rho_{Te}$  decreases according to Eq. (3.2). The change in  $\rho_{Le}$  is determined by which of  $V_L$  and  $V_T$  decreases faster in Eq. (3.3) as EL or ED increases, which appears to depend on the medium anisotropy. How this dependence is precisely related to the interaction between the finite-tissue-size and non-point-electrode effects is not yet known. Regardless of the degree of medium anisotropy, the non-point-electrode effect always reduces  $\alpha_e$ .

Because of the relative sizes in our simulation, the non-point-electrode effect is determined only by the ratios of electrode dimensions (IES to ED and IES to EL). Based on the data in Figure 3.3(d) and Figure 3.4(d),  $\alpha_e$  obtained in the simulations was fitted to the following equation:

$$\alpha_e = \frac{\alpha}{\left[1 + k_1 \left(\frac{EL}{IES}\right)^2 (\alpha - 1) + k_2 \left(\frac{ED}{IES}\right)^2 (\alpha - 1)\right] \cdot \left[1 + k_3 \left(\frac{IES}{TS}\right)^2 (\alpha - 1)\right]} \quad (3.5)$$

in which the first bracket in the denominator represents the non-point-electrode effect and the second bracket represents the finite-tissue-size effect. A nonlinear regression (S-

PLUS, StatSci, Seattle, WA) was performed on Eq. (3.5), yielding the following parameters (mean $\pm$ SE):  $k_1 = 0.72\pm 0.06$ ,  $k_2 = 1.64\pm 0.41$ , and  $k_3 = 7.11\pm 0.27$  with an 11% average residual error in  $\alpha_e$ . Since the non-point-electrode effect is often difficult to evaluate in experiments, Eq. (3.5) can be used to estimate the possible error and to optimize EL, ED, and IES in designing four-electrode arrays.

Caution should be taken when interpreting the simulation results for very small IES. Due to the limitation of the FE models, we were not able to study the non-point-electrode effect for very small IES. Most of the practical four-electrode probes, however, satisfies  $IES/ED > 5$  and therefore the simulation results and Eq. (3.5) should be applicable.

These simulation results have an important implication. In many published tissue resistivity studies, probes are often calibrated in saline to correct the experimental data [27]. That the non-point-electrode effect may be different for  $\rho_{Le}$  and  $\rho_{Te}$  suggests that probe calibration in an isotropic medium may not correctly compensate for non-point-electrode effects on measurements in anisotropic media.

### *B.2 Comparison of simulation with experimental results*

Our *in vitro* experiment also exhibited the non-point-electrode effect. The muscle tissue approximated a square cross section with  $TS = 10$  cm and  $TD = 7$  cm, so the  $TS/TD$  ratio is similar to that in the simulation. The probes with IES of 5 mm and 1 mm have  $IES/TS = 0.05$  and  $0.01$ , corresponding to  $IES = 6.4$  and  $1.28$  in Figure 3.1 - Figure 3.4, respectively, suggesting that the finite-tissue-size effect is negligible for the 1-mm probes and marginal for the 5-mm probes. Neglecting the finite-tissue-size effect, we compared the experimental measurements with the simulation results using Figure 3.4(e), in which  $\alpha = 10$ , typical for the published muscle anisotropy ratios.

The geometric dimensions of the probes used in the experiments are marked as I, II, III and IV on Figure 3.4(e) according to the ratios of  $IES/EL/ED$  in Table 3.1. Probes I and II have  $EL/ED = 1.5$  and do not fall on any of the curves in Figure 3.4(e), so they are

placed on the nearest curve ( $EL/ED = 1$ ). It can be seen that the non-point-electrode effect lowers  $\alpha_e$  measured by probes I, II, III and IV by 9%, 41%, 31% and 77%, respectively. The probes affected from the least to the most are I, III, II and IV, in agreement with the ranking of the experimentally-measured  $\alpha_e$  from the highest to the lowest. According to Figure 3.4(e) which assumes a true  $\alpha$  of 10, the four probes should measure much higher anisotropy ratios than the experimentally-measured values. Possible reasons for the discrepancy include: (1) the true  $\alpha$  in the *in vitro* experiment may be less than 10, and (2) intermittent rinsing of the muscle tissue with saline during the experiments might have reduced  $\alpha_e$ .

### B.3 Comparison of simulation with literature results

Our simulation results suggest that the non-point-electrode effect might contribute to the large variations in the anisotropy ratios reported in the literature. We compared our simulation with the results by Gielen [27] and Rush [69] listed in Table 3.2. We ignored the finite-tissue-size effect in view that their experiments were on live animals where tissue size was likely much larger than IES. The geometries of Gielen's probes are marked as G1 and G2 on Figure 3.4(e), which shows that if the true anisotropy ratio is 10, these probes would measure an anisotropy ratio of 2.5 (G1) and 7 (G2). This approximately agrees with the measured anisotropy ratios by Gielen in Table 3.2. The geometry of Rush's probe is marked as R1 on Figure 3.4(e), which is obviously less affected by the non-point-electrode effect than Gielen's probes. It is therefore reasonable that the anisotropy ratio measured by Rush was higher (9.2).

## V. Conclusions

Our FE simulation results strongly support the need for careful attention to geometry in the design of four-electrode probes used to measure tissue resistivities, particularly in anisotropic tissues. Both the non-point-electrode and the finite-tissue-size effects can affect the measured resistivity values and anisotropy ratios. Since the non-point-electrode

effect is much less understood than the finite-tissue-size effect, this study concentrated mainly on the former.

Our simulation shows that in an anisotropic tissue, the non-point-electrode effect lowers the measured transverse resistivities but affects the measured longitudinal resistivities differently depending on the tissue anisotropy, and the finite-tissue-size effect increases the measured resistivities. Both effects contribute to lowering the measured anisotropy ratio. These effects are more marked for tissues with higher anisotropy ratios. The simulation findings are supported by our experimental results. Since *in vivo* measurements often involve relatively large tissue sizes, the non-point-electrode effect may affect the measurements more severely than the finite-tissue-size effect. Eq. (3.5) can be used to minimize the non-point-electrode effect in probe design.

TABLE 3.1. *In vitro* measurements of skeletal muscle resistivities in a pig (TS = 10 cm, TD = 7 cm). EL: electrode length, ED: electrode diameter, IES: interelectrode spacing, TS: tissue size, TD: tissue depth.

Four-electrode probe geometry					Mean resistivity ( $\Omega\text{-cm}$ )		Anisotropy ratio $\alpha_e$
Probe #	IES (mm)	EL (mm)	ED (mm)	IES/EL/ED	$\rho_{Le}$	$\rho_{Te}$	
I	5.0	0.3	0.2	25 / 1.5 / 1	464	1745	3.8
II	1.0	0.3	0.2	5 / 1.5 / 1	394	536	1.4
III	5.0	1.0	0.2	25 / 5 / 1	657	1186	1.8
IV	1.0	1.0	0.2	5 / 5 / 1	215	234	1.1

TABLE 3.2. Measured anisotropy ratios of skeletal muscle vs. probe geometries from literature

Four-electrode probe geometry						Anisotropy ratio $\alpha_e$
Probe #	Researcher	IES (mm)	EL (mm)	ED (mm)	IES/EL/ED	
G1	Gielen [27]	0.5	0.5 <sup>1</sup>	0.1	5 / 5 / 1	2
G2	Gielen [27]	3.0	0.5 <sup>1</sup>	0.1	30 / 5 / 1	6
R1	Rush [69]	5.0	0.5 <sup>2</sup>	0.2 <sup>3</sup>	25 / 2.5 / 1	9.2

Note: 1. EL = 0.5 mm is estimated from the statement that EL < 1.0 mm.

2. EL = 0.5 mm is estimated from the statement that the electrodes only touched the tissue surface.

3. ED = 0.2 mm is estimated from the statement that needle electrodes were used.

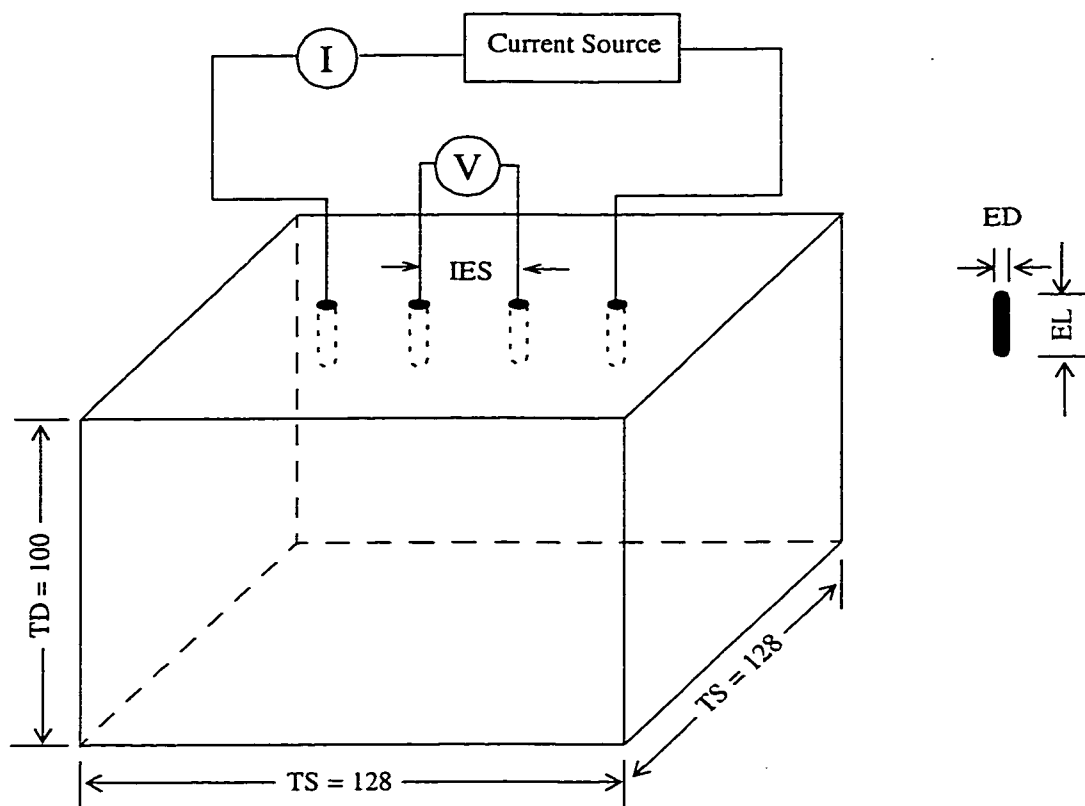


FIGURE 3.1. A sketch of tissue resistivity measurements using four electrodes. The four-electrode probe is placed on the surface and penetrates into the tissue. All dimensions are relative to ED ( $ED = 1$ ). IES: interelectrode spacing, EL: electrode length inside the tissue, ED: electrode diameter, TS: tissue size, TD: tissue depth.

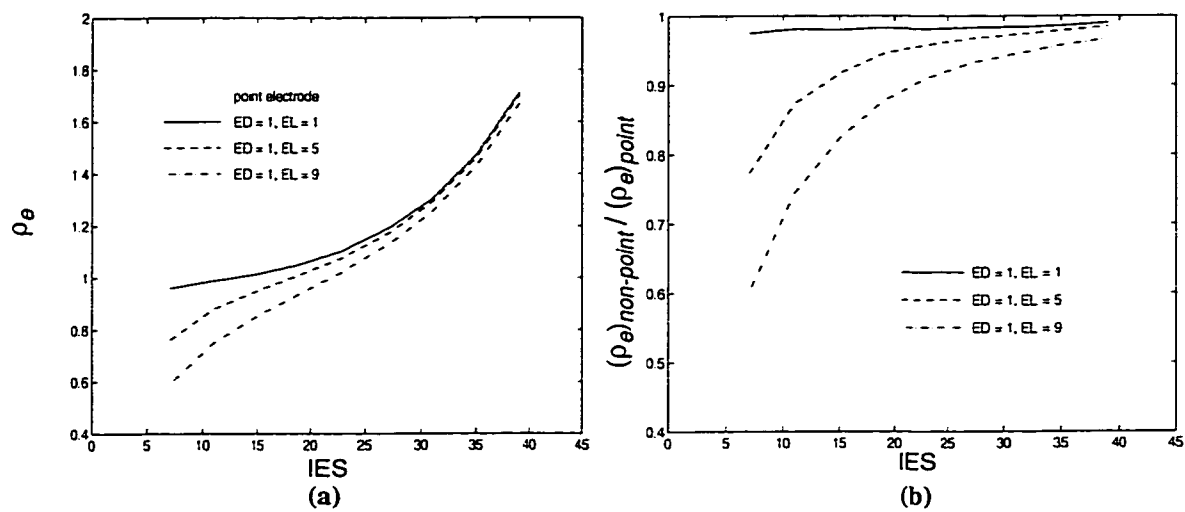


FIGURE 3.2. Simulated measurements in the isotropic model with  $\rho = 1$ . (a)  $\rho_e$ , (b) the ratio of  $\rho_e$  (non-point-electrode) to  $\rho_e$  (point-electrode).

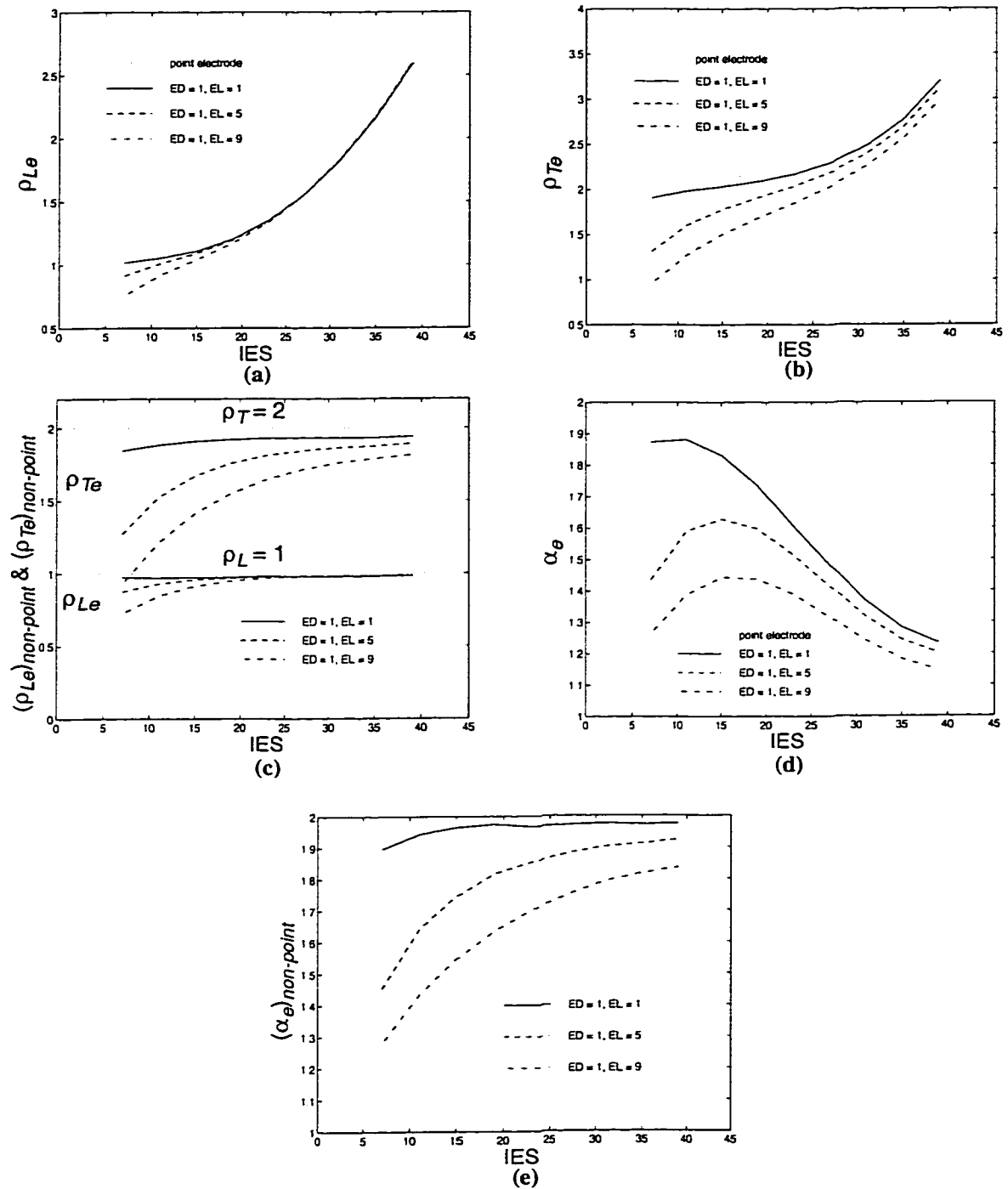


FIGURE 3.3. Simulated measurements in the anisotropic model with  $\rho_L = 1$  and  $\rho_T = 2$ . (a)  $\rho_{Le}$ , (b)  $\rho_{Te}$ , (c) the non-point-electrode effect on  $\rho_{Le}$  and  $\rho_{Te}$ , (d)  $\alpha_e$ , (e) the non-point-electrode effect on  $\alpha_e$ .

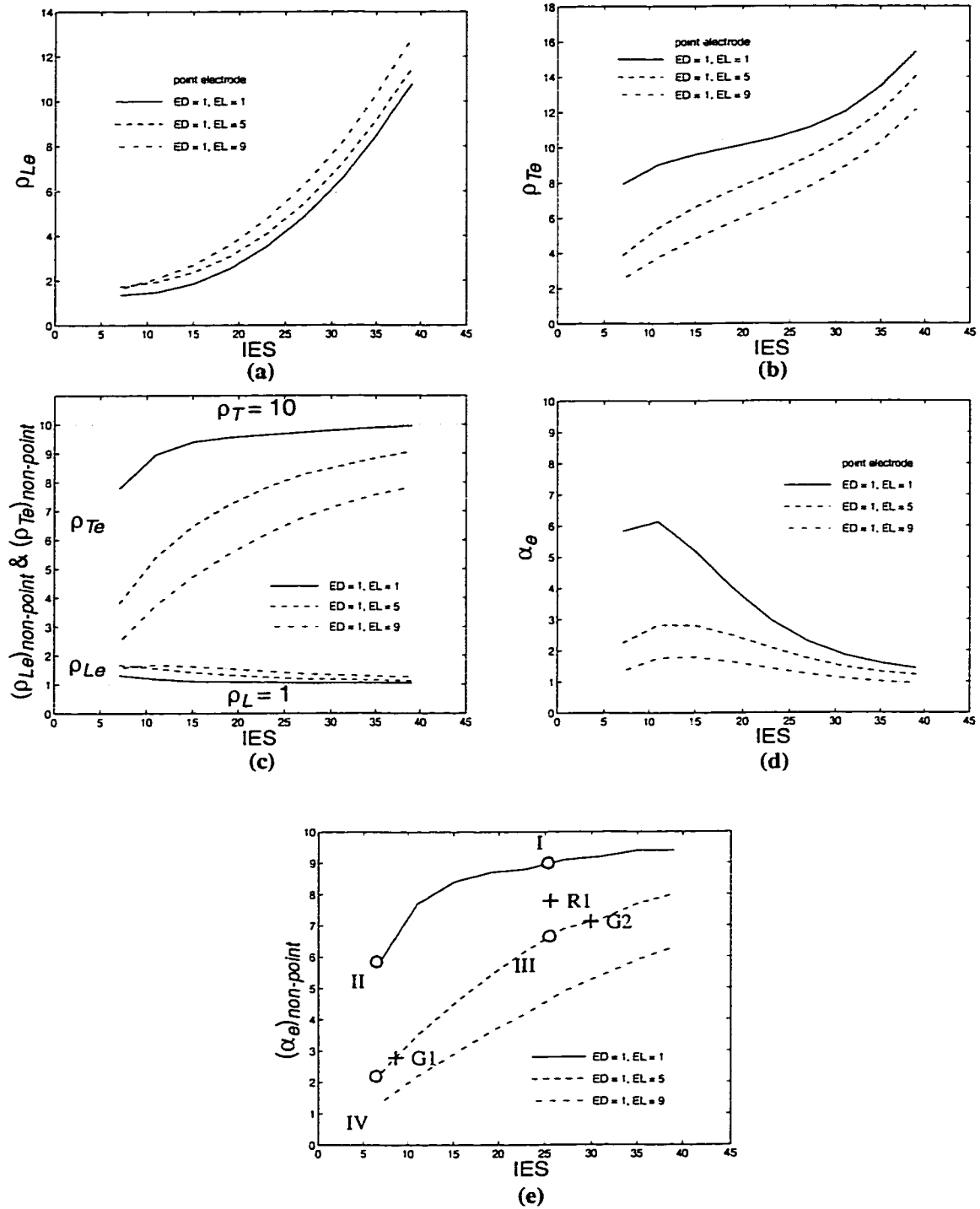


FIGURE 3.4. Simulated measurements in the anisotropic model with  $\rho_L = 1$  and  $\rho_T = 10$ . (a)  $\rho_{Le}$ , (b)  $\rho_{Te}$ , (c) the non-point-electrode effect on  $\rho_{Le}$  and  $\rho_{Te}$ , (d)  $\alpha_e$ , (e) the non-point-electrode effect on  $\alpha_e$ . "o": probes listed in Table 3.1. "+": probes listed in Table 3.2.

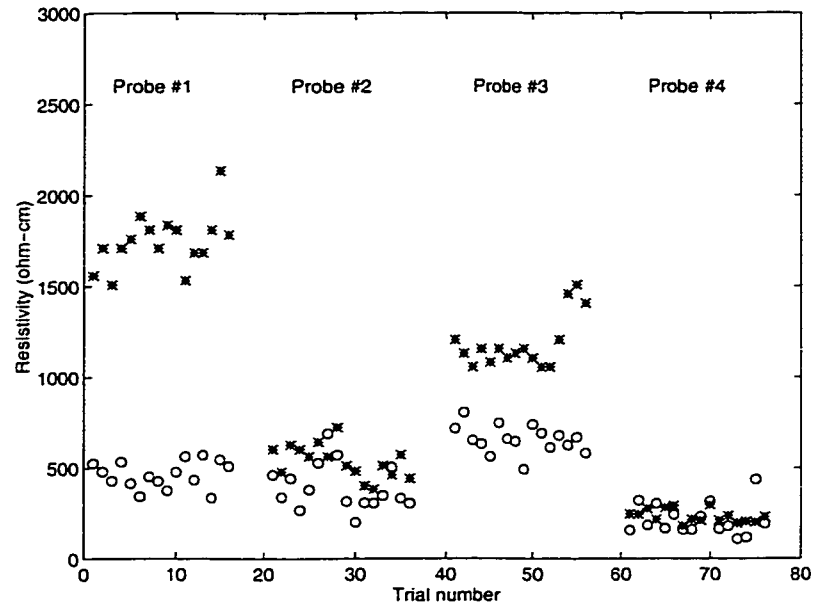


FIGURE 3.5. *In vitro* measurements of  $\rho_{Te}$  and  $\rho_{Le}$  of a pig's skeletal muscle using 4 four-electrode probes of different geometry. Probe numbering is the same as in Table 3.1. \*:  $\rho_{Te}$ , o:  $\rho_{Le}$ .

## Chapter 4. A Finite Element Study of the Effects of Electrode Position on the Genesis of Impedance Change in Impedance Cardiography

### I. Introduction

Impedance cardiography (ICG) is a technique for measuring changes in the thoracic electric impedance that occurs with each heart beat [43]. The interest in ICG stems from its potential for noninvasive measurement of cardiac hemodynamic functions, namely stroke volume (SV) and cardiac output, and systolic time interval [33].

The ability of ICG to measure beat-by-beat SV is based on the plethysmographic principle. Plethysmography is one of the oldest and most useful methods for flow measurement, and has wide applications [96]. It assumes that the organ whose impedance is being measured has a cylindrical shape, with blood vessel cylinders running inside and parallel to the organ cylinder. When blood vessels change their diameter, the vessel volume change is linearly related to the impedance change measurable across the two ends of the organ cylinder [26][93]:

$$\Delta vol = -\rho \cdot \left(\frac{L}{Z_0}\right)^2 \cdot \Delta Z \quad (4.1)$$

where  $\rho$  is the resistivity of the blood,  $L$  is the length of the cylinders,  $Z_0$  is the baseline impedance when the vessels are in the resting (diastolic) state, and  $\Delta vol$  and  $\Delta Z$  are the changes in vessel volume and organ impedance, respectively. The negative sign signifies that the increase of blood volume decreases impedance. Plethysmography has been successfully applied to measure blood flow in fingers [55]. The principle can also be applied in the detection of pulmonary edema by monitoring changes in fluid volume in the chest [44]. To apply the plethysmographic principle to the thorax for the ICG

measurement of cardiac output, the assumption is made that major vessels in the thorax can be approximated as cylinders parallel to the long axis of the thorax, and that it is the pulsatile flow in the major vessels that causes the observed pulsatile change in thoracic impedance [26]. If the major vessels are the ascending and descending aorta, and the measurement is taken between end-diastole and end-systole,  $\Delta vol$  in Eq. (4.1) becomes the stroke volume, SV.

Numerous studies have shown significant correlations (0.63 - 0.97) between the SV measured with Eq. (4.1) and those using invasive clinical methods [33][39]. Although correlation results are encouraging, data on the absolute errors in SV measured by the ICG method are scarce and no statistically significant conclusion can be drawn. In general, the available studies have reported a huge variation in the errors [33]. Some studies have also found that the method tends to fail in pathological conditions, such as for patients with severe heart disease [33][43]. The inaccuracy of the cylinder model of the thorax and the differences among subjects prompted Sramek *et al.* [80] and Bernstein [10] to modify the thorax as a truncated cone and add a correction factor to accommodate individual body habitus. However, experiments showed that the new methods improved the results very little [33]. Overall, ICG has not achieved a broad clinical acceptance due to conflicting results and a lack of understanding of the electrophysiological causes underlying the thoracic impedance change.

The true structure of the thorax is highly complex, in contrast to the plethysmographic assumptions underlying Eq. (4.1). The high degree of inhomogeneity of tissues and the complexity of physiological events in the thorax all influence the impedance change during a cardiac cycle. Four possible sources are considered to be the major contributors to the change in thoracic impedance from end-diastole to end-systole: (1) the decrease in ventricular blood volume, (2) the increase in aortic volume, (3) the decrease in lung resistivity due to increased blood perfusion, and (4) the decrease in blood resistivity due to alignment of the erythrocytes in the arteries during systole [49]. The plethysmographic principle for Eq. (4.1) is only valid if blood volume change in the

aorta is more significant than the other factors combined.

The ICG's conventional band-electrode configuration uses four band electrodes encircling the thorax, with the outer pair of electrodes delivering a constant current and the inner pair measuring the voltage (Figure 4.1(a)) [43]. The applied current has an amplitude of 2.5 - 4 mA and a frequency of 70 - 100 kHz. The impedance is measured by dividing the measured voltage by the applied current, and typically changes by 0.25  $\Omega$  over a cardiac cycle. Using FE and finite difference models, Kim *et al.* [38] and Wang and Patterson [91] have shown that all four sources contribute to the ICG signal with comparable strength. The models used by Kim *et al.* were based on an anatomical atlas, while those used by Wang and Patterson were based on gated sequences of MR images of a human thorax. Both authors concluded that the ICG signal is a mixed representations of the four factors, in which none dominates the rest.

The advent of spot electrodes, introduced to improve the ease of electrode placement and comfort level for patients, opened up new possibilities for ICG (Figure 4.1(b)) [57][58][98]. Qu *et al.* found that spot electrodes provide a better signal-to-noise ratio (SNR) than the band electrodes. This is because (1) ICG signal varies with electrode location, and (2) spot electrodes can be placed where motion artifact is minimum [61], so it is possible to optimize spot electrode location for best SNR, while band electrodes are limited in the choice of locations [1][61]. Adamicza *et al.* demonstrated on dogs that the impedance-based SV measurement with spot electrodes on the anterior chest wall was significantly different from that measured with band electrodes [1]. Woltjer *et al.* found that the baseline impedance measured with spot electrodes positioned laterally was significantly higher than that measured with band electrodes at the same level, causing the measured SV to be smaller than that measured with band electrodes [95]. Moreover, Patterson *et al.* showed that measurement taken between the xiphisternal joint and a point 10 cm below the suprasternal notch yielded an impedance change opposite to what would be measured by the band electrodes, a phenomenon that is not understood [57]. These findings all point to the complex, inhomogeneous nature of the thorax. That the impedance

and its changes measured by spot electrodes vary with electrode position even at the same level suggests that electrode position relative to the sources of impedance change is also important, and the effect needs to be studied in detail.

We hypothesized that a simulation of the effects of electrode location might provide an insight into how different sources contribute to the impedance change in ICG, and could also provide information about how spot electrodes can be used more effectively. If one source can be separated from the others by optimizing electrode position, a more physiologically meaningful measurement can be made. Therefore, this study investigated the following issues: (1) how the aforementioned sources affect the impedance change measured at different locations by spot electrodes, and (2) consequently how spot electrodes can be more effectively used. The FE method based on realistic human thorax models was used in the study.

## II. Methods

### A. *Models of human thorax*

The procedure in constructing the diastolic and systolic thorax models is schematically shown in Figure 4.2.

Images of a healthy male subject (age 32, 145 pound) were used for model construction. First, a non-gated T1-weighted MRI scan (GE Signa Horizon 5.7, 1.5 Tesla) was obtained, covering the region from neck to lower abdomen with contiguous 6-mm slices (Figure 4.2 (a)). Next, a 6-mm cine scan, gated with the R wave in the ECG, was performed covering the whole extent of the heart with 60 mm fringe at the top and 18 mm at the bottom. For each cross-section of the heart in the cine scan, 16 slices were taken at 46-ms intervals, spanning the entire cardiac cycle for the subject whose heart rate was 81. Respiratory compensation was applied. The imaging voxel size was 1.25x1.25x6.0 mm.

After scanning, the cine MR images of the heart were played back, and the end-diastolic and end-systolic phases were determined visually. Two end-diastolic and end-

systolic MR scans of the heart at the same level and their respective classified images are shown in Figure 4.3. The images at the two phases were then used to replace the same thoracic portion in the static scan of the whole thorax to form two sets of thoracic images at end-diastole and end-systole, respectively, each having 42 images (Figure 4.2 (b)). These digitized MR images were segmented into 30 tissue types using an X-window based semi-automated tissue segmentation tool developed in our lab [76]. The two sets of segmented images, when stacked in order, form the 3D end-diastolic and end-systolic thoracic models of the scan subject (Figure 4.2 (c)). Although vessels change their dimension between the two phases, only major vessels close to the heart change the most and contribute to the impedance change much more significantly than peripheral vessels. The 60-mm fringe at the top of the heart in the cine scan is sufficient to capture the changes in aortic dimensions.

Since classification requires some manual editing, random classification errors exist in the classified images. In addition, respiration has been shown to have an effect 3-6 times as much as the impedance change measured by ICG [15]. Even though respiratory compensation was used, small artifacts due to respiration still exist on the MR images. Thus the background tissues surrounding blood vessels and myocardium may differ between the end-diastolic and end-systolic models, which can introduce random errors into the results. To minimize these errors, we extracted the background thoracic model from the end-systolic model by replacing the blood and myocardium with fat, and extracted the two blood and myocardium foregrounds from the end-diastolic and end-systolic models (Figure 4.2 (d)). The final modified end-diastolic and end-systolic thoracic models were formed by “merging” the two foregrounds with the background model - replacing the background with the foreground voxels where the foreground is blood or myocardium, so that the two models have the same background (Figure 4.2 (e)). Such modification does not distort the realistic nature of the models while reducing random errors. FE analyses were then performed on these two modified 3D thorax models.

## ***B. FE method***

We refer the readers to Chapter 1, Section **II B** for details on the adaptive FE solver.

For the 3D realistic human thorax models, each voxel has a size of 1.25x1.25x6.0 mm, an aspect ratio of 1:1:4.8. In order to improve the element aspect ratio, images were down-sampled from 256x256 to 128x128, making the aspect ratio 1:1:2.4. Generic tissue specific resistivities taken from the literature [25][72] were used in the FE models (Table 4.1, except for the systolic resistivities of aortic blood and lungs, see below). The band electrodes encircling the thorax for current delivery were placed at the two distal ends of the models (Figure 4.4). A constant-current boundary condition ( $I = 1$  mA) was applied between this pair of electrodes. Voltages relative to the bottom current-delivery electrode were calculated over the skin surface, just as if using a spot electrode. To see how the four sources affect the measured thoracic impedance, the change in the skin voltage from end-diastole to end-systole (i.e.,  $\Delta V = V_{systole} - V_{diastole}$ ) was then calculated. By definition, the change in impedance between the voltage-sensing spot and the bottom current electrode from end-diastole to end-systole is  $\Delta Z = \Delta V / I = Z_{systole} - Z_{diastole}$ . The average impedance change on the skin surface over a cross-section is approximately what would be measured by a band electrode encircling the same cross-section. The thorax models in this study do not include the arms, so the band electrodes can be placed at any level of the thorax. In addition to mapping  $\Delta Z$  over the skin surface, ICG measurements with some practically-useful band- or spot-electrode configurations were also simulated and analyzed in a similar way.

The algorithm was run on a Pentium-II PC (233 MHz, Linux OS) containing 128 Mbytes of main memory. Each thorax model, which on average has 240,000 elements and 280,000 nodes, was solved in 7 minutes. This allowed a thorough parametric study of the relative contributions from different sources, as well as the effects of the electrode position.

### *C. Sources of impedance change in ICG*

The effects of the four sources were studied in two ways: (1) by observing each factor while keeping the others unchanged, and (2) by observing a combination of different factors that occur simultaneously.

The effect of ventricular contraction alone on impedance change was studied by keeping the myocardium and the blood within the heart chambers while replacing all the blood outside the heart with fat, which in most cases constitutes the background for blood vessels.

The effect of the expansion of major vessels (aorta in particular) in the thorax was studied in a similar way by generating models in which the myocardium and the blood within the heart were replaced by fat, while the blood in the remainder of the vessels was preserved.

In order to examine the accuracy of the plethysmographic principle for ICG, which assumes that the impedance change is caused by the change in vascular structure, the combined effect of ventricular contraction and major-vessel expansion was also simulated.

The lung resistivity changes between end-diastole and end-systole due to the increase of blood volume in the lungs following contraction of the RV. This causes a systolic drop in lung resistivity. Given the resistivity of lungs ( $\rho_l$ ) at end-diastole, the resistivity of blood ( $\rho_b$ ), and the fractional increase of blood volume in lungs ( $v$ ), Fricke's method was used to calculate the effective systolic lung resistivity  $\rho_l'$  by solving the following equation [24]:

$$\frac{\frac{\rho_l}{\rho_l} - 1}{\frac{\rho_l}{\rho_l} + 2} = \frac{\frac{\rho_l}{\rho_b} - 1}{\frac{\rho_l}{\rho_b} + 2} \cdot v \quad (4.2)$$

With the two lung resistivities obtained, the end-diastolic and end-systolic thorax models were compared to estimate the effect of lung resistivity change.

The blood resistivity has also been shown to change with the blood flow velocity. This is caused by change in the orientation of the poorly-conductive erythrocytes in the highly-conductive blood plasma (“orientation effect”). This effect is particularly significant in the ascending and descending aorta where blood is ejected quickly from the ventricles. Visser quantitatively estimated the orientation effect on the blood conductivity through rigid circular tubes [89], and found that (1) the changes in blood conductivity are independent of the flow direction, and (2) the orientation effect generally increases the blood conductivity, or reduces the blood resistivity, by about 10%, and by up to 20% at maximum flow velocities. A 10% decrease in the blood resistivity in aorta (including ascending and descending aortas and the arch), carotid arteries, and superior and inferior vena cava was assumed in this study from end-diastole to end-systole, and the resulting impedance change was calculated.

Finally, all the four factors were brought into effect simultaneously and the total impedance change between end-diastole and end-systole was calculated. The effect of each individual source discussed above was then compared to the combined effect to examine the relative significance of each factor.

In each case, the electrode location was varied over the skin surface to see how it affects the contribution of each source. Some practical band- and spot-electrode configurations were also compared to observe how sources interact with each other and where some sources have their largest effect.

### **III. Results**

The blood volume change in both ventricles is evident in the classified end-diastolic and end-systolic images. Although the volume changes in LV and RV should be the same and equal to SV, there is a small difference due to image classification error. There-

fore,  $SV$  was measured as the average of the volume change in both ventricles. Measurement based on counting voxels in the 3D models gives a volume total decrease of  $126\text{ ml}$  in both ventricles from end-diastole to end-systole. The  $SV$  and thus the volume of blood perfused to lungs were  $63\text{ ml}$ . The blood volume increase in the major vessels in the thorax was measured to be  $51\text{ ml}$ , while the other  $12\text{ ml}$  of blood should have gone to the coronary arteries. The results are shown in Table 4.2, all in the range for a normal person [9].

The change in resistivities for aortic blood and lungs is listed in Table 4.1. The blood resistivity change simply reflects the 10% decrease from end-diastole to end-systole (see Methods). The lung resistivity at end-systole is calculated using Eq. (4.2). With the blood volume perfused into lungs of  $63\text{ ml}$  (Table 4.2) and the total lung volume measured from the images of  $2700\text{ ml}$ ,  $v = \frac{63}{2700} = 0.023$ . This results in a systolic lung resistivity of  $1424\ \Omega\text{-cm}$ , a 5% decrease from its diastolic value.

Figure 4.5 shows  $\Delta Z$  due to ventricular contraction, major-vessel expansion, and the two effects combined. These two effects represent the structural changes due to blood ejection between end-diastole and end-systole, allowing us to examine the validity of the plethysmographic assumptions for ICG. Figure 4.6 shows  $\Delta Z$  for the effects of blood and lung resistivity changes, and the combined effect of the four sources altogether. In both figures,  $\Delta Z$  is plotted at some evenly-spaced cross sections from top to bottom of the thorax. The marked cross-sectional levels correspond to the dash lines in Figure 4.4. At each level, the plot from left to right corresponds to circling the circumference in the order of left lateral, back, right lateral, heart, and left lateral. The numbers in the parentheses next to the levels indicate the circumferential length at each cross-sectional level. Since the lengths differ among different levels, each plot is stretched linearly to the same size for comparison. As a result, the horizontal axes in Figure 4.5 and Figure 4.6 do not have the same metric units. The point which is approximately  $3/4$  along the horizontal axes corresponds to the position on the anterior thoracic surface nearest the heart (“Heart” locations in Figure 4.5 and Figure 4.6).

In Figure 4.5, spot-electrode measurements close to the heart often give larger  $\Delta Z$  than what would be measured elsewhere on curves “V” and “V+M”, and they are also larger than the average values measured by band electrodes. This nonuniformity is seen as the bumps at the heart location on the curve “V” (ventricular contraction), and coincide with the bumps seen on the curve “V+M” (ventricular contraction and major-vessel expansion combined), while the curve “M” (major-vessel expansion) appears flatter. These suggest that it is mainly the heart that causes the nonuniform  $\Delta Z$ . Table 4.3 lists the  $\Delta Z$  values measured by a spot electrode at the heart location and by a band electrode at each level seen in Figure 4.5. In Figure 4.6, the bumps are still seen on the curve “V+M+B+L” for all four factors combined. The curves “B” (blood resistivity change) and “L” (lung resistivity change), however, appear much flatter, indicating a greater uniformity in their contribution to the measured  $\Delta Z$  at the circumference of a cross-section. The measured  $\Delta Z$  values in Figure 4.6 by a spot electrode at the heart and by a band electrode are listed in Table 4.4.

To further understand how differently the four sources affect  $\Delta Z$  measured by practical ICG devices using spot- or band-electrode configuration, the whole thorax was divided into three regions from top to bottom of the thoracic trunk: neck, upper thorax, and lower thorax (Figure 4.4). The three regions are shown in Figure 4.5 and Figure 4.6 as levels 4-19 (neck), levels 19-34 (upper thorax), and levels 34-39 (lower thorax). The impedance change was measured between (1) two band electrodes at levels 4 and 39 to measure the entire thorax, (2) two anterior spot electrodes at the heart locations at levels 4 and 39 to measure the entire thorax, (3) two anterior spot electrodes at the heart at levels 4 and 19 to measure only the neck, (4) two anterior spot electrodes at the heart at levels 19 and 34 to measure the upper thorax containing the heart, and (5) two anterior spot electrodes at the heart at levels 34 and 39 to measure the lower thorax. The measured  $\Delta Z$ s, as shown in Figure 4.7, were calculated from Figure 4.5 and Figure 4.6, and demonstrate the effects on the five different electrode configurations of not only each individual source, but also their combinations - sources that occur simultaneously.

Figure 4.7 shows that when an electrode configuration covers the heart (electrodes 1, 2, 4), ventricular contraction is the only significant factor to increase the thoracic impedance in systole, while the other three factors all contribute to a decrease or little change in impedance. If only the structural effects of ventricular contraction and major-vessel expansion were present (“V+M”), ventricular contraction would dominate and the combined effect would be to increase the whole thorax impedance at systole by 0.11  $\Omega$  measured with band electrodes (“1”) and 0.35  $\Omega$  measured with spot electrodes (“2”), and to increase the upper thorax impedance by 1.33  $\Omega$  measured with spot electrodes (“4”). However, when accounting for all four factors simultaneously (“V+M+B+L”), the net effect is to decrease the impedance of the whole thorax by 0.55  $\Omega$  with band electrodes (“1”) and 0.38  $\Omega$  with spot electrodes (“2”), but to increase the impedance of the upper thorax by 1.19  $\Omega$  with spot electrodes (“4”). This spatial heterogeneity in impedance change demonstrates the dominance of ventricular contraction in the upper thorax.

It should be pointed out that because of the way the individual and combined effects are defined in this study, these effects are not additive, e.g., the effects from each individual source do not algebraically add up to the combined effect of the four sources.

## IV. Discussion

### A. Ventricular contraction

The results show that among the four sources of impedance change, ventricular contraction is the only factor that tends to increase impedance, and is generally the most influential factor. This agrees qualitatively with the findings by Kim *et al.* [38] and Wang and Patterson [91]. That ventricular contraction tends to increase the thoracic impedance is easily understood. Following ventricular contraction, the volume of the highly conductive blood in the ventricles is quickly reduced. As rest of the tissues, including myocardium, have a much lower conductivity, drop in the ventricular blood volume significantly increases the impedance. This effect, however, makes a nonuniform contribution to the measured  $\Delta Z$  on the circumference at each cross-section level. This is

most obvious on the curves “V” and “V+M” in Figure 4.5 and “V+M+B+L” in Figure 4.6, in which bumps are easily seen at the skin locations near the heart. The fact that the heart is closer to the anterior than the posterior chest wall also explains why only one bump exists on each plot. Such signal nonuniformity has been observed frequently in experiments. Qu *et al.* found on human subjects that the measured  $\Delta Z$  peaked at the fourth rib when the spot electrode was moved from neck down to the xiphisternal joint and also peaked at the sternum when moved from left to right lateral sides [61]. It should be pointed out that in addition to the ventricular blood volume change, ventricular contraction as defined here also includes heart movement between end-diastole and end-systole.

Because of its large impact near the heart when using spot electrodes to measure  $\Delta Z$  in the upper thorax while all four factors occur simultaneously (“V+M+B+L” for spot electrodes “4” in Figure 4.7), ventricular contraction dominates the opposite effects of major-vessel expansion and blood- and lung-resistivity decrease combined, increasing the impedance by  $1.19 \Omega$ . This impedance change is 82% of the impedance change that would be measured by the spot electrodes in the upper thorax ( $1.45 \Omega$ ) supposing that ventricular contraction were the sole contributing factor (“V” for spot electrodes “4” in Figure 4.7). This result is well supported by the experimental findings by Patterson *et al.*, who observed that impedance increased when measured between the xiphisternal joint and a point 10 cm below the suprasternal notch, opposite to the measurement elsewhere on the thorax [57]. In fact, this thoracic segment in their work overlaps the “upper thorax” in our study. The result shows that it is possible to place a surface electrode on the skin proximal to the heart to reflect the contribution from ventricular contraction.

### ***B. Major-vessel expansion***

That major-vessel expansion causes a decrease in impedance agrees with the results reported by Kim *et al.* [38] and Wang and Patterson [91]. As blood is highly conductive, an increase in its volume is expected to decrease the observed impedance.

Compared to ventricular contraction, major-vessel expansion has a more uniform effect on the curves in Figure 4.5 and Figure 4.6. This appears to agree with the assumed plethysmographic model of ICG in which blood vessels are approximated as cylinders within the thoracic cylinder [26][93]. Such model results in an isopotential surface perpendicular to the long axis of the cylinders, i.e., the same potential, and thus the same impedance, would be measured anywhere on a cross section of the thoracic cylinder. When the vessel diameter increases uniformly at all cross sections due to a blood volume increase, which is mostly the case for the ascending and descending aortas during blood ejection, similar impedance change would result when measured anywhere on a cross section.

We used the impedance change due only to major-vessel expansion to estimate the blood volume increase in the major vessels with Eq. (4.1). Assuming that the band electrodes are placed at levels 4 and 34, i.e., from lower neck to the xiphoid level, we have  $\rho = 154(\Omega \cdot cm)$ ,  $L = 18(cm)$ , and from model calculation  $Z_0 = 34(\Omega)$  and  $\Delta Z = 0.96(\Omega)$ . Eq. (4.1) thus yields  $\Delta vol = 41.4(ml)$ , reasonably close to  $SV = 51 ml$  in Table 4.2. This demonstrates that the ICG's plethysmographic assumptions and Eq. (4.1) would approximately be valid if the major thoracic vessels (predominately ascending and descending aortas and superior and inferior vena cava) was the only factor for impedance change.

This result implies that if spot electrodes are placed in such a way that aortic expansion becomes a major factor in measured impedance change, better estimates of SV can be obtained. In fact, Balestra *et al.* found that placing the electrodes in the esophagus provides a better correlation and a much smaller difference between the SV calculated with Eq. (4.1) and that obtained with the dye-dilution method, because internal esophageal electrodes are much closer to the aorta and the effect of ventricular contraction is negligible [4]. However, esophageal electrodes are not favored in practice because of their invasiveness.

### ***C. Thoracic structural change and the plethysmographic assumptions for ICG***

Plethysmography is solely based on the structural change as a result of blood volume change [26][93][96]. In the case of ICG, this structural change always consists of simultaneous volume change in the ventricles and major vessels. It is obvious that ventricular contraction has a larger effect than major-vessel expansion so that the combined effect on the measurement by band electrodes would still increase the thoracic impedance by  $0.11 \Omega$  (“V+M” vs. “V” and “M” for band electrodes “1” in Figure 4.7). This dominance is understandable because the ventricular blood volume decrease between diastole and systole comes from both ventricles, while a major part of the blood from the right ventricle enters lungs and thus does not contribute to major vessel expansion. So the net effect of the total structural change does not reflect the SV due to major vessel expansion.

Ventricular contraction also causes nonuniformity in the measured impedance in different segments of the thorax. If the plethysmographic principle held, impedance changes along the thoracic trunk would also be uniform, while in fact the impedance change in the upper thorax and those in the neck and lower thorax have opposite signs (“V+M” for spot electrodes “3” vs. “4” and “5” in Figure 4.7). The dominance of ventricular contraction over major-vessel expansion in the combined structural change casts doubts on the validity of the plethysmographic assumptions for ICG, and suggests that achieving a good accuracy in the estimation of SV with Eq. (4.1) using band electrodes is not likely.

### ***D. Lung and blood resistivity change***

That the resistivity decrease for blood and lungs at systole also decreases the thoracic impedance is understandable, because blood has the highest conductivity while lungs have the largest tissue volume in the thorax, so both factors have large impact on the measured impedance. These effects on the impedance measured over skin surface are more uniform than the ventricular-contraction effect (Figure 4.6). This is likely due to

the facts that (1) major thoracic vessels run in parallel with the thoracic trunk, and (2) lungs account for a large thoracic volume.

As the structural change in the thorax slightly increases impedance, it seems that the resistivity change of blood and lungs has a major contribution in reducing the measured impedance (“V+M” vs. “V+M+B+L” for electrodes “1” and “2” in Figure 4.7). This agrees with what Wang and Patterson found: even though volume changes in the ventricles and aortic vessels have large effects, their cancellation causes their net effect to be much smaller than the contributions from the resistivity change of blood and lungs [91]. Visser *et al.* also found via experiments that the contribution from the blood resistivity variations had a comparable magnitude to that from the volume change in thoracic vessels [90].

### ***E. Combination of the four effects***

The combined effect of the four sources is shown in Figure 4.6 and Figure 4.7. The bumps on the curve “V+M+B+L” coincide with those on the curve “V+M” (Figure 4.6), still indicating the dominance of the ventricular-contraction effect near the heart.

Ventricular contraction, the only factor that tends to increase the thoracic impedance at end-systole, has its most dominant effect in the upper thorax, where 82% of the total measured impedance change reflects its contribution. Therefore, it is possible to separate the effect of ventricular contraction from the other three factors by measuring at the upper thorax with spot electrodes. Even though ventricular contraction also contains the SV information, the relation between the impedance change as a result of it and SV is not known quantitatively. In contrast, when placed in the neck area, spot electrodes give more accurate information about the contributions from the other three factors. When band electrodes or spot electrodes are placed between lower neck and xiphoid to measure impedance change as is commonly done, a mixture of all the four factors results that have comparable magnitudes and are thus inseparable. In any case,

the applicability of Eq. (4.1) to the direct estimation of SV is doubtful.

On the other hand, correlation between measured impedance change and SV has been repeatedly documented in experiments and clinical trials. The correlation is conceivable in view that all the four factors are the direct results of ventricular blood ejection from end-diastole to end-systole. Possible ways to apply the correlation rather than to directly apply Eq. (4.1) in the estimation of SV include calibrating an ICG device with an invasive SV measurement or simply measuring the relative change in impedance to reflect the relative change in SV. When this is performed on the same patient, robust results can be obtained, which is in fact used clinically. Since the spot electrode measurement at upper thorax mostly reflects the contribution of ventricular contraction, using spot electrodes to measure upper thoracic impedance change may provide an even more accurate estimation of SV.

Finally, the extremely small impedance change measured in lower thorax (spot electrodes “5” in Figure 4.7) deserve some explanation: (1) the transmission of the pulsatile blood flow in the descending aorta lags significantly behind that in the ascending aorta, and at the instant of end-systole there is not enough blood reaching the lower thorax [45], and (2) the baseline impedance (or the vertical length) of this section is small (see Eq. (4.1)).

In this study, we visually inspected the acquired MR images and chose two distinct instants, end-diastole and end-systole, to build the thorax models and investigate the impedance change in between. Since the peak in aortic blood flow in the descending aorta is significantly behind that in the ascending aorta [45], a more systematic study should include the analysis at several instants during the cardiac cycle so that the time course of thoracic impedance change can be assessed, which may provide us with more insight into the impedance change in ICG.

## V. Conclusions

In contrast to previous studies, this study has focused on how the geometric location of electrodes affects the contributions from different sources to the measured thoracic impedance change, which provides a better picture of the origin of the ICG. Major vessel expansion and change in resistivities of blood and lungs all contribute to a fairly uniform decrease of thoracic impedance measured at the skin surface, while ventricular contraction tends to increase the impedance nonuniformly, affecting the measurements most when electrodes are near the heart. As a result, the spot-electrode measurements vary with electrode location. The nonuniformity can also cause opposite impedance changes in different thoracic segments.

The results of this study have important implications. They suggest that ICG's plethysmographic assumption that approximates the thorax as a tissue cylinder with major vessels embedded in parallel is invalid and Eq. (4.1) is not applicable. Common band-electrode measurements represent a mixed effect of the four sources with different signs and comparable magnitudes. Spot-electrode configurations can separate the ventricular-contraction effect from the rest by placing the electrodes on anterior chest wall near the heart, in which case impedance increases at systole, to allow a better detection of ventricular volume change than with band-electrode configuration. Although in this case Eq. (4.1) is not applicable to directly measure the SV, a relative change in the measured impedance can still reflect a relative change in SV. With proper patient-specific and invasive calibration, measured impedance change might be used to estimate SV.

TABLE 4.1. Tissue resistivities used in the FE models [25][72]

<b>Tissue type</b>	<b>Resistivity (<math>\Omega</math>-cm)</b>
blood (peripheral)	154
blood (aortic, end-diastole)	154
blood (aortic, end-systole)	138
bone	16000
esophagus	700
fat	2180
liver	673
lungs (end-diastole)	1500
lungs (end-systole)	1424
muscle	700
myocardium	420
spleen	420
skin	1500
stomach	800

TABLE 4.2. Blood volume change from end-diastole to end-systole in the ventricles and lungs

<b>Organs</b>	<b>Stroke Volume (ml)</b>
SV in LV & RV	126
Blood volume increase in aorta	51
Blood perfusion in lungs	63

TABLE 4.3.  $\Delta Z$  from Figure 4.5 for the spot- and band-electrode measurements (unit:  $\Omega$ )

Level	Ventricular contraction (V)		Major vessel expansion (M)		Structural change (V+M)	
	spot (heart)	band	spot (heart)	band	spot (heart)	band
4	0.74	0.66	-0.89	-0.69	-0.03	0.11
9	0.86	0.66	-0.81	-0.62	0.27	0.17
14	0.99	0.65	-0.60	-0.51	0.70	0.27
19	1.06	0.61	-0.53	-0.39	0.91	0.34
24	0.72	0.51	-0.31	-0.26	0.69	0.32
29	0.49	0.34	-0.02	-0.15	0.38	0.24
34	-0.39	0.14	0.07	-0.06	-0.42	0.09
39	-0.37	0.00	0.05	0.00	-0.38	0.00

TABLE 4.4.  $\Delta Z$  from Figure 4.6 for the spot- and band-electrode measurements (unit:  $\Omega$ )

Level	Blood resistivity change (B)		Lung resistivity change (L)		Total combined (V+M+B+L)	
	spot (heart)	band	spot (heart)	band	spot (heart)	band
4	-0.82	-0.58	-0.68	-0.62	-0.77	-0.55
9	-0.58	-0.48	-0.61	-0.57	-0.30	-0.40
14	-0.10	-0.34	-0.44	-0.49	0.38	-0.19
19	0.16	-0.23	-0.31	-0.40	0.71	-0.02
24	0.24	-0.14	-0.20	-0.29	0.57	0.07
29	0.19	-0.07	-0.09	-0.18	0.30	0.09
34	0.14	-0.03	-0.02	-0.07	-0.48	0.03
39	0.05	0.00	0.01	0.00	-0.39	0.00

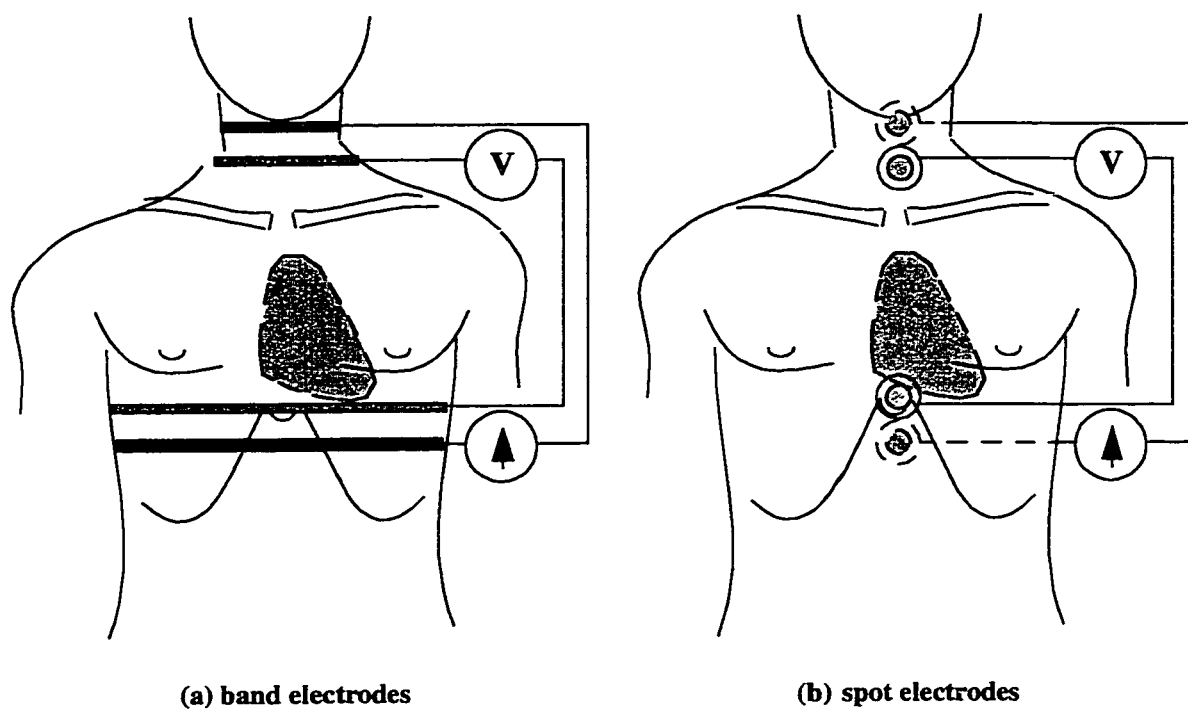


FIGURE 4.1. Schematic diagram of common ICG electrode configuration. The shaded area represents the heart. (a) Band-electrode configuration, in which the outer pair deliver a constant current while the inner pair measure the voltage. (b) Spot-electrode configuration, similar to the band-electrode configuration except that the current-delivering bands are replaced with posterior spot electrodes (dash-line circles) and the voltage-sensing bands are replaced with anterior spot electrodes (solid-line circles).

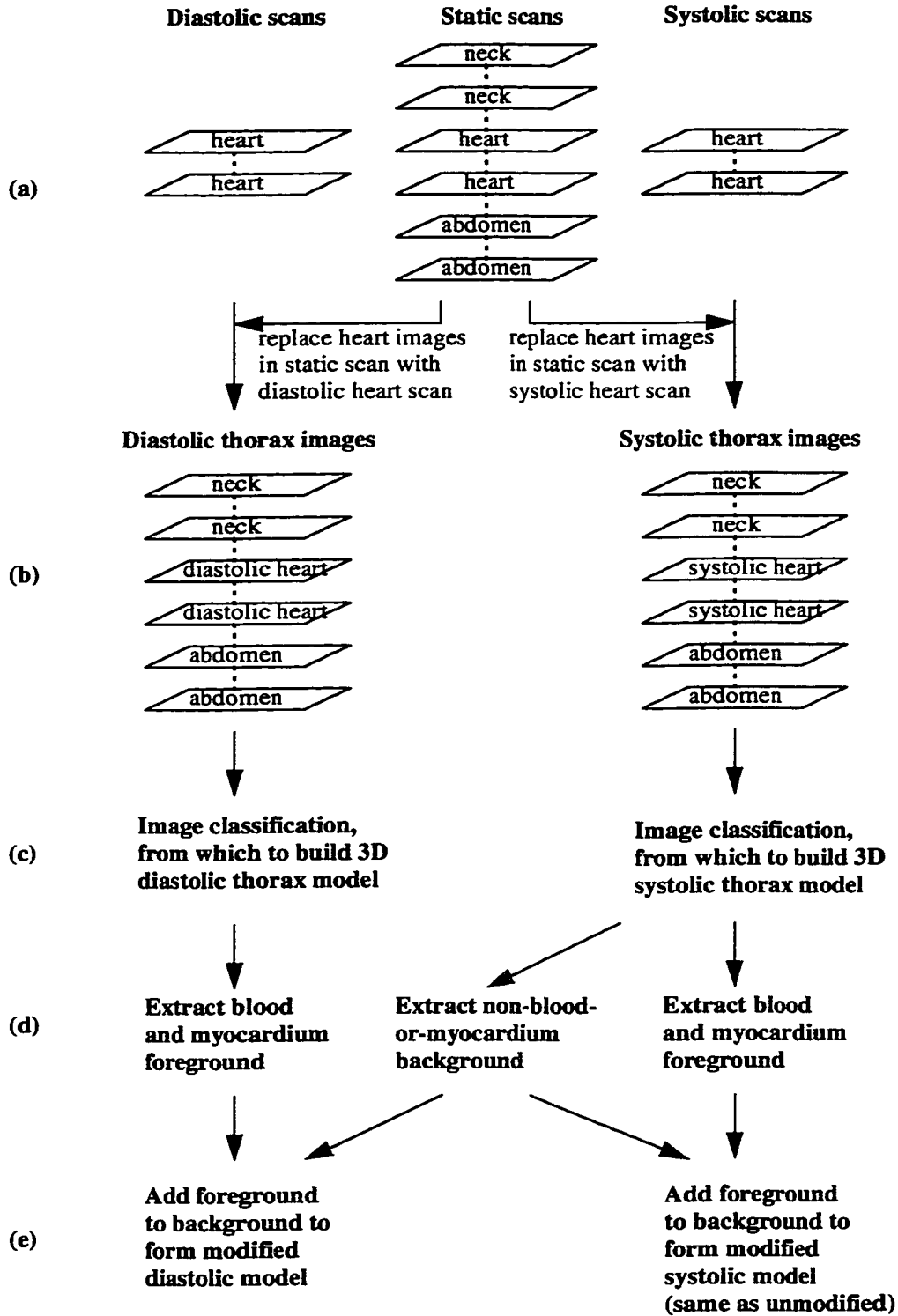
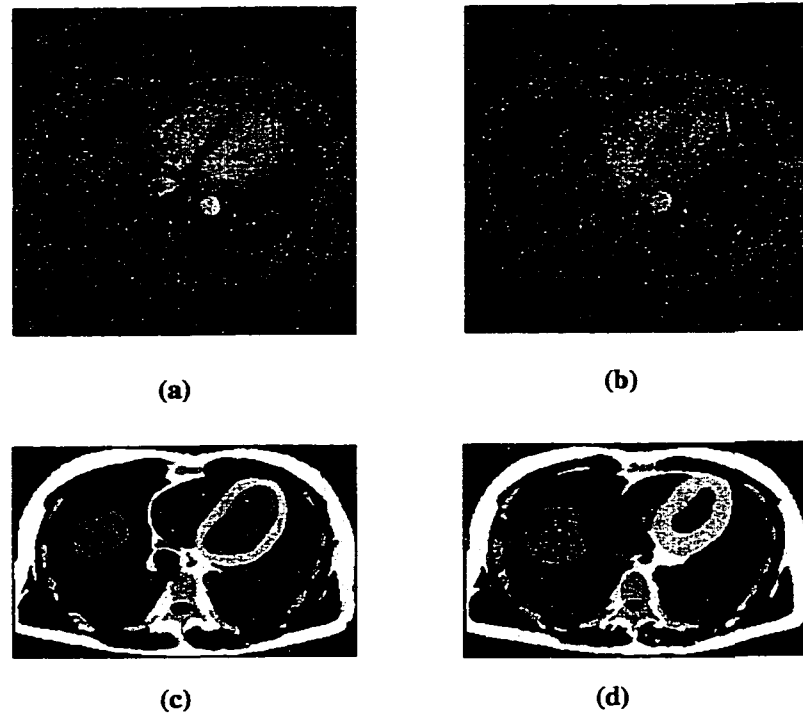


FIGURE 4.2. Procedural steps in creating the diastolic and systolic thorax models.



**FIGURE 4.3.** Example MRI scans and classified images of the subject's heart at end-diastole and end-systole. (a) and (c): MR and classified images at end-diastole; (b) and (d): MR and classified images at end-systole.

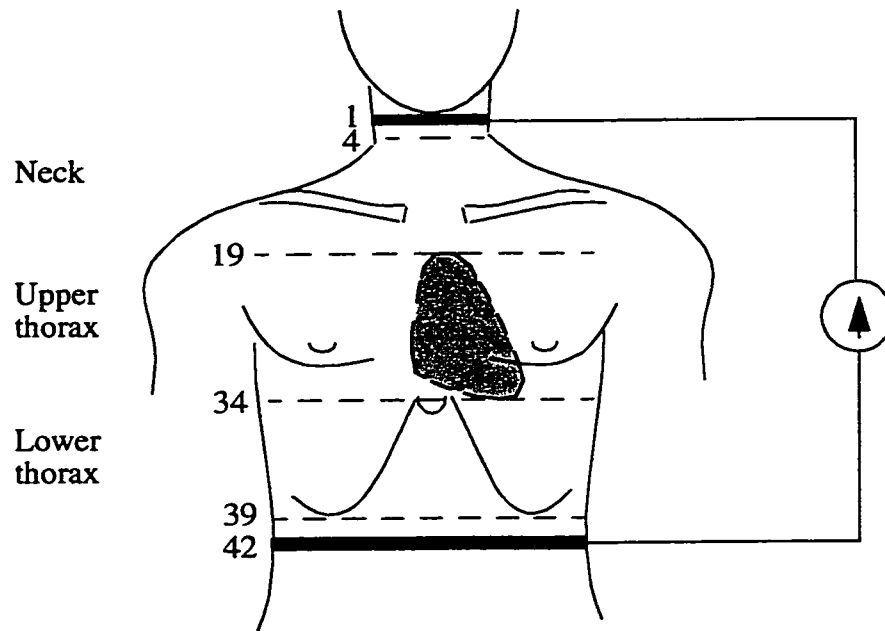


FIGURE 4.4. Schematic diagram of the ICG electrode configurations investigated in this study. The shaded area represents the heart. The outmost dark bands are current-delivering electrodes. The four dash lines in between indicate the division of thorax into neck, upper thorax, and lower thorax from top to bottom. The numbers by the bars and lines correspond to the levels in Figure 4.5 and Figure 4.6: lower neck (4), heart top (19), heart bottom or xiphoid (34), and upper abdomen (39).

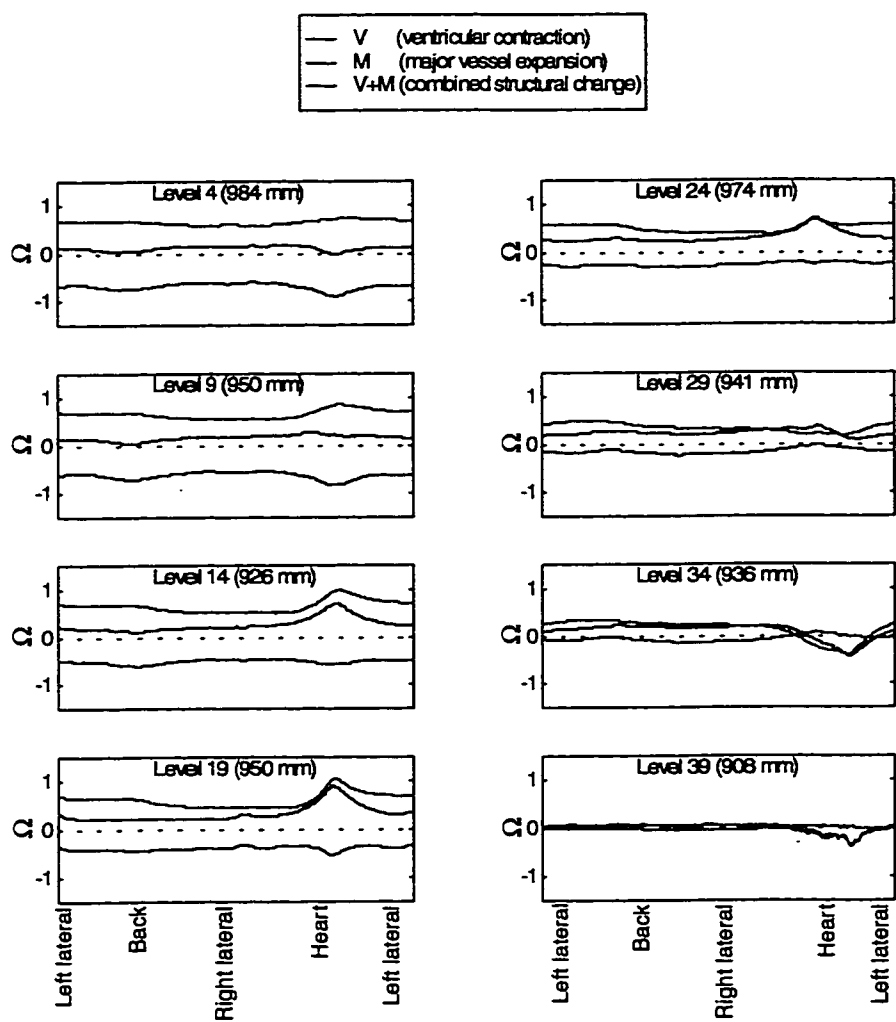


FIGURE 4.5. Simulated measurements of impedance change from end-diastole to end-systole ( $\Delta Z = \Delta Z_{\text{systole}} - \Delta Z_{\text{diastole}}$ ) as a result of ventricular contraction and major-vessel expansion at eight thoracic levels. The impedance is between a position on the skin surface and the bottom current-delivery band electrode.

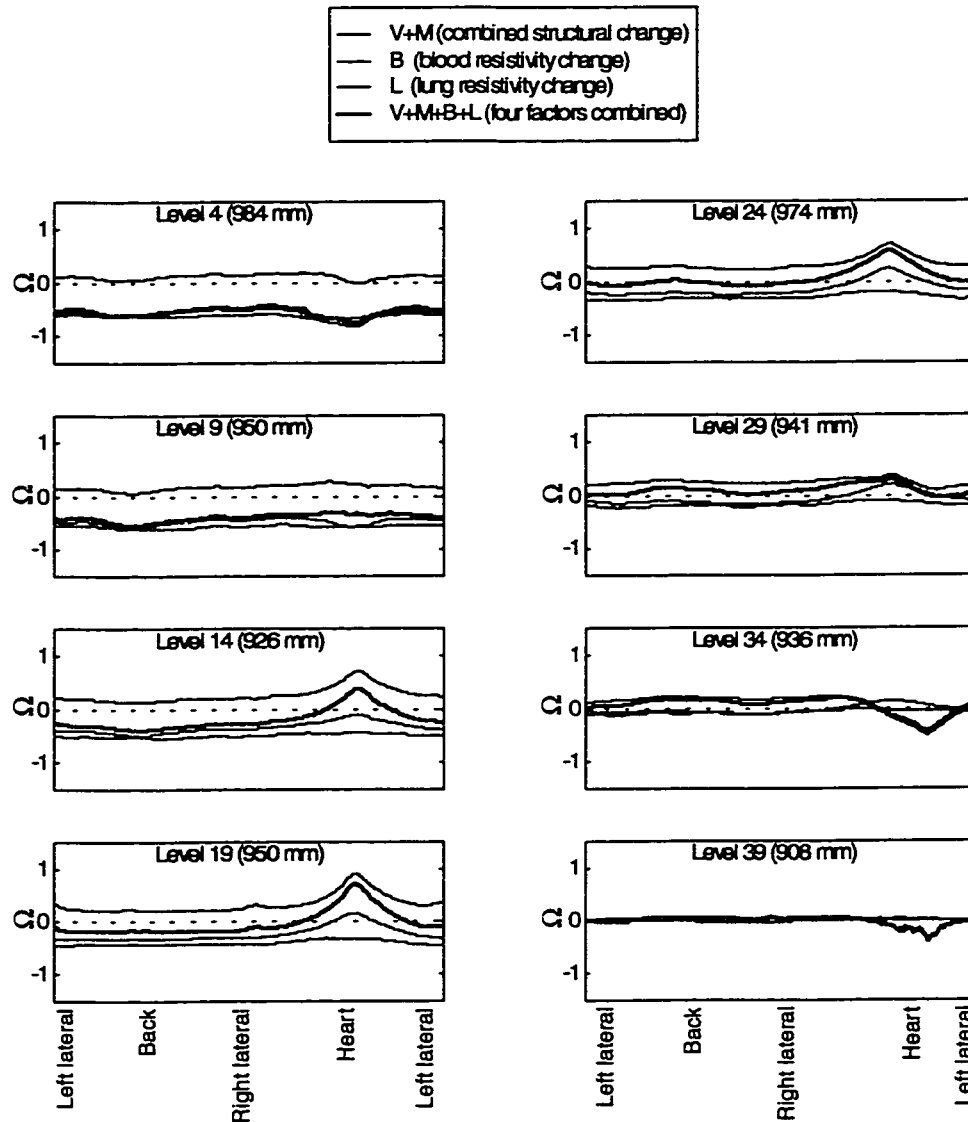


FIGURE 4.6. Simulated measurements of impedance change from end-diastole to end-systole ( $\Delta Z = \Delta Z_{\text{systole}} - \Delta Z_{\text{diastole}}$ ) as a result of the blood and lung resistivity changes, and all the factors combined. Curve “V+M” is from Figure 4.5. The impedance is between a position on the skin surface and the bottom current-delivery band electrode.

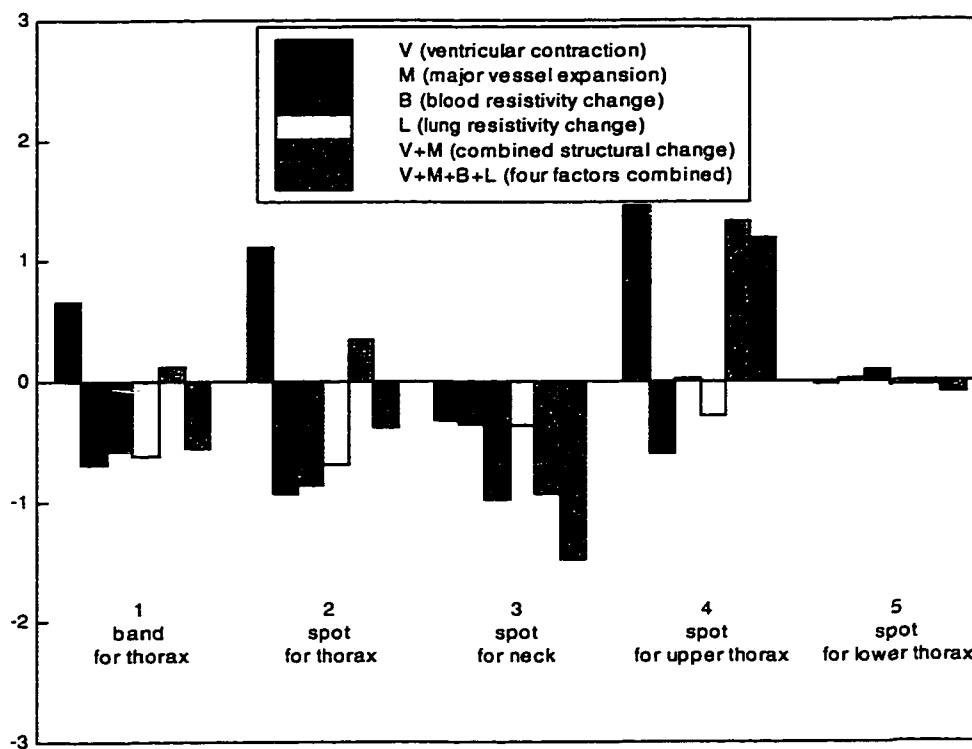


FIGURE 4.7. Simulated measurements of impedance change using five practical band- and spot-electrode configurations covering either one of the whole thorax, neck, upper thorax, and lower thorax. The spot electrodes are also at the anterior heart location horizontally. It shows not only the effect of each individual source, but also the combined effects of structural change in both ventricular and vessel volumes and the combined effects of the four sources occurring simultaneously.

## Bibliography

- [1] A. Adamicza, L. Tutsek, B. Daroczy, F. Bari, and S. Nagy, "The measurement of cardiac output in dogs by impedance cardiography with different electrode arrangements," *Acta Physiologica Hungarica*, vol. 82, pp. 37-52, 1994.
- [2] *AVS User's Guide and AVS Module Reference* (Release 5), Waltham, MA: Advanced Visual Systems, 1993.
- [3] R. Bajcsy and S. Kovacic, "Multiresolution elastic matching," *Computer Vision, Graphics, and Image Processing*, vol. 46, pp. 1-21, 1989.
- [4] B. Balestra, R. Malacrida, L. Leonardi, P. Suter, and C. Marone, "Esophageal electrodes allow precise assessment of cardiac output by bioimpedance," *Critical Care Medicine*, vol. 20, pp. 62-67, 1992.
- [5] A. L. Bardou, J. Degonde, P. J. Birkui, P. Auger, J. M. Chesnais, and M. Duriez, "Reduction of energy required for defibrillation by delivering shocks in orthogonal directions in the dogs," *PACE*, vol. 11, pp. 1990-1995, 1988.
- [6] A. L. Bardou, J. Chesnais, P. J. Birkui, M. Govaere, P. M. Auger, D. von Euw, and J. Degonde, "Directional variability of stimulation threshold measurements in isolated guinea pig cardiomyocytes: relationship with orthogonal sequential defibrillating pulses," *PACE*, vol. 13, pp. 1590-1595, 1990.
- [7] G. H. Bardy, "Sudden cardiac death," *Progress In Cardiology*, Zipes DP and Rowlands DJ (eds), Lea & Febiger, Philadelphia, PA, pp. 157-170, 1988.
- [8] G. H. Bardy, B. Hofer, G. Johnson, P. J. Kudenchuk, J. E. Poole, G. L. Dolack, M. Gleva, R. Mitchell, and D. Kelso, "Implantable transvenous cardioverter-defibrillators," *Circulation*, vol. 87, pp. 1152-1168, 1993.
- [9] R. M. Berne, *Handbook of Physiology: The Cardiovascular System*, vol. 1, Bethesda, Maryland: American Physiological Society, 1979.
- [10] D. P. Bernstein, "A new stroke volume equation for thoracic electrical bioimpedance theory and rationale," *Critical Care Medicine*, vol. 14, pp. 904-909, 1986.
- [11] D. E. Blilie, J. B. Fahy, C. Chan, M. Ahmed and Y. Kim, "Efficient solution of three-dimensional finite element models for defibrillation and pacing applications," *Proceedings of the 13th Annual International Conference of IEEE/EMBS*, Vol. 13, pp. 772-773, 1991.

- [12] F. L. Bookstein, "Principal warps: thin-plate splines and the decomposition of deformations," *IEEE Transactions on Pattern Analysis and Machine Intelligence*, vol. 11, pp. 567-585, 1989.
- [13] F. L. Bookstein, "How to produce a landmark point: the statistical geometry of incompletely registered images," *Proceedings of the SPIE on Vision Geometry*, vol. 2573, pp. 266-277, 1995.
- [14] J. D. Bourland, W. A. Tacker, and L. A. Geddes, "Strength-duration curves for trapezoidal waveforms of various tilts for transchest defibrillation in animals," *Medical Instrumentation*, vol. 12, pp. 38-41, 1978.
- [15] B. H. Brown, D. C. Barber, A. H. Morice, and A. D. Leathard, "Cardiac and respiratory related electrical impedance changes in the human thorax," *IEEE Transactions on Biomedical Engineering*, vol. 41, pp. 729-733, 1994.
- [16] H. C. Burger and J. B. Milaan, "Measurements of the specific resistance of the human body to direct current," *Acta Medica Scandinavica*, vol. 114, pp. 585-607, 1943.
- [17] H. C. Burger and R. van Dongen "Specific electrical resistance of body tissues," *Physics in Medicine & Biology*, vol. 5, pp. 431-447, 1961.
- [18] R. E. Carlson and T. A. Foley, "The parameter  $R^2$  in multiquadric interpolation," *Computers and Mathematics with Applications*, vol. 21, pp. 29-42, 1991.
- [19] L. Clerc, "Directional differences of impulse spread in trabecular muscle from mammalian heart," *Journal of Physiology (London)*, vol. 255, pp. 335-346, 1976.
- [20] J. M. Davy, "Is there a defibrillation threshold?" (abstract), *Circulation*, vol. 70, Supplement II, pp. 406, 1984.
- [21] B. R. Epstein and K. R. Foster, "Anisotropy in the dielectric properties of skeletal muscle," *Medical & Biological Engineering & Computing*, vol. 21, pp. 51-55, 1983.
- [22] T. A. Foley, "Deformation of volumes using scattered landmark points," *Intelligent Systems*, E. A. Yfantis (ed.), pp. 841-851, 1995.
- [23] R. Franke, "Scattered data interpolation: tests of some methods," *Mathematics of Computation*, vol. 38, pp. 181-200, 1982.
- [24] H. Fricke, "The electric conductivity and capacity of disperse systems," *Physics*, vol. 1, pp. 106-115, 1931.

- [25] L. A. Geddes and L. E. Baker, "The specific resistance of biological material: a compendium of data for the biomedical engineer and physiologist," *Medical & Biological Engineering*, vol.5, pp. 271-293, 1967.
- [26] L. A. Geddes and L. E. Baker, *Principles of Applied Biomedical Instrumentation*, 3rd ed., New York: Wiley, 1989.
- [27] F. L. H. Gielen, W. Wallinga-de Jonge, and K. L. Boon, "Electrical conductivity of skeletal muscle tissue: experimental results from different muscles *in vivo*," *Medical & Biological Engineering & Computing*, vol. 22, pp. 569-577, 1984.
- [28] *Guide for the Care and Use of Laboratory Animals*, National Institute of Health publication #86-23, revised 1985.
- [29] P. A. Guse, K. M. Kavanagh, C. A. Alferness, P. D. Wolf, D. Rollins, J. Hagler, W. M. Smith, and R. E. Ideker, "Defibrillation with low voltage using a left ventricular catheter and four cutaneous patch electrodes in dogs," *PACE*, vol. 14, pp. 443-451, 1991.
- [30] W. Hort, "Makroskopische und mikrometrische Untersuchungen am Myokard verschieden stark gefullter linker Kammern," *Virchows Arch. Pathol. Anat. Physiol. Klin. Med.*, vol. 333, pp. 523-564, 1960.
- [31] D. W. Hosmer and S. Lemeshow, *Applied Logistic Regression*. New York, NY: John Wiley, 1989.
- [32] R. E. Ideker, P. D. Wolf, C. Alferness, W. Krassowska, and W. M. Smith, "Current concepts for selecting the location, size and shape of defibrillation electrodes," *PACE*, vol. 14, pp. 227-240, 1991.
- [33] L. Jensen, J. Yakimets, and K. K. Teo, "Issues in cardiovascular care: a review of impedance cardiography," *Heart & Lung*, vol. 24, pp. 183-193, 1995.
- [34] D. L. Jones, G. J. Killein, G. M. Guiraudon, and A. D. Sharma, "Sequential pulse defibrillation in humans: orthogonal sequential pulse defibrillation with epicardial electrodes," *Journal of American College of Cardiology*, vol. 11, pp. 590-596, 1988.
- [35] D. B. Jorgenson, D. R. Haynor, G. H. Bardy, and Y. Kim, "Computational studies of transthoracic and transvenous defibrillation in a detailed 3-D human thorax model," *IEEE Transactions on Biomedical Engineering*, vol. 42, pp. 172-184, 1995.
- [36] D. B. Jorgenson, P. H. Schimpf, I. Shen, G. Johnson, G. H. Bardy, D. R. Haynor, and Y. Kim, "Predicting cardiothoracic voltages during high energy shocks: meth-

- odology and comparison of experimental to finite element model data," *IEEE Transactions on Biomedical Engineering*, vol. 42, pp. 559-571, 1995.
- [37] W. J. Karlon, S. R. Eisenberg, and J. L. Lehr, "Effects of paddle placement and size on defibrillation current distribution: A three-dimensional finite element model," *IEEE Transactions on Biomedical Engineering*, vol. 40, pp. 246-255, 1993.
- [38] D. W. Kim, L. E. Baker, J. A. Pearce, and W. K. Kim, "Origins of the impedance change in impedance cardiography by a three-dimensional finite element model," *IEEE Transactions on Biomedical Engineering*, vol. 35, pp. 993-1000, 1988.
- [39] D. W. Kim, "Detection of physiological events by impedance," *Yonsei Medical Journal*, vol. 30, pp. 1-11, 1989.
- [40] Y. Kim, *A three-dimensional modifiable computer body model and its applications*, Ph.D. dissertation, University of Wisconsin, Madison, WI, 1982.
- [41] Y. Kim, J. B. Fahy, and B. J. Tupper, "Optimal electrode designs for electrosurgery, defibrillation, and external cardiac pacing," *IEEE Transactions on Biomedical Engineering*, vol. 33, pp. 845-853, 1986.
- [42] Y. Kim, H. G. Zieber, and F. E. Wang, "Uniformity of current density under stimulating electrodes," *Critical Reviews in Biomedical Engineering*, vol. 17, pp. 585-619, 1990.
- [43] W. G. Kubicek, J. M. Karnegis, R. P. Patterson, D. A. Witsoe, and R. H. Mattson, "Development and evaluation of an impedance cardiac output system," *Aerospace Medicine*, vol. 37, pp. 1208-1212, 1966.
- [44] W. G. Kubicek, R. P. Patterson, and D. A. Witsoe, "Impedance cardiography as a noninvasive method of monitoring cardiac function and other parameters of the cardiovascular system," *Annals New York Academy of Sciences*, vol. 170, pp. 724-732, 1970.
- [45] W. G. Kubicek, F. J. Kottke, M. U. Ramos, R. P. Patterson, D. A. Witsoe, J. W. Labree, W. Remole, T. E. Layman, H. Schoening, and J. T. Garamela, "The Minnesota impedance cardiograph - theory and applications," *Biomedical Engineering*, vol. 9, pp. 410-416, 1974.
- [46] I. J. LeGrice, P. J. Hunter, and B. H. Smaill, "Laminar structure of the heart: a mathematical model," *American Journal of Physiology*, vol. 272, pp. H2466-2476, 1997.
- [47] W. C. McDaniel and J. C. Schuder, "An up-down algorithm for estimation of the cardiac ventricular defibrillation threshold," *Medical Instrumentation*, vol. 22, pp. 286-292, 1988.

- [48] C. E. Miller and C. S. Henriquez, "Finite element analysis of bioelectric phenomena," *Critical Reviews in Biomedical Engineering*, vol. 18, pp. 207-233, 1990.
- [49] S. N. Mohapatra, *Non-invasive cardiovascular monitoring by electrical impedance technique*, London: Pitman Medical, 1981.
- [50] M. Moshfeghi, S. Ranganath, and K. Nawyn, "Three-dimensional elastic matching of volumes," *IEEE Transactions on Image Processing*, vol. 3, pp. 128-138, 1994.
- [51] M. M. Mower, "Patterns of ventricular activity during catheter defibrillation," *Circulation*, vol. 49, pp. 858-861, 1974.
- [52] G. M. Nielson, T. A. Foley, B. Hamann, and D. Lane, "Visualizing and modeling scattered multivariate data," *IEEE Computer Graphics and Applications*, vol. 11, pp. 47-55, 1991.
- [53] G. M. Nielsen, "Scattered data modeling," *IEEE Computer Graphics and Applications*, vol. 13, pp. 60-70, 1993.
- [54] P. M. F. Nielsen, I. J. Le Grice, B. H. Smaill, and P. J. Hunter, "Mathematical model of geometry and fibrous structure of the heart," *American Journal of Physiology*, vol. 260, pp. H1365-1378, 1991.
- [55] J. Nyboer, *Electrical impedance plethysmography*, Springfield, Illinois: Thomas, 1970.
- [56] M. Oeff, J. A. Abbott, E. D. Scheinman, E. S. Yee, M. M. Scheinman, and J. C. Griffin, "Determination of patch electrode position for the internal cardioverter-defibrillator by cine computed tomography and its relation to the defibrillation threshold," *Journal of American College of Cardiology*, vol. 20, pp. 210-217, 1992.
- [57] R. P. Patterson, L. Wang, and S. B. Raza, "Impedance cardiography using band and regional electrodes in supine, sitting, and during exercise," *IEEE Transactions on Biomedical Engineering*, vol. 38, pp. 393-400, 1991.
- [58] B. C. Penney, N. A. Patwardhan, and H. B. Wheeler, "Simplified electrode array for impedance cardiography," *Medical and Biological Engineering and Computing*, vol. 23, pp.1-7, 1985.
- [59] R. Plonsey and R. Barr, "The four-electrode resistivity technique as applied to cardiac muscle," *IEEE Transactions on Biomedical Engineering*, vol. 29, pp. 541-546, 1982.
- [60] R. Plonsey and R. C. Barr, "A critique of impedance measurements in cardiac tissue," *Annals of Biomedical Engineering*, vol. 14, pp. 307-322, 1986.

- [61] M. Qu, Y. Zhang, J. G. Webster, and W. J. Tompkins, "Motion artifact from spot and band electrodes during impedance cardiography," *IEEE Transactions on Bio-medical Engineering*, vol. 33, pp. 1029-1036, 1986.
- [62] M. H. Raitt, G. Johnson, G. L. Dolack, J. E. Poole, P. J. Kudenchuk, and G. H. Bardy, "Clinical predictors of the defibrillation threshold with the unipolar implantable defibrillation system," *Journal of American College of Cardiology*, vol. 25, pp. 1576-1583, 1995.
- [63] M. F. Rattes, D. L. Jones, A. D. Sharma, and G. J. Klein, "Defibrillation threshold: a simple and quantitative estimate of the ability to defibrillate," *PACE*, vol. 10, pp. 70-77, 1987.
- [64] T. G. Reese, R. M. Weisskoff, R. N. Smith, B. R. Rosen, R. E. Dinsmore, and van J. Wedeen, "Imaging myocardial fiber architecture *in vivo* with magnetic resonance," *Magnetic Resonance in Medicine*, vol. 34, pp. 786-791, 1995.
- [65] D. E. Roberts, L. T. Hersh, and A. M. Scher, "Influence of fiber orientation on wavefront voltage, conduction velocity, and tissue resistivity in the dog," *Circulation Research*, vol. 44, pp. 701-712, 1979.
- [66] M. A. Ross and D. D. Streeter Jr., "Nonuniform subendocardial fiber orientation in the normal macaque left ventricle," *European Journal of Cardiology*, vol. 3, pp. 229-247, 1975.
- [67] B. J. Roth, "Mechanisms for electrical stimulation of excitable tissue," *Critical Reviews in Biomedical Engineering*, vol. 22, pp. 253-305, 1994
- [68] S. Rush, "Methods of measuring the resistivities of anisotropic conducting media *in situ*," *Journal of Research of the National Bureau of Standards - C. Engineering and Instrumentation*, vol. 66C, pp. 217-222, 1962.
- [69] S. Rush, J. A. Abildskov, and R. McFee, "Resistivity of body tissues at low frequencies," *Circulation Research*, vol. 12, pp. 40-50, 1963.
- [70] P. H. Schimpf, D. R. Haynor, and Y. Kim, "Object-free adaptive meshing in highly heterogeneous 3-D domains," *International Journal of Biomedical Computing*, vol. 40, pp. 209-225, 1996.
- [71] P. H. Schimpf, Y. Wang, D. R. Haynor, and Y. Kim, "Sensitivity of transvenous defibrillation models to adaptive mesh density and resolution: the potential for interactive solution times," *International Journal of Bio-Medical Informatics*, vol. 45, pp. 193-207, 1997.
- [72] H. P. Schwan and C. F. Kay, "Specific resistance of body tissues," *Circulation Research*, vol. 9, pp. 664-670, 1956.

- [73] H. P. Schwan, "Electrode polarization impedance and measurements in biological materials," *Annals New York Academy of Sciences*, vol. 148, pp. 191-209, 1968.
- [74] N. G. Sepulveda, B. J. Roth, and J. P. Wikswo, Jr., "Current injection into a two-dimensional anisotropic bidomain," *Biophysical Journal*, vol. 55, pp. 987-999, 1989.
- [75] N. G. Sepulveda, J. P. Wikswo, and D. S. Echt, "Finite element analysis of cardiac defibrillation current distributions," *IEEE Transactions on Biomedical Engineering*, vol. 37, pp. 354-365, 1990.
- [76] N. Shrinidi, D. R. Haynor, Y. Wang, D. B. Jorgenson, and Y. Kim, "An efficient tissue classification system for X-ray CT images to build patient-specific finite element models," *IEEE Transactions on Biomedical Engineering*, vol. 43, pp. 333-337, 1996.
- [77] I. Singer and D. Lang, "Defibrillation threshold: Clinical utility and therapeutic implications," *PACE*, vol. 15, pp. 932-949, 1992.
- [78] I. Singer, J. Goldsmith, and C. Maldonado, "Transseptal defibrillation is superior for transvenous defibrillation," *PACE*, vol. 18, pp. 229-232, 1995.
- [79] H. M. Spotnitz, *Research Frontiers in Implantable Defibrillator Surgery*. Boca Raton, FL: CRC Press, 1992.
- [80] B. B. Sramek, D. M. Rose, and A. Miyamoto, "Stroke volume equation with a linear base impedance model and its accuracy, as compared to thermodilution and magnetic flowmeter techniques in humans and animals," *Proceedings of Sixth International Conference on Electrical Bioimpedance*, Zadar, Yugoslavia, pp. 38-41, 1983.
- [81] P. Steendijk, G. Mur, E. T. van de Velde, and J. Baan, "The four-electrode resistivity technique in anisotropic media: theoretical analysis and application on myocardial tissue *in vivo*," *IEEE Transactions on Biomedical Engineering*, vol. 40, pp. 1138-1148, 1993.
- [82] D. D. Streeter Jr. and D. L. Bassett, "Engineering analysis of myocardial fiber orientation in pig's left ventricle in systole," *Anatomical Record*, vol. 155, pp. 503-511, 1966.
- [83] D. D. Streeter Jr., H. M. Spotnitz, D. J. Patel, J. Ross Jr., and E. H. Sonnenblick, "Fiber orientation in the canine left ventricle during diastole and systole," *Circulation Research*, vol. 24, pp. 339-347, 1969.
- [84] D. D. Streeter, Jr., W. E. Powers, M. A. Ross, and F. Torrent-Guasp, "Three-dimensional fiber orientation in the mammalian left ventricular wall," *Cardiovascular*

*System Dynamics*, J. Baan, A. Noordergraaf, and J. Raines (Ed.), Cambridge, MA: MIT Press, 1978.

- [85] D. D. Streeter Jr., "Gross morphology and fiber geometry of the heart," *Handbook of Physiology: A critical, comprehensive presentation of physiological knowledge and concepts*, vol. I, R. M. Berne (ed.), Bethesda, MD: American Physiological Society, pp. 61-112, 1979.
- [86] M. F. Suesserman and F. A. Spelman, "Quantitative *in vivo* measurements of inner ear tissue resistivities: I. *In vitro* characterization," *IEEE Transactions on Biomedical Engineering*, vol. 40, pp. 1032-1047, 1993.
- [87] W. A. Tacker, *Defibrillation of the Heart*. St. Louis, MO: Mosby, 1994.
- [88] L. Tung, N. Sliz, and M. R. Mulligan, "Influence of electrical axis of stimulation on excitation of cardiac muscle cells," *Circulation Research*, vol. 69, pp. 722-730, 1991.
- [89] K. R. Visser, "Electric properties of flowing blood and impedance cardiography," *Annals of Biomedical Engineering*, vol. 17, pp. 463-473, 1989.
- [90] K. R. Visser, R. Lamberts, and W. G. Zijlstra, "Investigation of the origin of the impedance cardiogram by means of exchange transfusion with stroma free haemoglobin solution in the dog," *Cardiovascular Research*, vol. 24, pp. 24-32, 1990.
- [91] L. Wang and R. Patterson, "Multiple sources of the impedance cardiogram based on 3-D finite difference human thorax models," *IEEE Transactions on Biomedical Engineering*, vol. 42, pp. 141-148, 1995.
- [92] Y. Wang, P. H. Schimpf, D. R. Haynor, G. H. Bardy, and Y. Kim, "Analysis of defibrillation efficacy from myocardial voltage gradients with finite element modeling," *IEEE Transactions on Biomedical Engineering*, in print, February 1998.
- [93] J. G. Webster, *Medical Instrumentation: Application and Design*, 3rd ed., New York: Wiley, 1998.
- [94] F. X. Witkowski, P. A. Penkoske, and R. Plonsey, "Mechanism of cardiac defibrillation in open-chest dogs with unipolar DC-coupled simultaneous activation and shock potential recordings," *Circulation*, vol. 82, pp. 244-260, 1990.
- [95] H. H. Woltjer, B. J. M. van der Meer, H. J. Bogaard, and P. M. J. M. de Vries, "Comparison between spot and band electrodes and between two equations for calculations of stroke volume by means of impedance cardiography," *Medical & Biological Engineering & Computing*, vol. 33, pp. 330-334, 1995.

- [96] J. P. Woodcock, "Plethysmography," *Biomedical Engineering*, vol. 9, pp. 406-409, 1974.
- [97] J. H. Zar, *Biostatistical Analysis*. 3rd ed., Upper Saddle River, NJ: Prentice-Hall, 1996.
- [98] Y. Zhang, M. Qu, J. G. Webster, W. J. Tompkins, B. A. Ward, and D. R. Bassett, Jr., "Cardiac output monitoring by impedance cardiography during treadmill exercise," *IEEE Transactions on Biomedical Engineering*, vol. 33, pp. 1037-1042, 1986.
- [99] E. Zheng, S. Shao, and J. G. Webster, "Impedance of skeletal muscle from 1 Hz to 1 MHz," *IEEE Transactions on Biomedical Engineering*, vol. 31, pp. 477-481, 1984.
- [100] X. Zhou, J. P. Daubert, P. D. Wolf, W. M. Smith, and R. E. Ideker, "Size of the critical mass for defibrillation," (abstract), *Circulation*, vol. 80, pp. II-531, 1989.
- [101] X. Zhou, P. D. Wolf, D. L. Rollins, W. M. Smith, and R. E. Ideker, "Potential gradient needed for defibrillation with monophasic and biphasic shocks," (abstract), *PACE*, vol. 12, pp. 651, 1989.
- [102] O. C. Zienkiewicz, *The Finite Element Method in Engineering Science*. 2nd ed., London, McGraw-Hill, 1977.
- [103] D. P. Zipes, J. Fischer, R. M. King, A. deB. Nicoll, and W. W. Jolly, "Termination of ventricular fibrillation in dogs by depolarizing a critical amount of myocardium," *American Journal of Cardiology*, vol. 36, pp. 37-44, 1975.

## Curriculum Vitae

*Yanguan Wang*

### EDUCATION

Ph.D. in Bioengineering, 6/1999.

University of Washington, Department of Bioengineering, Seattle, WA.

Ph.D. dissertation: Analysis of defibrillation efficacy and investigation of impedance cardiography with finite element models incorporating anisotropic myocardium.

M.S. in Electronics Engineering, 10/1990.

Chinese Academy of Sciences, Institute of Electronics, Beijing, China.

M.S. thesis: Efficient and realistic rendering of 3-D space-filling molecular models.

B.S. in Biomedical Engineering, 7/1987.

Shanghai Jiao Tong University, Department of Biomedical Engineering, Shanghai, China.

B.S. thesis: Development of an MC68000 based radiographic imaging system.

### PROFESSIONAL SKILLS AND RESEARCH INTEREST

Finite element modeling, image processing, visualization, medical instrumentation, cardiac electrophysiology and defibrillation devices, animal experiments, medical informatics.

Programming with C/C++, LabVIEW, and Matlab, Java, and client/server in Windows and Unix.

### WORK EXPERIENCE

#### Teaching

BIOEN535: *Medical Instrumentation (Digital)*, Department of Bioengineering, University of Washington, winter 1998.

EE/BIOEN436: *Introduction to Medical Instrumentation*, Departments of Bioengineering and Electrical Engineering, University of Washington, spring 1998.

#### Industry

Software engineer: Beijing New AUTO Corporation, Beijing, China, 7/1989-10/1990.

Software engineer: Shanghai Power Construction Bureau, Shanghai, China, 10/1990-9/1992.

Software developer: medical informatics applications, Integrated Advanced Information Management System (IAIMS), Health Sciences Center, University of Washington, 11/1998-5/1999.

## PUBLICATIONS

Y. Wang, P. H. Schimpf, D. R. Haynor, G. H. Bardy, and Y. Kim, "Analysis of defibrillation efficacy from myocardial voltage gradients with finite element modeling," *IEEE Transactions on Biomedical Engineering*, in press, to appear in September 1999.

Y. Wang, P. H. Schimpf, D. R. Haynor, and Y. Kim, "Geometric effects on resistivity measurements with four-electrode probes in isotropic and anisotropic tissues," *IEEE Transactions on Biomedical Engineering*, vol. 45, pp. 877-884, 1998.

P. H. Schimpf, Y. Wang, D. R. Haynor, and Y. Kim, "Sensitivity of transvenous defibrillation models to adaptive mesh density and resolution: the potential for interactive solution times," *International Journal of Bio-Medical Informatics*, vol. 45, pp. 193-207, 1997.

N. Shrinidhi, D. R. Haynor, Y. Wang, D. B. Jorgenson, G. H. Bardy, and Y. Kim, "An efficient tissue classifier for building patient-specific finite element models from X-ray images," *IEEE Transactions on Biomedical Engineering*, vol. 43, pp. 333-337, 1996.

S. J. Jantz, P. H. Schimpf, Y. Wang, D. R. Haynor, and Y. Kim, "Visualization of finite element models of defibrillation," *Proceedings of 17th IEEE-EMBS Annual Conference*, pp. 359-360, 1995.

Y. Wang, "More realistic and efficient algorithm for the rendering of 3-D space-filling molecular models," *SPIE Visual Communication and Image Processing*, vol. 1606, pp. 1027-1036, 1991.